Real-Time Optimization and Control of Refinery Cracking Processes: Theory and Industrial Applications

by

Hasan Şıldır

A Thesis Submitted to the
Graduate School of Sciences and Engineering
in Partial Fulfillment of the Requirements for
the Degree of Doctor of Philosophy

Doctor of Philosophy
in
Chemical and Biological Engineering

Koc University

June 2014
Koc University
Graduate School of Sciences and Engineering

This is to certify that I have examined this copy of a Doctor of Philosophy by

Hasan Şıldır

and have found that it is complete and satisfactory in all respects,
and that any and all revisions required by the final
examining committee have been made.

Committee Members:

Yaman Arkun, Ph. D. (Advisor)

Can Erkey, Ph. D.

Murat Sözer, Ph. D.

Devrim Kaymak, Ph. D.

Alper Uzun, Ph. D.

Date: ______________________________

ABSTRACT

Cracking is an important catalytic process which is used to convert high boiling, high molecular weight hydrocarbon fractions to smaller molecules. Industrial cracking units process large throughputs and small improvements in the process operations result in significant profits. At the same time safety and product quality is an important concern. For these reasons real-time optimization and control of industrial cracking plants is an important research area.

Chemistry of industrial cracking plants is very complex since cracking involves a high number of chemical species. There are 3 major approaches to modeling of such complex reaction medium: Sequential Oriented Lumping, Continuous Lumping and Discrete Lumping. The first approach is not very flexible for industrial applications. The other two approaches have been used to model cracking reactions in this study.

The method of continuous lumping treats the complex reactive mixture as a continuum. In this thesis it is used to model an industrial hydrocracker plant whose primary products are mainly middle distillates. The hydrocracker plant involves the reactor and the fractionation unit which separates the effluent into final products. The material and energy balances in the reactor are developed in the form of integro-differential equations. Instead of developing a rigorous fractionation model, we have derived an empirical dynamic model from historical plant data. Once the model is available, a plant-wide control structure is designed to provide transition between changing operating conditions due to disturbance or shifts in prices. The proposed hierarchical control structure includes an upper control layer which includes the profit related outputs in the objective function directly and coordinates low level decentralized control blocks for plant wide profitability.

The method of discrete lumping divides the complex reactive mixture into pure and discrete pseudo-components. In this thesis it is used to model an industrial Fluid Catalytic

Cracker (FCC) plant whose primary products are primarily light distillates. Similar to the hydrocracker, FCC plant involves reaction and fractionation units. For the reaction unit, the reaction medium is divided into a high number of pseudo-components and semi-empirical correlations are developed to estimate the properties of each fraction. The plant operating window is calculated to observe the influence of plant inputs on profit and crucial outputs. An economic model predictive controller (EMPC) is designed to account for the plant profit under both steady state and the dynamic operating conditions. The plant is stabilized by terminal region constraints on EMPC and a lower level traditional model predictive control block.

This work proposes practical solutions to complex refinery problems by developing novel modeling and control approaches. The potential benefit from the implementation of current methods is demonstrated with several case studies.

ÖZET

Kırılma, yüksek kaynama noktası ve moleküler ağırlığa sahip hidrokarbonların parçalanarak daha küçük moleküllere dünüştüğü önemli bir katalitik prosestir. Endüstriyel kırılma üniteleri büyük hammaddeleri işler ve proseslerdeki küçük iyileştirmeler ciddi karlılıkla sonuçlanır. Diğer taraftan, ünite güvenliği ve ürün kalitesi önemli bir kısıttır. Bu sebeplerden dolayı, endüstriyel kırılma ünitelerinin gerçek zamanlı optimizasyonu kritik bir araştırma konusudur.

Çok sayıda kimyasal tür içermesi sebebiyle endüstriyel kırılma üniteleri çok karışıktır. Bu karışık reaksiyon ortamının modellenmesinde 3 ana yöntem vardır: Ardışık odaklı kümeleme, sürekli kümeleme ve kesikli kümeleme. İlk yaklaşım endüstriyel uygulamaları için çok esnek değildir. Bu çalışmada kırılma reaksiyonlarının modellenmesi için diğer 2 yöntem kullanılmıştır.

Sürekli kümeleme yöntemi karmaşık reaktif karışımları sürekli olarak varsayar. Bu tezde, bu yöntem temel ürünleri orta distilatlar olan endüstriyel hidrokraker ünitesinin modellenmesi için kullanılmıştır. Hidrokraker ünitesi, reaksiyon ünitesini ve akımın son ürünlere ayrıldığı ayrıştırma ünitesini içermektedir. Reaktörde geliştirilen kütle ve enerji denklemleri integro-türevsel yapıdadır. Ayrıştırma kısmında, mekanistik bir ayrıştırma modeli geliştirmek yerine geçmiş ünite datalarından elde edilen dinamik empirik model kullanılmıştır. Modeli kullanarak, kontrol yapısı bozucu etkiler ya da değişen fiyatlar sebebiyle yer değiştiren operasyon koşulları arasında geçişi sağlamıştır. Bu kontrol yapısındaki üst katman karlılık odaklı çıktıları hedef fonksiyonunda içerir ve alt seviye bağımsız kontrol yapılarını koordine eder.

Kesikli kümeleme yöntemi, reaksiyon karışımını saf ve kesikli bileşenlere ayırır. Bu tezde, bu yöntem temel ürünleri hafif distilatlar olan endüstriyel akışkan yataklı kırıcının (FCC) modellenmesinde kullanılmıştır. Hidrokrakerdeki gibi, FCC ünitesi reaksiyon ve ayırma kısımlarını içermektedir. Reaksiyon ünitesinde, reaksiyon karışımını çok sayıda bileşene bölünmüştür ve her bir bileşenin özellikleri geliştirilen yarı-empirik modeller ile belirlenmiştir. Ünite girdilerinin karlılık ve önemli çıktıları üzerindeki etkilerini incelemek için ünite çalışma penceresi hesaplanmıştır. Hem yatışkın hal hem de dinamik rejimdeki ünite karlılığını hesaplara katmak için ekonomik model öngörülü kontrol (EMPC) tasarlanmıştır. Ünite, son zamanlar için konulan kısıtlar ve alt seviyedeki standart model öngörülü kontrol ile stabil hale getirilmiştir.

Buradaki tartışmalar, yeni modelleme ve kontrol yaklaşımları geliştirerek karışık rafineri problemlerine pratik çözümler sunmaktadır. Bunların uygulanması durumundaki olası getirileri birçok vaka çalışması ile gösterilmiştir.

ACKNOWLEDGEMENTS

I would like to show my gratitude for Prof. Dr. Yaman Arkun. He has been a great inspiration during the most challenging part of my life. I am grateful for his support and guidance. The discussions and the memories are never to be forgotten.

I would also like to thank to:

My thesis committee for their valuable comments during my studies;

TUPRAS refineries for the financial support;

friends in TUPRAS for their valuable contributions and the effort they have spent;

friends from my office and university;

my instructors at my current and previous faculties;

my father, mother and sister.

Lastly, I feel blessed for having my wife, Ayşegül. I can not imagine me accomplishing this much without her. All has been and will be thanks to her.

TABLE OF CONTENTS

LIST OF TABLES

LIST OF FIGURES

Chapter 1

INTRODUCTION

Crude oil contains many type of hydrocarbon compounds which are utilized through many succeeding processes. After removal of the salts, some hydrocarbons can be used in the market directly after distillation with small additional treatments. At the end of the distillation, significant amount of high boiling point materials, which have low market value because of market and environmental considerations, are also produced and they need further processing. Cracking is an important and wide process which is used to upgrade those heavy ends. In this process, heavy compounds are cracked to smaller molecules with lower molecular weight and boiling point. The cracking chemistry is very complex because of the content of the crude oil and the reaction mechanism. In addition, the analysis of the reaction media and the materials is limited in industrial applications. On the other hand, the modeling of those processes has crucial importance in the refinery to exploit all the economic potential while ensuring safety and product quality.

Mechanistic kinetic models are based on fundamental chemistry and they study the reaction mixture at the molecular level ([1, 2]). In order to facilitate the development of mechanistic models, different types of molecular lumping or partitioning techniques have been proposed to simplify the representation of the large-scale reaction networks. For example, in the structure-oriented lumping approach, hydrocarbon molecules are conveniently represented by a limited set of structural constructs which provide a useful framework for modeling and molecular property prediction ([3-5]). Each chemical species in the reaction media is represented by a vector notation whose elements provide information on a chemical structure. This information can be used to infer the cracking tendency and other intrinsic properties of overall molecule. In a similar effort, Martens and Marin [6] lumps (cyclo)alkanes and carbenium ions into structural classes of similar species and computes the lumping coefficients without generating the entire reaction network. This in turn decreases the computational burden of determining the kinetic rate constants. Klein and Hou [2] introduced a mechanistic kinetic modeling toolbox which classifies reactions into a set of reaction families and they have used a computer generated reaction network to estimate the rate parameters. Mechanistic models have good predictive capabilities in general but because of their complexity and large number of parameters involved, they have not found significant applications in industrial hydrocracking processes yet.

Real-time optimization of cracking process has been a crucial research and many different modeling approaches have been proposed in the literature depending on different processes. Hydrocracking and Fluid Catalytic Cracking (FCC) are the most popular cracking processes in the refineries. Although the basic idea behind the processes is similar, there are many different driving forces in the two processes, which requires the development of novel and case specific expressions. Most models in the literature lack the flexibility for industrial implementations.

The cracking processes are exposed to many disturbances and unknown driving forces. The complexity of the process motivates the development of hybrid models which incorporate the first principle expressions with empirical correlations. The primary objective of this study is to derive practical process models to capture the effects in the process and their influences on the operating conditions and profitability using existing literature and real plant data.

In chapter 2, we focus on the continuous lumping approach which treats the complex reactive mixture as a continuum in an industrial hydrocracker plant. We develop a dynamic model for whole hydrocracker plant involving the cracking reactors and the fractionation unit which separates the effluent into final products. A hybrid model is constructed using the method of continuous lumping to derive novel first principle expressions for the reactors and empirical fractionation model. The model is validated using industrial data and a hierarchical coordinating control structure is implemented on the model to drive the plant to optimal operating regime.

The method of discrete lumping, which divides the complex reactive mixture into pure and discrete pseudo components, is used to model the reaction unit of an industrial Fluid Catalytic Cracker (FCC) plant in chapter 3. A practical nonlinear model is developed with high number of pseudo components. The properties of those are estimated from empirical correlations which make use of intrinsic properties with few parameters. An economic model predictive controller (EMPC) is constructed to provide optimal transition path among changing operating conditions in the whole operating window.

The last chapter includes the discussion of current approaches and possible future improvements in the area.

Chapter 2

CONTINUOUS LUMPING AND APPLICATION TO HYDROCRACKER

2.1 Introduction

Hydrocracking is a catalytic process used in petroleum refineries for cracking the high-boiling, high molecular weight hydrocarbons to lower-boiling products like gasoline, naphtha, kerosene, diesel oil. Hydrocracking is an important and flexible refinery process because it can process a wide variety of gas oils to produce a spectrum of improved and valuable products which are low in sulphur and impurities. Environmental concerns and increased demand for low-sulphur diesel and high smoke point jet fuel have played a major role in the increased utilization of the hydrocracking technology.

Hydrocracking is carried out in the presence of hydrogen at high temperatures (260 – 495°C) and pressures (35 – 200 bar). The main reactions are cracking and hydrogenation. In order to support both cracking and hydrogenation, bifunctional catalysts such as bimetallic compounds (e.g. NiMo) deposited on an acidic support (e.g. silica-alumina) are used. The acidic site facilitates cracking while the metallic site provides the hydrogenation function. Although cracking reaction itself is endothermic, the overall hydrocracking process is exothermic since hydrogenation is highly exothermic.

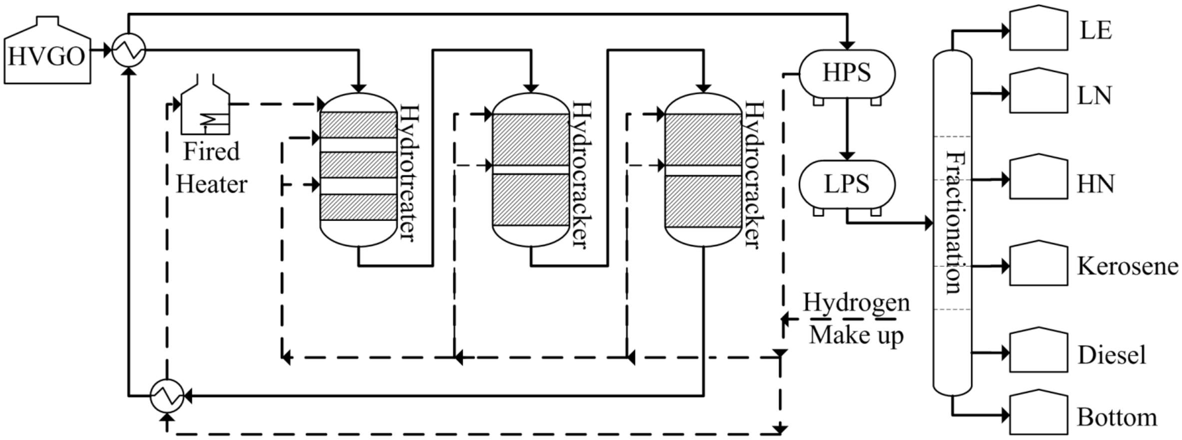

Figure 2.1: Process flow diagram of hydrocracking in the refinery.

A simplified hydrocracking plant flow sheet is shown in Fig. 2.1. The heavy vacuum gas oil is preheated with effluent of the reactor and combined with the hydrogen which is heated in fuel fired heater before entering the first stage of hydrocracker which is called hydrotreater. In the hydrotreater, sulfur and nitrogen compounds are converted to hydrogen sulfide and ammonia which are subsequently removed. At the same time any olefins and aromatics present in the feed are hydrogenated. Both of these processes require hydrogen consumption. A limited amount of hydrocracking takes place in the hydrotreater since the catalyst has higher hydrogenation activity than cracking. When the hydrotreater consists of multiple catalytic beds, hydrogen quench is used for inter-stage cooling as shown in Fig.2.1. The liquid effluent from the hydrotreater next enters the hydrocracker where most of the cracking takes place in the liquid phase. Hydrocracking units are trickle bed reactors in which the liquid phase consists of the heavy gas oil feed; hydrogen is in the gas phase and the catalyst constitutes the solid phase. Hydrocracking chemistry is complex and includes many reactions such as hydrogenation/dehydrogenation, beta scission, and isomerization ([1, 6]).

The liquid effluent from the hydrocracker is essentially free of sulfur and nitrogen impurities and consists mostly of saturated hydrocarbons. The reactor output is combined with water to reduce the corrosion of ammonia on the pipes and the effluent is supplied to a high pressure separator (HPS) where it is separated into hydrogen rich gas, liquid hydrocarbon and water. The hydrogen-rich gas is mixed with hydrogen make-up and recycled back to the reactor section. The hydrocarbon liquid is sent to a low-pressure separator (LPS) where H_2S and NH_3 are recovered. Finally the liquid hydrocarbon product is fed into the fractionation section where it is separated into the products.

2.2 Modeling Approaches

Modeling of hydrocracking is a formidable task due to existence of a large number of molecular species participating in many complex reactions. In addition the feedstock characteristics can exhibit significant variability. Different modeling approaches to hydrocracking have been reported in the literature [7]. These approaches can be classified under either mechanistic kinetic modeling or lumped kinetic modeling. Mechanistic modeling is not applicable to industrial plants for various drawbacks. The complexity of the mechanistic models has motivated the development of simpler lumped kinetic models. The first class of such models is the discrete lumping models (see chapter 3) in which the reaction mixture is divided into discrete pseudo-compounds (lumps) based on a molecular property such as boiling point, molecular weight or carbon number distribution ([8-11]). Because of their simplicity, discrete lumped models have been applied to several hydrocracking systems. Stangeland [10] developed a discrete lumped kinetic model and applied it to a commercial hydrocracker to predict yields. Mohanty et al. [12] and Bhutani et al. [13] incorporated Stangeland’s kinetic model into a plug flow reactor model and they tuned the model parameters using industrial data.

Unlike discrete lumping, the continuous lumping method considers the reactive mixture as a continuum. Specifically, when the cracking mixture has very large number of components, it is treated as a continuous mixture in which concentrations are expressed as continuous distribution of some intrinsic property such as true boiling temperature. DeDonder [14] introduced this notion for the first time for the thermodynamics of mixtures with infinitely many components and phases. Later Aris and Gavalas [15] laid the theoretical foundation for reaction mixtures with infinitely many components. Chou and Ho [16] proposed a lumping procedure for continuous reaction mixtures. For nonlinear catalytic cracking reactions Cicarelli et al. [17] developed a formal solution based on continuous kinetic lumping and perturbation theory.

Continuous lumped models were applied to several industrial systems successfully. Laxminarasimhan et al. [18] presented a model that matched the experimental product yields of vacuum gas oil hydrocracking closely. Basak et al. [19] used the continuous lumping approach in their commercial units and was able to predict the product yields, hydrogen consumption and heat effects. In moderate hydrocracking of heavy oil, Elizalde et al. [20] found the error between experimental and model predicted data to be lower than 5% for all the operating conditions. Lababidi et al. [21] and Elizalde et al. [20] reported that continuous lumped models show better predictive power than their discrete counterparts.

When compared with mechanistic and discrete models, continuous lumped models are easier to develop and tune since they are not derived at the level of molecular detail and they have fewer number of modeling parameters to estimate. At the same time they are known to possess good predictive capabilities. For these reasons, we have chosen the continuous lumping framework to model hydrocracking. Our ultimate goal is to use the developed model for optimization and control of an industrial unit. For this reason, we want the model to capture the essential features of the industrial process without unnecessary details which can hinder its end use. Here we present the development of a first principle model which includes both reactor dynamics and nonisothermal conditions which, to the best of our knowledge, are not addressed by the steady-state models given in the literature. In order to set the stage for the presentation of such a reactor model, we first introduce the mathematical preliminaries as originally given in [16] and the continuous lumping procedure as applied to hydrocracking in [18].

2.3 Mathematical Preliminaries

For a mixture that has N reactant species, the total concentration at any given time t is given by:

$$C(t) = \sum_{i=1}^{N} c_i(t) \tag{2.1}$$

where $c_i(t)$ is the concentration of the i^{th} reactant that has reactivity k_i and $C(t)$ is the total concentration.

Chou and Ho [16] approximated the discrete mixture Eq. 2.1 by a continuous mixture where concentrations are continuous functions of reactivity k. In doing so they employed a coordinate transformation from discrete "i-coordinate" to continuous "k-coordinate". The one-to-one map between i and k is given by:

$$D(k_i) = \frac{\Delta i}{\Delta k_i} \tag{2.2}$$

As N approaches infinity, $D(k_i)$ becomes a continuous function of k and $D(k)dk$ represents the number of species with reactivity between k and $k+dk$. Thus $D(k)$ is a species-type distribution function that must satisfy the species conservation:

$$\frac{1}{N}\int_0^\infty D(k)dk = 1 \tag{2.3}$$

With these definitions, one gets the continuous representation of the discrete mixture:

$$C(t) = \int_0^\infty c(k,t)D(k)dk \tag{2.4}$$

where *c(k,t)* is the concentration of reactant with reactivity *k* at time *t* in the continuous mixture.

When Eq.2.4 is discretized on equally spaced *i*'s, one recovers the discrete mixture i.e.

$$\int_0^\infty c(k,t)D(k)dk \approx \sum_{i=1}^{N} c(k_i,t)D(k_i)\Delta k_i = \sum_{i=1}^{N} c(k_i,t)\frac{(\Delta i = 1)}{\Delta k_i}\Delta k_i = \sum_{i=1}^{N} c(k_i,t) = \sum_{i=1}^{N} c_i(t) \tag{2.5}$$

Thus the species-type distribution function $D(k)$ provides the consistency between discrete and continuous lumping. Experimental evidence suggests that hydrocracking reactivity increases monotonically with the True Boiling Point (TBP) following a power law type relationship [18]:

$$\frac{k}{k_{\max}} = \theta^{1/\alpha} \tag{2.6}$$

where α and $k_{\max}$ are parameters and θ is the normalized true boiling (TBP) point:

$$\theta = \frac{TBP - TBP(l)}{TBP(h) - TBP(l)} \tag{2.7}$$

In Eq. 2.7 *TBP(l)* and *TBP(h)* are the lowest and highest boiling points of the reaction mixture, respectively. $k_{\max}$ is the reactivity of species that has the highest boiling point. Using the definition of *D(k)*, i.e. Eq. 2.2, and noting that $\frac{di}{d\theta} \approx \frac{\Delta i}{\Delta \theta} = \frac{N}{1} = N$, one gets:

$$D(k) = \frac{di}{dk} = \frac{di}{d\theta}\frac{d\theta}{dk} = N\frac{\alpha}{k_{\max}^{\alpha}}k^{\alpha-1} \tag{2.8}$$

which satisfies the constraint given by Eq. 2.3.

It is this form of species-type distribution function $D(k)$ that has been used in all of the hydrocracking continuous lumping studies in the literature. Note that concentration *c(k,t)* depends on the feed concentration. However $D(k)$ depends only on the types of reactants present in the feed and it is independent of the concentration of each reactant.

2.3.1 The Yield Function

In hydrocracking, longer chain hydrocarbons crack to yield smaller chains. We let *K* and *k* represent the reactivities of longer and shorter chains, respectively. The yield function $p(k,K)$ represents the formation of the species with reactivity *k* from hydrocracking of heavier species that has reactivity *K*. Analyzing several experimental data on hydrocracking of paraffinic, aromatic and olefinic compounds, Laxminarasimhan et. al. [18] found that a skewed Gaussian-type distribution function can be used to describe the yield distributions closely. This yield function is only function of reactivity and is given by:

$$p(k,K) = \frac{1}{S_0\sqrt{2\pi}}\left[exp - [\{(k/K)^{a_0} - 0.5\}/a_1]^2 - exp(-(0.5/a_1)^2 + \delta(1 - k/K)\right] \tag{2.9}$$

Fig. 2.2 shows the typical yield curves for three different reactivities K. It is observed that for short hydrocarbons, with low reactivity, the peak of the yield curve is relatively narrower and higher since there is less species to crack. Conversely, the yield curve is wider for longer hydrocarbons that have higher reactivity. Also it should be noted that $p(k,K)=0$ for $k \geq K$ since cracking to longer hydrocarbons is not possible by definition. When k = 0, Eq. 2.9 becomes:

$$p(0,K) = \frac{\delta}{S_0\sqrt{2\pi}} \tag{2.10}$$

$p(0,K)$ should be a nonzero small number since the least reactivity components form in negligible amounts during cracking. Therefore the model parameter δ is taken as a small number and the remaining model parameters (a_0, a_1) in Eq. 2.9 are estimated to match the plant data. These two parameters are very critical as their values determine the distribution of the products that are formed upon hydrocracking.

The yield distribution function must satisfy the material balance constraint:

$$\int_0^K p(k,K)D(k)dk = 1 \tag{2.11}$$

which expresses the condition that the total yield must be equal to 1. In order to satisfy Eq. 2.11, the normalization factor S_0 is specified by:

$$S_0 = \int_0^K \frac{1}{\sqrt{2\pi}}\left[exp - [\{(k/K)^{a_0} - 0.5\}/a_1]^2 - exp(-(0.5/a_1)^2 + \delta(1-k/K)\right]D(k)dk \tag{2.12}$$

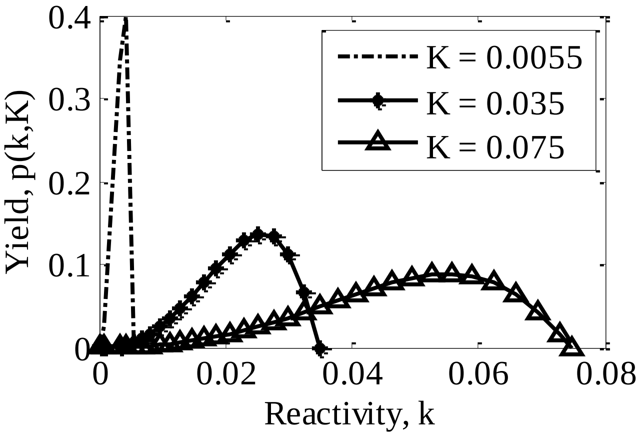

Figure 2.2. Yield distribution function $p(k, K)$

2.4 Development of the Reactor Model

Hydrocracking units are trickle bed reactors in which the liquid phase consists of the heavy gas oil feed, hydrogen is in the gas phase and the catalyst constitutes the solid phase. Each catalytic bed is separated by a quench zone that provides inter-stage cooling as schematically shown in Fig.2.3. In order not to unduly complicate the model, we assume a plug flow reactor operating under adiabatic conditions with excess hydrogen. Reactions are modeled as first-order pseudo-homogeneous reactions. Diffusional resistances, hydrodesulfurization and hydrodenitrogenation reactions are assumed negligible. Finally since hydrogen consumption is a small fraction of the feed (about 0.5%), the total mass flow rate of the liquid feed can be taken constant through the reactor beds. Similar simplifying assumptions have been used and found realistic by other researchers ([12, 13]). However, unlike all previous models in the literature, we do not assume steady state so that the developed model can be potentially used for dynamic analysis of the reactor behavior and its control.

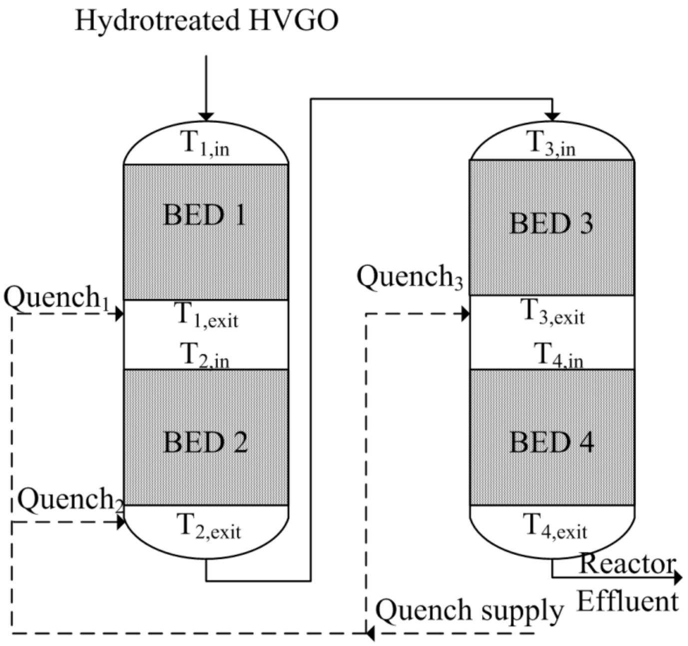

Figure 2.3: Schematic description of the reactors with the various process variables.

With the above assumptions, performing species mass balance in a shell of the liquid phase and letting the thickness of the shell become infinitesimally small, one gets the unsteady-state differential mass balance:

$$\frac{\partial c(k,z,t)}{\partial t} = -v\frac{\partial c(k,z,t)}{\partial z} - k_0 e^{-\frac{E_a}{R}\left(\frac{1}{T_0}-\frac{1}{T}\right)} c(k,z,t) + \int_k^{k_{max}} p(k,K).K_0 e^{-\frac{E_a}{R}\left(\frac{1}{T_0}-\frac{1}{T}\right)} c(K,z,t)D(K)dK \tag{2.13}$$

where $c(k,z,t)$ is the mass fraction of species with reactivity k at axial position z at time t ; v is the mass average velocity; E_a is the activation energy; k_0 and K_0 are reactivities at some reference temperature T_0. The term on the left hand side of Eq. 2.13 denotes the accumulation of mass; the first term on the right hand side is the net rate of addition of mass by convection;

the second term is the consumption of the species with reactivity k due to its cracking to lighter species; and the last term is the generation of the species with reactivity k by cracking heavier species. The mass-balance Eq. 2.13 is expressed in the continuous k-domain. Its discrete analog is given by:

$$\frac{\partial c_i(z,t)}{\partial t} = -v\frac{\partial c_i(z,t)}{\partial z} - k_0 e^{-\frac{E_a}{R}\left(\frac{1}{T_0}-\frac{1}{T}\right)} c_i(z,t) + \sum_{j,j>i}^{N} p_{ij} k_0 e^{-\frac{E_a}{R}\left(\frac{1}{T_0}-\frac{1}{T}\right)} c_j(z,t) \qquad (2.14)$$

where c_i is the concentration of the i^{th} species in the discrete mixture; p_{ij} is the yield of j^{th} species to form the i^{th} species upon cracking.

Under steady state and isothermal conditions at $T = T_0$, Eq. 2.13 reduces to the continuous lumping model given in the literature [18]:

$$v\frac{dc(k,z)}{dz} = -k\, c(k,z) + \int_k^{k_{max}} p(k,K).Kc(K,z)D(K)dK \qquad (2.15)$$

In the literature continuous lumping models for hydrocrackers do not include the energy balance and as such they cannot predict the temperature effects in a general setting. Here by carrying out an energy balance in the liquid phase, we get:

$$\frac{\partial T(z,t)}{\partial t} = -v\frac{\partial T(z,t)}{\partial z} + \frac{\int_0^{k_{max}} k_0 e^{-\frac{E_a}{R}\left(\frac{1}{T_0}-\frac{1}{T}\right)} c(k,z,t)(-\Delta H_r^o(k))D(k)dk}{\int_0^{k_{max}} c(k,z,t)C_p(k)D(k)dk} \qquad (2.16)$$

Hydrogen is not included in the derivation since it is assumed to be totally in the gas phase. In Eq. 2.16 $C_p(k)$ is the specific heat capacity for the species with reactivity k; and

$\Delta H_r^o(k)$ is the heat of cracking reaction for the species with reactivity k. An average value of activation energy E_a is assumed for the gas oil across all species as suggested by Quader and Hill [8] and used by Mohanty et al. [12] and Bhutani et al. [13].

In order to solve the integro-differential reactor equations Eq. 2.13 and 2.16, one needs to specify the initial concentration distribution of the feed i.e. $c(k,0)$. In order to determine $c(k,0)$, first the feed is divided into N lumps (or pseudo-components) where each pseudo-component boils in a particular temperature range and contributes to the feed by its weight fraction given by:

$$w_i = \int_{k_{i-1}}^{k_i} c(k,0)D(k)dk \qquad \text{for } i = 1,2,..,N \tag{2.17}$$

where the limits of integration on reactivity can be mapped to the boiling points by $k_i = k_{\max}\theta_i^{1/\alpha}$ and $k_{i-1} = k_{\max}\theta_{i-1}^{1/\alpha}$ due to the transformation between reactivity and true boiling point as given by Eq. 2.6.

When the weight fraction data are available, $c(k,0)$ can be obtained by inverting Eq. 2.17 subject to the constraint:

$$\sum_{i=1}^{N} w_i = 1 = \int_{0}^{k_{\max}} c(k,0)D(k)dk \tag{2.18}$$

In the hydrocracker unit under study the feed samples can only be taken from the fresh feed at the entrance of the hydrotreater. The hydrotreater produces significant amount of H_2S and NH_3 at high pressures. Therefore it is not possible to collect samples at the exit of the hydrotreater to characterize the feed entering the first bed of the hydrocracker. Since cracking in the hydrotreater is negligible compared to the first bed, we have assumed that the properties of the feed entering the first bed remains the same as the fresh feed entering the hydrotreater, except for nitrogen and sulfur content.

After the weight fractions of the feed are determined, we use a method developed by Riggs and Govindhakannan [22] to solve Eqn. 2.17 and 2.18 for $c(k,0)$. In each interval $k_{i-1} \le k \le k_i$, $c(k,0)$ is represented by a linear interpolation, and the resulting set of algebraic equations are solved through an optimization problem to give the initial values of the concentration profile for N pseudo-components i.e. $c(k_1,0), c(k_2,0), ..., c(k_N,0)$.

Using the initial concentration of the feed constructed by the above method and the known value of the reactor inlet temperature, the nonlinear integro-differential equations Eqn. 2.13 and 2.16 were solved numerically by using the method of finite differences and applying the trapezoidal rule to evaluate the integrals.

In our case there are six individual products: Light Ends (LE), Light Naphta (LN), Heavy Naphta (HN), Kerosene (Krs), Diesel (Dsl) and Bottoms (Btm) (see Fig.2.1). Each product is characterized by a particular TBP cut $[\theta_1, \theta_2]$. After the product concentration distribution $c(k,z,t)$ is calculated by solving the differential equations, the weight fraction of each product can be determined from:

$$w_{1,2}(z,t) = \int_{k_1}^{k_2} c(k,z,t) D(k) dk \tag{2.19}$$

where $k_1 = k_{\max}\theta_1^{1/\alpha}$ and $k_2 = k_{\max}\theta_2^{1/\alpha}$. This product distribution can then be compared with the actual plant data (see the model and plant comparison).

2.4.1 Determination of Heat Capacity and Heat of Reaction

The reactor model requires the knowledge of distribution of heat capacity and the heat of reaction as a function of reactivity *k*. Mohanty et al. [12] has calculated the heat capacities of the individual (pseudo) components of a discrete lumped model using Peng-Robinson equation of state, fugacity coefficients and excess enthalpy.

It is observed from the calculations that heat capacity monotonically decreases with TBP. In particular it decreases linearly in the higher TBP range which covers most of our operating conditions. When we computed the heat capacities using HYSYS and existing correlations in the literature [23], we have observed the same trend. At the same time, heat capacity correlations for petroleum fractions in the liquid phase can be in error as much as 20% [24]. Therefore, instead of using a particular correlation, we have determined the heat capacity from a linear relationship:

$$C_p(k) = a.\theta(k) + b \tag{2.20}$$

The parameters *a* and *b* are estimated from actual plant data in the following way. The hydrocracker unit consists of four catalytic beds separated by three quench zones. The product from each bed is cooled down by the hydrogen quench before it enters the next bed. Energy balance for each quench zone provides the following equation:

$$\dot{m}_Q\left(T_{set} - T_{Hydrogen}\right)C_{p,Hydrogen} = \left[\dot{m}_p C_{p,product} + \dot{m}_H C_{p,Hydrogen}\right]\left(T_{exit} - T_{set}\right) \tag{2.21}$$

where $\dot{m}_Q$ is the hydrogen quench mass flow rate; T_{exit} is the product temperature at the exit of one bed and T_{set} is the desired set-point value for the inlet temperature of the succeeding bed; $\dot{m}_{\mathrm{p}}$ is the mass flow rate of the liquid product in the quench zone; $\dot{m}_{\mathrm{H}}$ is the mass flow rate of hydrogen leaving the bed with the product; T_{Hydrogen} is the inlet temperature of hydrogen quench; $\mathrm{C}_{p,Hydrogen}$ is the heat capacity of hydrogen; and $\mathrm{C}_{p,product}$ is the average heat capacity of reactor product. The average heat capacity of the product can be expressed in terms of the pseudo-component heat capacities and their weight fractions:

$$C_{p,product} = \sum_k w(k)C_p(k) = \sum_k w(k)(a.\theta(k) + b) \tag{2.22}$$

In Eq. 2.21 and 2.22 all the variables are available or measured except the parameters *a* and *b*. Therefore these parameters are estimated by least squares using plant data and the heat capacity for each pseudo-component follows from Eq. 2.20.

There is experimental evidence that heat of hydrocracking is mostly governed by hydrogen consumption [25] and it varies almost linearly with hydrogen consumed during hydrocracking [26]. In order to compute the hydrogen consumption, carbon-to-hydrogen (C/H) weight ratio as a function of reactivity is needed. C/H ratios for hydrocarbons have been shown to monotonically increase with the boiling point [27]. Correlation [28] that is used in this study to estimate C/H ratio from boiling point also supports this.

Once (C/H) ratios are available, hydrogen consumed in cracking of each species can be easily calculated [12]. Next the standard heat of reaction for species with reactivity *k* can be computed from:

$$\Delta H_r^o(k) = -HC(k)(42)10^3 / 2 \quad (kJ / kg\, hydrocarbon). \tag{2.23}$$

where *HC(k)* is the amount of hydrogen consumed in the cracking of species with reactivity k. In Eq. 2.23, a typical literature value of 42 MJ of heat release per kmol of hydrogen consumed is used [26]. Using Eq. 2.23, we have computed the heat of reaction for different reactivities or TBP's. For most of the operating range of interest to us, the behavior of standard heat of reaction versus TBP is almost linear as in the case of heat capacities.

Therefore, the following linear expression can be used:

$$\Delta H_r^o\ (k) = c.\theta(k) + d \tag{2.24}$$

where *c* and *d* are adjustable parameters that will be estimated to match the plant data.

Note that in Eq. 2.24, the standard heat of reaction $\Delta H_r^o(k)$ is used for the heat of reaction at the reactor operating conditions $\Delta H_r(k)$, since the sensible heat effects were found negligible, for our operating temperatures. This is in line with the observations made in [25].

2.4.2 Calculation of Hydrogen Consumption

The hydrogen consumption can be computed from the hydrogen difference between the product and the feed:

$$\text{Hydrogen consumed per kg of feed} = \left[\sum_{\text{i,products}} \frac{w_i}{R_i + 1} - \sum_{\text{j,reactants}} \frac{w_j}{R_j + 1} \right] \tag{2.25}$$

where R_i is the carbon to hydrogen (C/H) weight ratio of i^{th} pseudo-component and w_i is the corresponding weight fraction. Since (C/H) ratios are available for the individual components, Eq. 2.25 can be used to calculate the hydrogen consumption.

2.4.3 Calculation of Quench Flow Rates

Hydrogen quench flows are used between the reactor beds to provide inter-stage cooling and to keep the bed inlet temperatures at their desired set points. At the same time quench flows supply additional hydrogen for the hydrocracking reactions in the beds. In the absence of any catalyst, no reactions take place in the quench zones between the beds. After the bed exit concentrations are determined, the quench flow rate $\dot{m}_Q$ in each quench zone is calculated from Eq. 2.21 and 2.22.

2.5 Parameter Estimation

Parameter estimation is concerned with the problem of determining reasonable values for the model parameters from plant measurements so that the resulting model gives a good prediction of plant data. Like in many other industrial systems, the hydrocracker operates with a certain degree of variability in its feed properties, catalyst and operating conditions. Therefore a representative set of plant data must be used to estimate realistic values for the parameters.

For the training data we have chosen plant data that cover a period of almost two months. Considering a longer time period would introduce significant variability in catalyst activity and choosing a shorter time period would limit the range or predictive power of the model. Each data set in this study consists of the daily average values for the corresponding date.

Steady-state parameter estimation is formulated as a nonlinear weighted least-squares problem of the form:

$$\min_{\varphi} (X_p - X_m(\varphi))^T W (X_p - X_m(\varphi)) \tag{2.26}$$

where X_p is the vector of plant measurements and X_{m} is the vector of model predictions that depend on the parameter values φ. W is the weighting matrix. Plant measurements consist of the exit temperatures of four reactor beds and the weight fractions of six products (light ends, light naphta, heavy naphta, kerosene, diesel and bottoms) all collected under steady-state conditions. This makes a total of 10 measurements per each data set. There are 4 data sets corresponding to four daily averages.

Therefore,

$$X_p = \begin{bmatrix} x_p^1 \\ x_p^2 \\ x_p^3 \\ x_p^4 \end{bmatrix} \quad \text{and} \quad X_p^i = \begin{bmatrix} x_{p,1}^i \\ . \\ . \\ x_{p,10}^i \end{bmatrix} \quad \text{for } i = 1,2,3,4 \tag{2.27}$$

and similarly for X_m.

The parameter vector is given by:

$$\varphi = \begin{bmatrix} k_{max} & \alpha & a_0 & a_1 & E_{a1} & E_{a2} & E_{a3} & E_{a4} & c & d \end{bmatrix}^T \tag{2.28}$$

The first two parameters are associated with the reactivites. The third and the forth parameters are related to yield function. Next four are the activation energies in different beds and the last two parameters are for the heat of reaction. Note that the heat capacity parameters (*a*, *b*) are not included in the optimization since they are calculated separately from the energy balance in the quench zones as discussed earlier.

Nonlinear least squares (2.26) requires the data on the weight fractions of the products. It is customary to obtain the weight fractions of petroleum by performing TBP (True Boiling

Point) distillation using an industry- standard ASTM method in the laboratory. From these tests, distilled volume fractions of the feed are recorded as a function of temperature. From the volume fractions, weight fractions can be computed (e.g. using the oil manager of HYSYS) and plotted versus temperature to give the TBP curve (see Fig. 2.4 for TBP curve of each product, feed and reactor output). These data are obtained from the plant measurements as follows. First of all it is not possible to sample and perform a distillation assay on the reactor output before fractionation due to safety and other physical restrictions. Instead ASTM distillation is performed on each product obtained after fractionation. These individual ASTM distillation assays are used to construct the TBP curve for each product. Next the individual distillation assays are blended by the HYSYS oil manager to yield the total product's TBP curve. The results are summarized in Fig.2.4 for the products obtained by cracking a particular feed. As shown the total product starts to boil when light ends (LE) starts to boil; and the last drop of the total product boils when the last drop of the heaviest product, bottom boils.

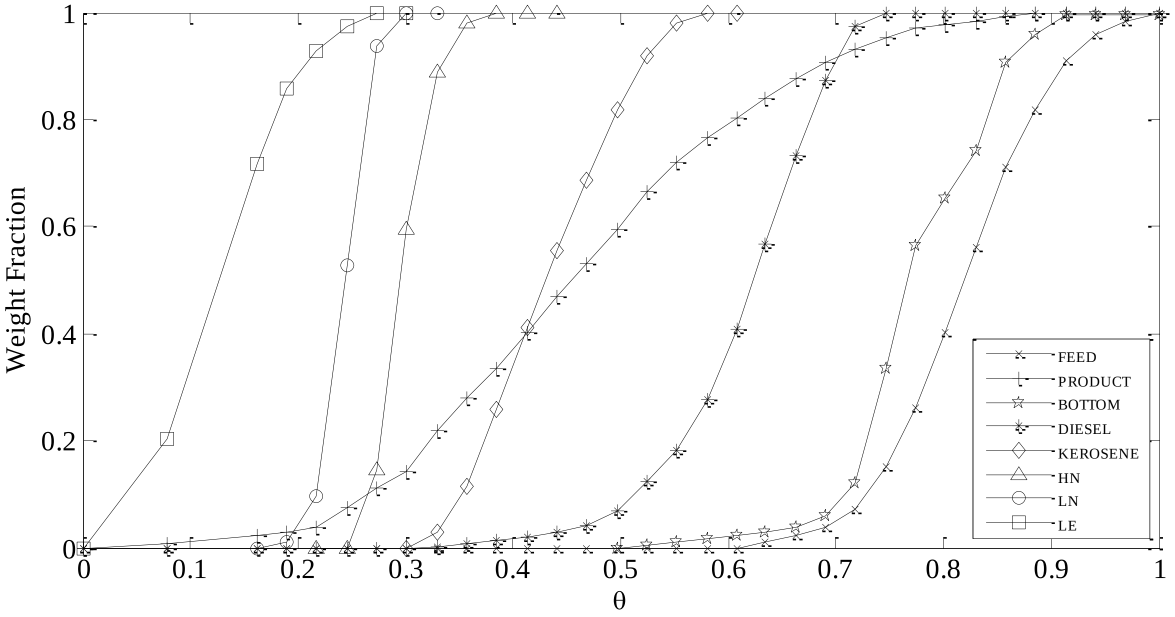

Figure 2.4: True Boiling Point distillation curves of individual products, and the total product for a particular feed.

As seen in Fig.2.4 TBP curves of certain products do usually overlap (e.g. LN and HN) indicating that the separation of "adjacent" cuts is not 100%. This has to be taken into account when calculating the individual weight fractions. We have used the temperature cut point concept [29] to calculate the individual product yields. For two "adjacent" products temperature cut point (*TCP*) is defined by

$$TCP = \frac{IBP(h) + FBP(l)}{2} \tag{2.29}$$

where *IBP(h)* is the initial boiling point of the heavy product, and *FBP(l)* is the final boiling point of the adjacent light product. For example, between LN and HN, the initial boiling point of HN, *IBP(h*), is 0.27 and the final boiling point of LN, *FBP(l),* is 0.30. Cumulative weight fractions corresponding to these temperatures are 0.110 and 0.145, respectively. It is certain that any material which boils at temperatures lower than 0.27 will be in LN, and any material which boils above 0.30 will be part of HN. In the overlap range 0.27-0.30 the distribution of the product between HN and LN will be determined by the cut point temperature. From Eq. 2.29 the calculated cut point temperature is 0.285 and the corresponding weight fraction is 0.125. Thus, the material which boils above 0.285 is assigned to HN, and the material boiling below is added to LN. In a similar fashion the cut point temperatures can be computed for all the products as shown in Fig. 2.5.

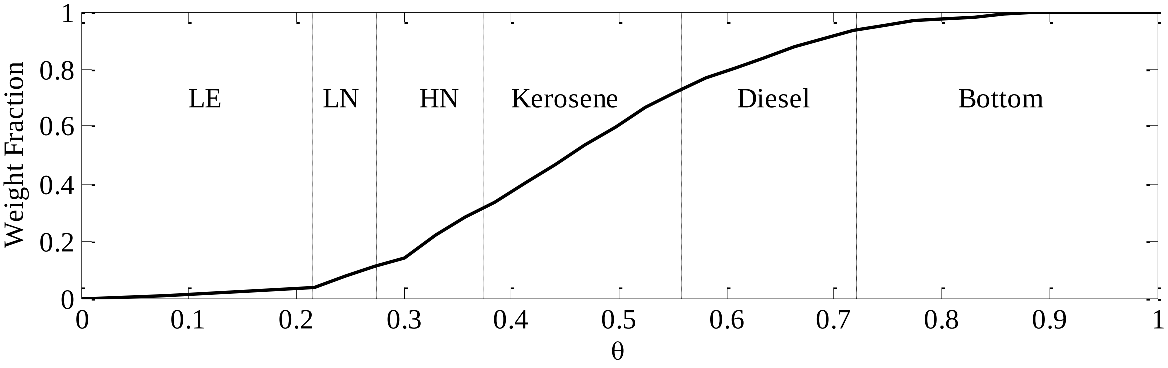

Figure 2.5: TBP curve and temperature cut points for different fractions.

Fractionation can be run at different temperature cut points by making the necessary adjustments in the distillation column. Table 2.1 lists the maximum and minimum values for the plant under this study. The temperature cut points are manipulated within those ranges according to the market conditions.

Table 2.1: Cut point data from plant

	Minimum Cut Point	Maximum Cut Point
LE – LN	0.203	0.229
LN – HN	0.265	0.305
HN – Krs	0.359	0.424
Krs – Dsl	0.497	0.579
Dsl – Btm	0.681	0.732

Starting from an initial guess for the parameter estimates, optimization problem (2.26) was solved subject to the ordinary differential equations (2.13) and (2.16) evaluated under steady-state conditions. Several initial runs with extensive steady-state operating data showed that some of the parameters are redundant or correlated. This lack of identifiability often occurs due to lack of data or the presence of large number of parameters ([30, 31]). In our case the identifiability problem persisted regardless of the additional measurements. Therefore among the parameter set φ, a subset of the most sensitive, identifiable parameters had to be chosen to determine reliable estimates. For this purpose Fisher information matrix was used [32]. According to the theorem of Cramer and Rao, the covariance of the inverse of Fisher information matrix is a lower bound for the covariance matrix of the parameter errors:

$$Cov(\hat{\varphi} - \varphi^{*}) \geq I_F^{-1}(\varphi^{*}) \tag{2.30}$$

where $I_F = \frac{1}{\sigma^2} F F^T$ is the Fisher information matrix and F is the Jacobian or sensitivity matrix of model outputs to the parameters; σ^2 is the variance of the measurement noise or output error; $\hat{\varphi} - \varphi^{*}$ is the error in the parameters with φ^{*} and $\hat{\varphi}$ being the true and estimated parameter values, respectively. In inequality (2.30) small eigenvalues of I_F will give large lower bounds and thus large covariances for the parameter errors. This means that certain parameters have poor (large) confidence intervals and cannot be identified. Following the algorithm proposed in [31], the number of parameters was successively reduced until the minimum eigenvalue of the Fisher information matrix is above a threshold value specified by the user. The eliminated parameters were treated as constant and not used for further tuning. Although different methods exist to recover from identifiability problems [32], this approach was found easy to use and gave good results. Among the parameter set, the identifiable ones were found to be: $\left[k_{max}, E_{a2}, E_{a3}, d\right]$. Their estimated values and confidence limits are listed in Table 2.2. As seen the confidence intervals are tight. Addition of more parameters to this set increased the confidence regions; therefore, parameter selection algorithm stopped at these four parameters.

Table 2.2. Estimated Parameters

Parameter	Nominal value	%95 confidence interval
k_{max}	0.0747	0.001
E_{a2}	235.01	1.42
E_{a3}	207.50	1.46
d	-136.70	1.23

2.6 Model Performance

Performance of the model after its parameters are tuned by parameter estimation is displayed in Table 2.3 for both training and validation. Actual bed exit temperatures, product yields and hydrogen flows are compared with the model's output. The model uses the same temperature cut points used during fractionation in the plant so that the same products can be compared. The agreement is remarkably good as seen from the listed magnitudes of average absolute deviation (AAD) between model predictions and plant data. Errors in product yields are less than 10% of the individual yields in most cases and less than 4% of the total. Temperature errors are less than a degree and are within process and measurement noise. In the plant hydrogen make-up keeps the total hydrogen constant. Therefore in Table 2.3 the total hydrogen consumption calculated by the model is compared with the amount of hydrogen make-up consumed in the plant. Prediction of hydrogen quench flows and hydrogen consumption are both acceptable as well. Maximum AAD for quenches and make-up is 6% and 4% of the nominal values, respectively.

Table 2.3. Comparison between model and plant for products, temperatures and hydrogen

	PRODUCTS	BED EXIT

		[% weight fraction]						TEMPERATURES [°C]			
		Btm	Dsl	Krs	HN	LN	LE	T_1	T_2	T_3	T_4
AAD[*]	TRAINING	1.2	3.8	0.2	2.3	1.3	1.5	0.4	0.7	0.2	0.2
	VALIDATION	0.4	1.6	1.8	0.7	1.1	1.3	0.4	0.5	0.3	0.4

		HYDROGEN FLOWS $[nM^3/h]$			
		$Quench_1$	$Quench_2$	$Quench_3$	Make-up
AAD	TRAINING	395.6	643	330.7	1015.5
	VALIDATION	564.6	714.1	266.5	520.9

[*] AAD stands for Average Absolute Deviation

Fig. 2.6 compares the calculated TBP curves of the product with plant data. Model-Product refers to the predicted TBP curve of the product leaving the fourth bed and Plant-Product refers to the TBP which is constructed by blending the individual fractionation products. The match is very good. The model predicts a slightly heavier product since its TBP curve is slightly to the right of the plant's TBP curve. Since product samples cannot be taken at the end of the beds, only the product profile for the exit of the 4th bed can be validated by the plant data. However we have also included in Fig. 2.6 the predicted TBP curves for the products at the end of each reactor bed. The model shows that starting with the feed, the TBP curves shift continuously to the left as the feed undergoes cracking in each subsequent bed. This is indeed the correct trend since the weight fractions of the lighter fractions increase as the amount of cracking increases with the number of beds.

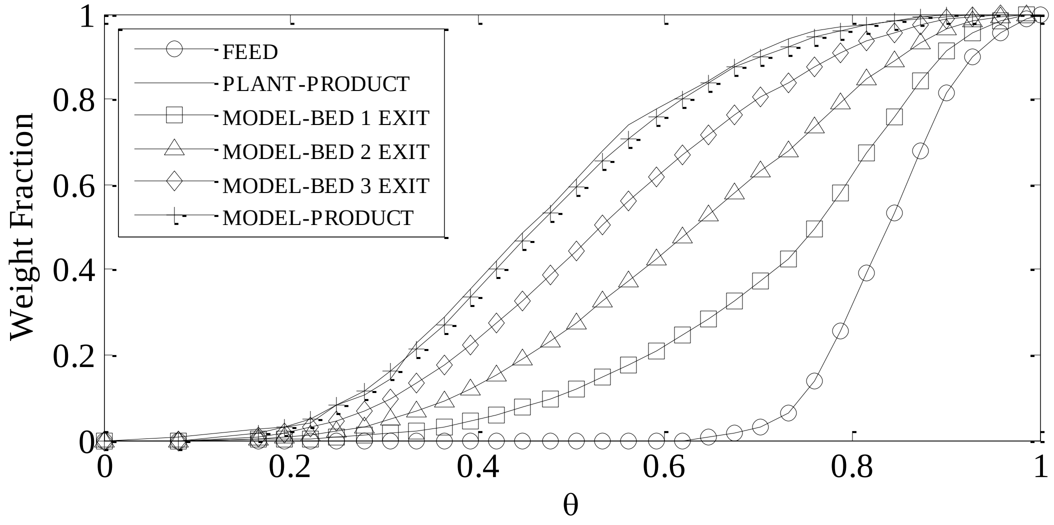

Figure 2.6: Comparison of Model and Plant TBP curves for a particular day under consideration.

After the model was tuned and validated under steady-state conditions, its dynamic performance was evaluated against transient plant data obtained from step testing. For this purpose the full dynamic model Eq. 2.13 and 2.16 were simulated using the step set-point changes made in the bed inlet temperatures as shown in Fig. 2.7. In the plant the bed inlet temperatures are controlled at their set-points by the quench controllers which manipulate the hydrogen quench flows. Therefore we have added to our reactor model a first order dynamic model for each quench zone which approximates the response of the inlet temperature to its set-point. These responses are shown in Fig. 2.7. Model-PV and Plant-PV indicate the reactor inlet temperature responses of the model and plant to the set-point changes, respectively.

Step changes greater than 0.5 ^{o}C are not allowed by the plant operators to prevent thermal runaways and guarantee operational safety. During the normal plant operation, if temperature changes greater than 0.5 ^{o}C are needed, they are implemented in increments of 0.5 ^{o}C.

Between each 0.5 ^{o}C change, pseudo-steady state is established before the next incremental change is made. Therefore the developed models using 0.5 ^{o}C changes are consistent with the requirements of the real plant operation. Finally 0.5 °C change in inlet temperature affects the bed exit temperature significantly enough (due to high sensitivity) to perform parameter estimation and model fitting.

First step change was made in the 4th bed inlet temperature, and after sufficient time elapsed, this was followed by successive decreases in 3rd, 2nd and 1st bed temperatures. In this fashion step response of each bed's outlet temperature to its inlet temperature was obtained as seen in Fig. 2.8. The model predicts the overall dynamic behavior of the plant quite well.

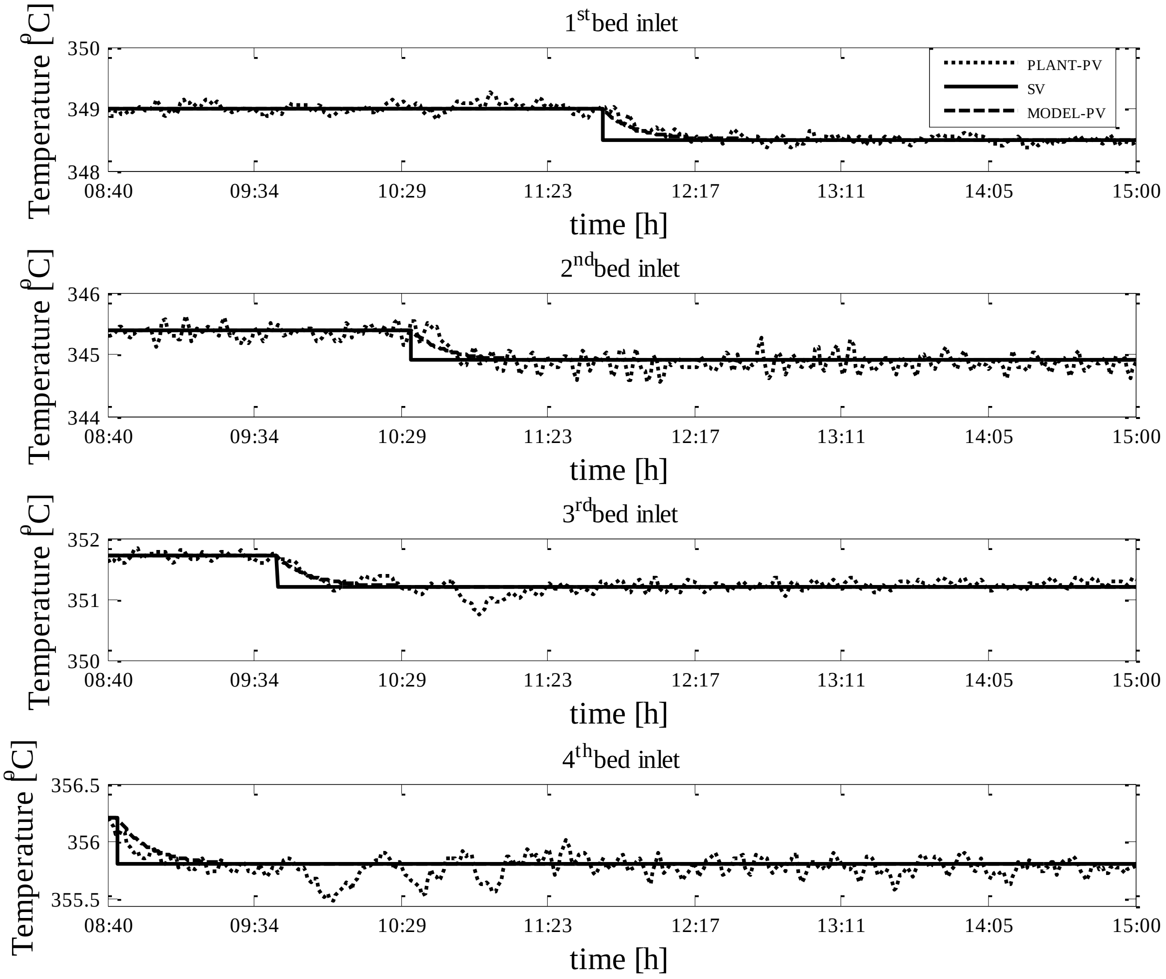

Figure 2.7: Bed inlet temperature changes.

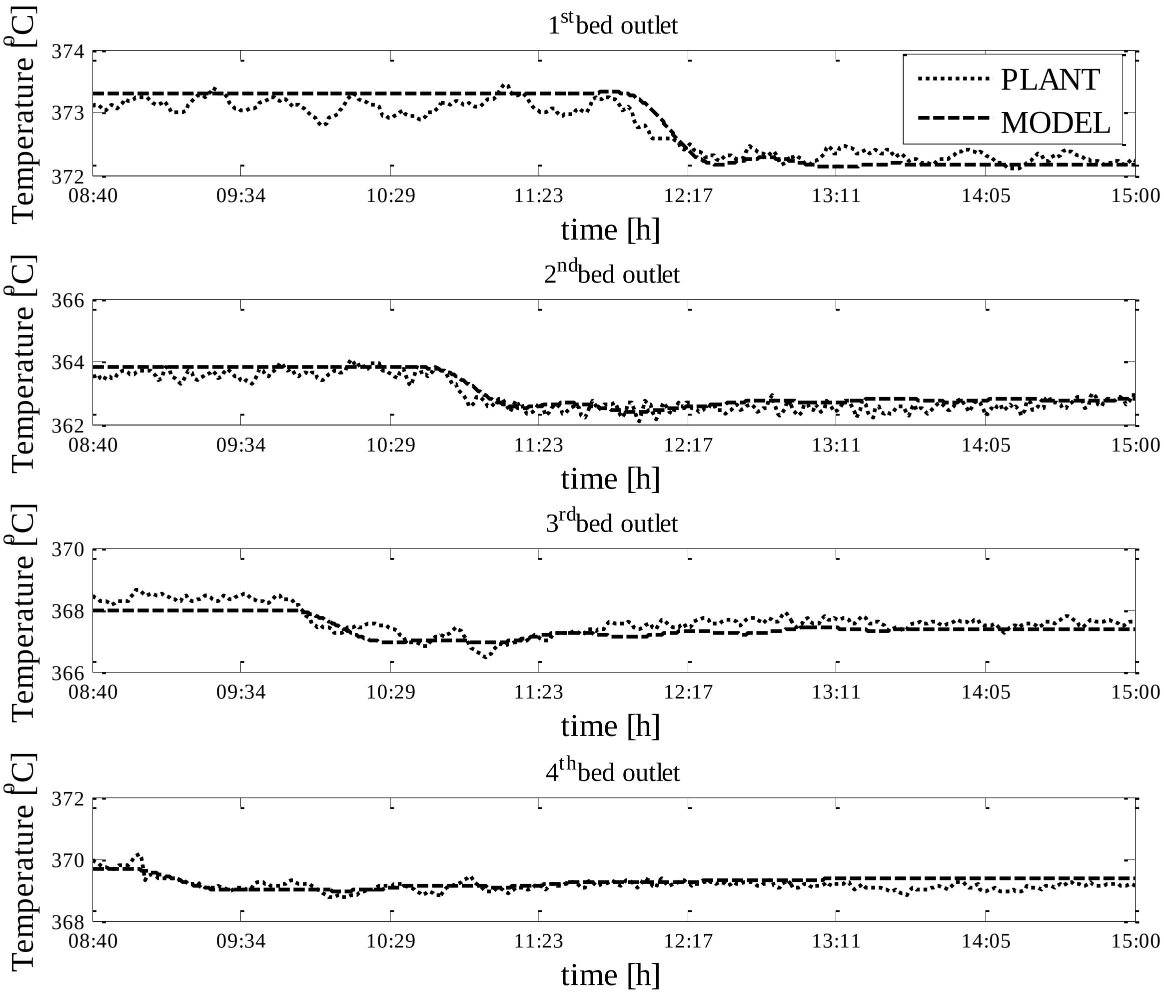

Figure 2.8: Bed exit temperature responses.

Finally we note that the parameters of the dynamic model were fixed at values obtained from steady-state estimation. Parameter estimation was done using steady-state data since the predictions were found in good agreement with plant data. We have also used a dynamic optimization algorithm to estimate the parameters from dynamic data. The difference between steady-state and dynamic parameter estimation was not found to be appreciable enough to warrant additional computational effort. The parameter values do not change significantly either when dynamic data are used. However, if it is deemed necessary, the dynamic model can be retuned on-line when it is put in use by a control system.

2.7 Potential Application Areas of the Model

Models are as good as they serve their intended purposes. In this regard steady-state models are usually developed and used for optimization purposes by which the best steady-state operating conditions are calculated. Similarly dynamic models are used for controlling the plant at its economically optimum operating conditions. Although steady-state optimization and control fall outside the scope of this paper, we have done a sensitivity analysis to study the relationship between the reactor operating conditions and the product distribution. The objective here is to see if the model has captured enough sensitivity which can serve as a basis for future optimization studies. Therefore we have chosen different product specifications and computed the reactor operating conditions that would give these products. This "inverse" problem is solved by:

$$\underset{\boldsymbol{T_{in}}}{minimize} \left\{ \sum_i (1 - \frac{x_{i,set}}{x_{i,\mathrm{m}}})^2 \right\} \tag{2.31}$$

$$T_{min} \le T_{in} \le T_{max} \tag{2.32}$$

where T_{in} is the vector of inlet temperatures; $x_{i,set}$ is the desired value of the weight fraction of the *i*-th product and $x_{i,m}$ is the modeled value of the same weight fraction. The decision variables are the bed inlet temperatures of four beds which are constrained due to safety considerations. In Table 2.4 reactor operating conditions that would yield various products are computed and compared with a base case. Since the aim here is to study the sensitivity and not to compute an economically optimal product profile, only one product specification is entered at a time. In this fashion the sensitivity of the reactor temperatures and other products can be calculated. For example when bottom product is reduced to 7% from its base value 8.1%, bed inlet temperatures must be increased to favor more cracking. Since more cracking occurs, there should be an increase in the lighter products. Both of these trends are correctly captured by the model as shown in Table 2.4. Similarly, in order to increase the weight fraction of the bottom product, bed inlet temperatures should be decreased as seen in 10% bottom case. In order to increase the diesel from 22.1% to 25%, temperatures should decrease as shown. In doing so the heavier adjacent fraction bottom increases as well and lighter fractions kerosene, naphtha and light ends decrease as expected. Results given in Table 2.4 showed that the model predicts correct trends and realistic reactor temperatures which are consistent with the plant operators' experience. Therefore one can conclude that the parameter values computed from least-squares (and equally important the chosen model structure) are realistic.

Table 2.4. Product and temperature profiles

	BASE	PRODUCTS			
		Bottom=7%	HN=19.5%	Bottom=10%	Diesel=25%
Btm	8.1	7.0	6.3	10.0	11.3
Dsl	22.1	20.8	19.9	23.9	25.0
Krs	40.2	40.6	40.8	39.3	38.7
HN	18.0	18.8	19.5	16.6	15.7
LN	7.4	8.0	8.4	6.6	6.1
LE	4.3	4.8	5.2	3.6	3.2
REACTOR OPERATING CONDITIONS					
$T_{1,in}$	344.6	345.1	345.4	344.4	343.8
$T_{2,in}$	343.0	343.8	344.4	341.6	340.8
$T_{3,in}$	348.8	349.6	350.2	347.4	346.6
$T_{4,in}$	350.9	351.8	352.5	349.3	348.3
$T_{1,exit}$	364.0	365.1	365.5	363.6	362.5
$T_{2,exit}$	360.2	362.0	363.5	357.0	355.4
$T_{3,exit}$	363.6	364.7	365.5	361.7	360.5
$T_{4,exit}$	363.1	364.1	365.0	361.0	359.9

We can conclude that the steady state model can be used in economic optimizations where product values and operating costs are taken into account and the optimal reactor operating conditions can be determined also.

2.8 Design of Control Structure

After the product concentration distribution *c(k,z,t)* is calculated by solving the reactor equations, the weight fraction of different species types i.e. pseudo-components can be calculated as a function of TBP of the mixture. RTO has to predict and optimize the amounts of individual distillation products. The TCPs in Fig. 2.5 provide mapping between pseudo components and final products which are obtained after the separation. In practice, TCPs are determined by the operations in the fractionation plant and online measurements of variables in Eq. 2.29 is not possible. For plant wide RTO purposes, TCPs must be estimated and controlled using measured variables.

Next let $P(\theta)$ define a polynomial that relates the normalized TBP θ to the corresponding cumulative weight fraction (see Fig. 2.4 and 2.5) of product mixture which satisfies the following:

$$P(1)=1 \tag{2.33}$$

$$P(0)=0 \tag{2.34}$$

The coefficients of $P(\theta)$ are determined using the least-squares approach to match the plant's TBP curve. There are 5 temperature cut points for 6 products as shown in Fig. 2.5. For instance, $\theta_{Dsl\text{-}Btm}$ is the cut point temperature between diesel and bottom product. Thus $\theta_{Dsl\text{-}Btm}$ should satisfy the following

$$P(\theta_{Dsl\text{-}Btm})=1-w_{Btm} \tag{2.35}$$

where w_{Btm} is the weight fraction of bottom product, which is measured in the plant. Similarly for $\theta_{Krs\text{-}Dsl}$

$$P(\theta_{Krs\text{-}Dsl})=1-w_{Btm}-w_{Dsl} \tag{2.36}$$

where w_{Dsl} is the weight fraction of diesel which is also measured. This procedure is followed to yield five temperature cut points for six products for each data set that cover 30 days of various processing regimes and operating conditions.

In the plant 95% boiling point temperatures (95%BPs) are controlled since these temperature values are typically used in the market as product specification. 95% boiling point temperature (95%BP) corresponds to the temperature at which 95% of the mixture is distilled as shown in Fig.2.3.

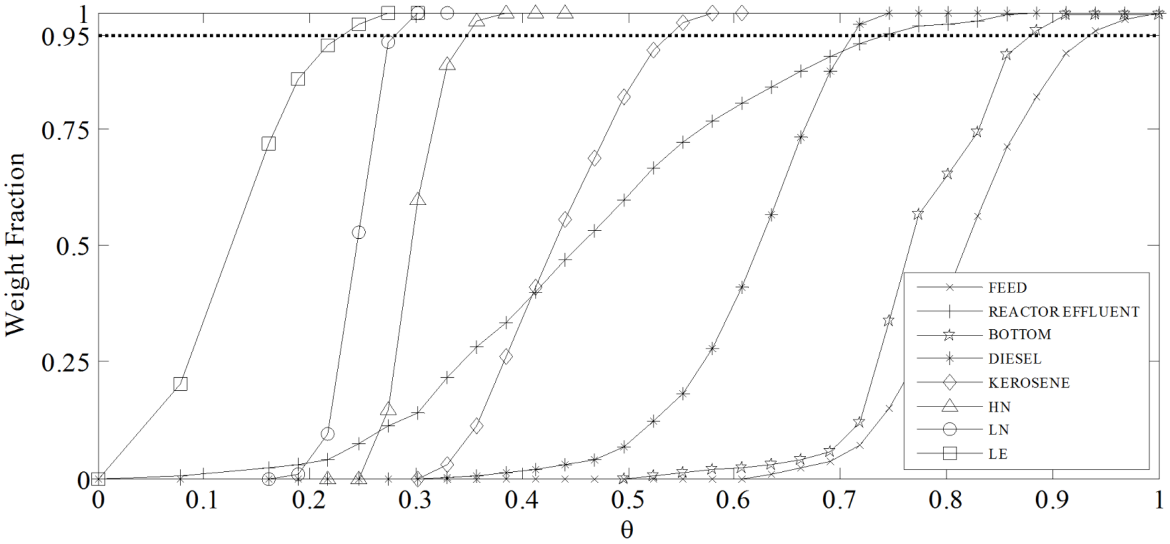

Figure 2.9: Product distillation curves and 95%°C boiling points.

The intersections of 95% weight fraction line with the individual curves specify the normalized 95%°C boiling points.

We should note that the reactor model predicts the true boiling point curve and the TCPs of the reactor effluent. However, the fractionator's control system controls the 95% BPs. Therefore, the true boiling point curve must be related to the 95% BPs to predict the effect of reactor operating conditions on the distillation product distribution. To this end, an empirical model between 95%BPs and the TCPs were developed based on historical plant data. The relationship between 95%BP and corresponding TCP is presented in Fig. 2.10.

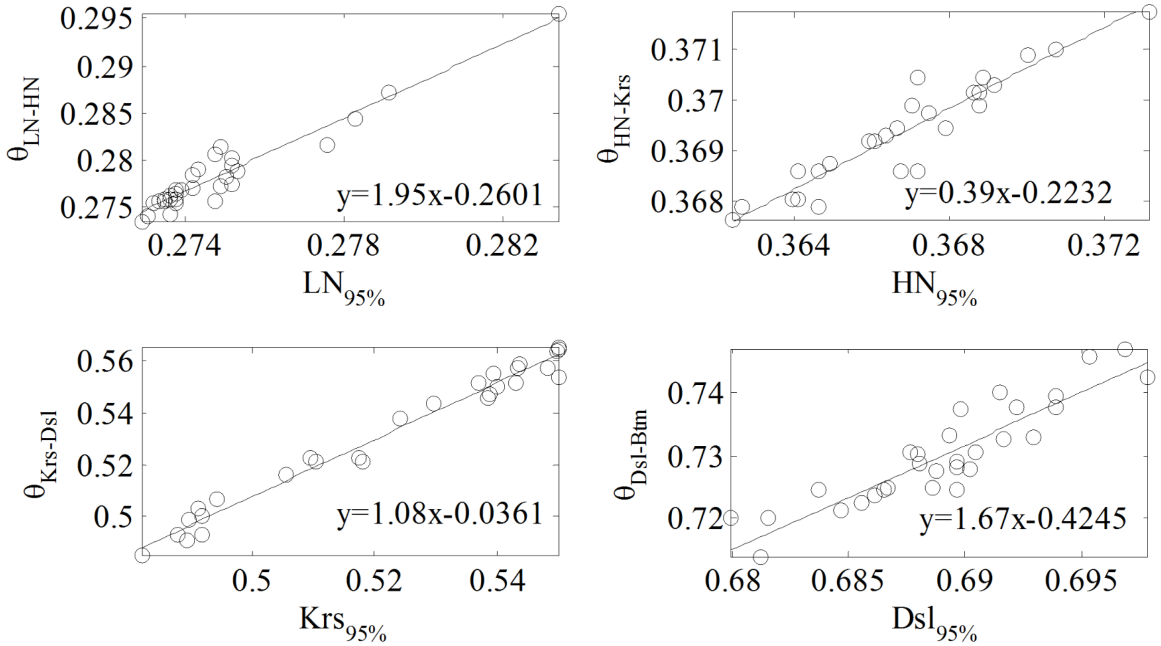

Figure 2.10: Cut point and 95% BP relationship.

Since online adjustment of 95%BP of LE is not practical in the refinery, $\theta_{LE\text{-}LN}$ is kept constant at all times. Thus, there are four adjustable TCPs as shown in Fig. 2.10.

The existing fractionation control system in the plant is an MPC controller. This local MPC controller is responsible for the control of four 95% BPs (LN, HN, Krs, Dsl). There are eight manipulated variables available. These are: fractionator top pressure, fractionator top temperature, kerosene withdrawal rate, diesel withdrawal rate, fractionator middle reflux, splitter top pressure, splitter middle tray temperature and splitter reflux. These variables are shown in Fig. 2.11. Product withdrawals are the primary manipulated variables. Increasing the product withdrawal directly increases 95%BP of the corresponding product by withdrawing heavier hydrocarbons that would be otherwise moving down the column. In the plant 95% BPs are estimated by an on-line soft sensor that uses an empirical model which predicts the 95% BPs from tray temperatures and the column pressure readings. The temperature and pressure of trays from which products are withdrawn show high correlation with the corresponding 95% BPs of the products. The locations of the pressure and temperature transmitters are marked by PT and TT in Fig.2.11. The model has been built using historical data and is updated on-line on a daily basis when the laboratory distillation assay measurements become available [33].

For MPC design and implementation, step response models between eight manipulated variables and four 95% BPs have been constructed from actual plant data. The existing MPC controller uses these step response models and is able to control the 95% BPs satisfactorily. Since the operating range of the 95% BPs is narrow, the effect of plant-model mismatch on control performance is acceptable. We have used these step response models in our plant-wide control system design and simulations.

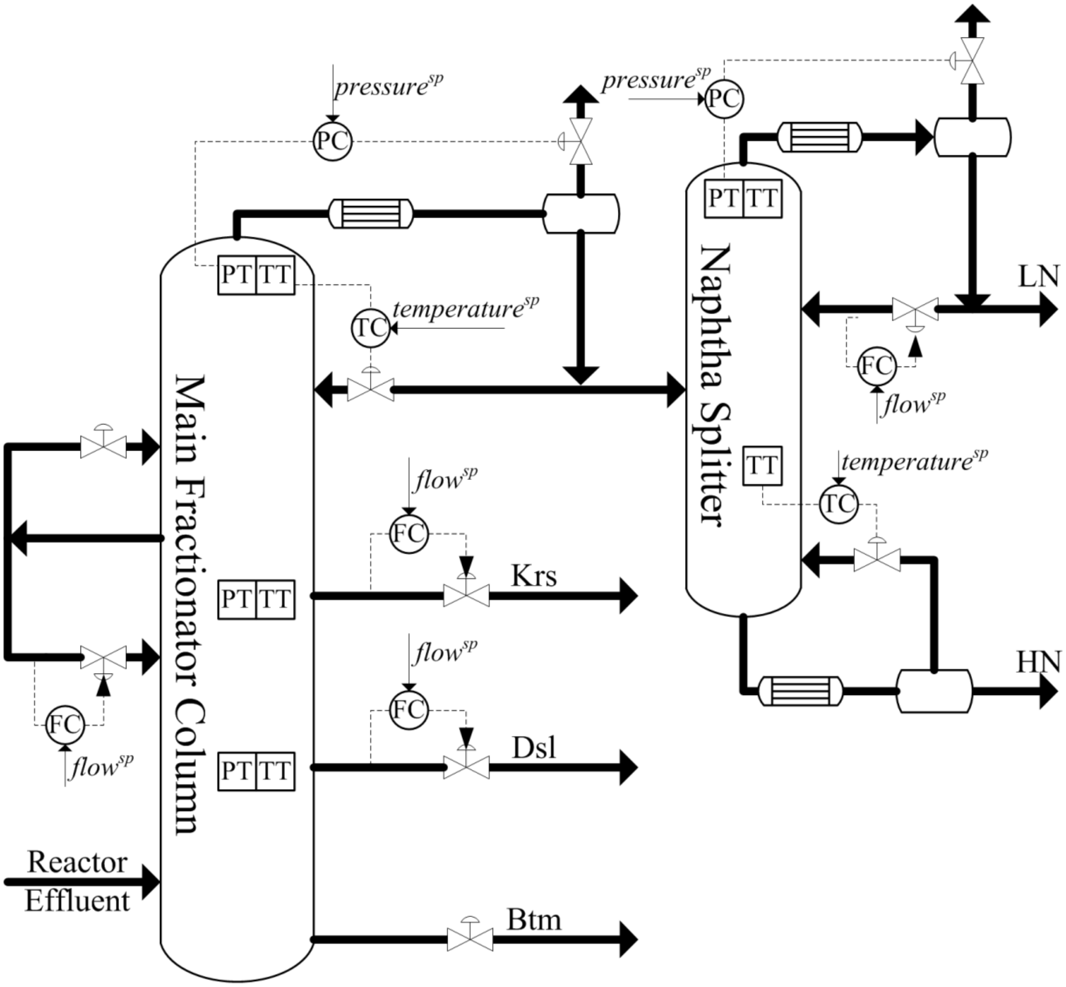

Figure 2.11: Fractionation subsystem with its controlled outputs and manipulated variables.

Other than 95%BPs, kerosene and diesel have flash points that should satisfy minimum levels for safety purposes. In the literature, various empirical correlations are derived for prediction of flash point of diesel and kerosene [34]. We have correlated the flash point with the 95%BPs using a linear multivariable fit:

$$T_{F,Krs} = -19.16+0.4045\cdot HN_{95\%}+0.02105\cdot Krs_{95\%} \tag{2.37}$$

where $T_{F,Krs}$ is the flash point of kerosene (°C), $HN_{95\%}$ is the 95%BP of HN; $Krs_{95\%}$ is the 95%BP of kerosene. It must be noted that the flash point of kerosene is estimated from the properties of two adjacent products. A similar approach is used for diesel flash point estimation which gives:

$$T_{F,Dsl} = 32.34+0.06073\cdot Krs_{95\%}+0.08035\cdot Dsl_{95\%} \tag{2.38}$$

where $T_{F,Dsl}$ is the flash point of diesel (°C); $Krs_{95\%}$ is the 95%BP of kerosene; $Dsl_{95\%}$ is the 95%BP of diesel. Finally, heavy naphtha has a 5% boiling point temperature constraint ($HN_{5\%}$). $LN_{95\%}$ (95%BP of LN) and $HN_{95\%}$ (95%BP of HN) are used to estimate the 5% boiling point temperature of HN:

$$HN_{5\%} = 31.61+0.2603\cdot HN_{95\%}+0.5086\cdot LN_{95\%} \tag{2.39}$$

Fig. 2.12 shows the prediction errors of the above product property models. In all cases the prediction errors are at acceptable levels (i.e. within the limits set in the plant). In addition model parameters can be updated on-line and predictions improved as new measurements become available.

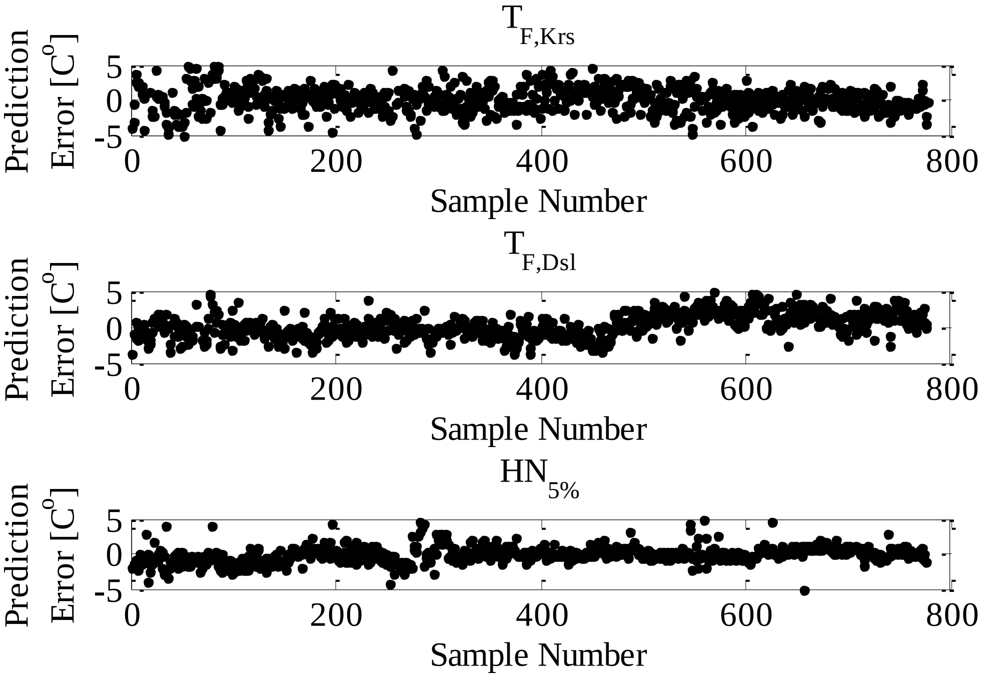

Figure 2.12: Prediction errors of product property models.

2.8.1 Control Problem Formulation

2.8.1.1 Operational Constraints

The hydrocracking plant is highly complex with many correlated process variables. Several important process constraints limit the operation of the reactor and the fractionator. Constraints on the exothermic reactor beds are well defined by the plant engineers and the catalyst company. Both bed exit and inlet temperatures are constrained to maintain safe operation without thermal runaway. Hydrogen is produced from natural gas or gasoline which in turn limits the make-up hydrogen consumption in the plant. Similarly, quench flows which are used for inter-stage cooling are limited by the available hydrogen in the plant and for safety issues a minimum quench amount is required. The catalyst is uniformly distributed in each reactor bed. Therefore Weighted Average Bed Temperature (WABT) is equal to the average bed temperature given:

$$WABT = \frac{\int_0^L T(z)dz}{L} \tag{2.40}$$

where L is the length of the bed and $T(z)$ is the temperature at axial position, z. For each bed WABT and temperature rise (ΔT) have to be regulated within limits to keep the catalyst active. Thus the constraints for the hydrocracker are:

Reactor bed inlet and exit constraints:

$$\begin{gathered} T_{in,min_i} \le T_{in,i} \le T_{in,max_i} \quad i = 1,2,3,4 \\ T_{exit,min_i} \le T_{exit,i} \le T_{exit,max_i} \quad i = 1,2,3,4 \end{gathered} \tag{2.41}$$

Reactor bed temperature rise and weighted average temperature constraints:

$$\begin{gathered} 0 \le \Delta T_i \le \Delta T_{max,i} \quad i = 1,2,3,4 \\ WABT_{min_i} \le WABT_i \le WABT_{max_i} \quad i = 1,2,3,4 \end{gathered} \tag{2.42}$$

Hydrogen make-up and quench flow constraints:

$$\begin{gathered} Q_{makeup} \le Q_{makeup,max} \\ Q_{min_i} \le Q_i \le Q_{max_i} \quad i = 1,2,3 \end{gathered} \tag{2.43}$$

Above temperatures and flow-rates are all measured in the plant.

In the fractionator 95% boiling point temperatures must be within ranges determined by the market and refinery requirements. In addition kerosene and diesel products must have flash-points above their safe limits; thus, they are constrained as well. Heavy naphtha has a

5% boiling point temperature constraint ($HN_{5\%}$) determined by the downstream processing in the gasoline unit. Thus, the fractionator constraints related to the product specifications are given by:

$$\begin{aligned}
&95\%BP_{min,i} \le 95\%BP_i \le 95\%BP_{max,i} \qquad i=1,2,3,4\\
&T_{F,Krs,min} \le T_{F,Krs}\\
&T_{F,Dsl,min} \le T_{F,Dsl}\\
&HN_{5\%,min} \le HN_{5\%}
\end{aligned} \tag{2.44}$$

2.8.1.2 Economic Objective

Any advanced process control system has to satisfy the above operational constraints. In addition, the plant has to be operated in the most profitable fashion. For a given HVGO feed, the total profit of the hydrocracker plant is given by:

$$\Phi = \left[\sum_{i=1}^{6} w_i p_i - Q_H p_H - p_f\right] m_f \tag{2.45}$$

where w_i is the weight fraction of i^{th} product, p_i is the corresponding price ($/kg), Q_H is the hydrogen consumption per kg of feed, p_H is the price of hydrogen ($/kg), m_f is the mass flow rate of the liquid feed (kg/h) and p_f ($/kg) is the cost of the feed. In Eq. 2.45 the hydrogen consumption Q_H is a function of the weight fractions of the product. Therefore for a given feed and set of prices, the objective function Φ is solely determined by the weight fractions i.e. $\Phi=\Phi(\boldsymbol{w})$ where $\boldsymbol{w}=[w_1\ w_2 \ldots w_6]^T$. Reactor bed inlet temperatures and the 95% boiling point temperatures are the major independent variables which affect the weight fractions of products and thus the profit.

2.8.1.3 Disturbances

Different types of disturbances can influence the operation of the hydrocracking plant. These disturbances can be classified according to their frequencies and impact [35]. Slow disturbances with high economic impact require re-optimization and may initiate a change in the steady-state operating conditions. The feed stock quality (e.g. aromaticity, chemical structure etc.), catalyst deactivation, product and hydrogen prices belong to this class of disturbances. These changes may persist for days or weeks depending on the crude feedstock and market demand. For such cases the model parameters can be updated on-line and steady-state economic optimization is performed to determine the new operating conditions. Since these disturbances do not change frequently, the plant-wide controllers will have enough time to make the necessary transition between the steady-state operating points. For faster disturbances or for those without significant economic impact, on-line optimization is not warranted. The temporary excursions caused by these disturbances are handled by the regulatory controllers. For example impurities in the reactor feed, hydrodynamic effects in the reactor are of this type of disturbances.

It is clear that the plant-wide control problem in hand has to address two types of control objectives. One is regulation; the other is optimization. Furthermore these control tasks have to be continuously met in a dynamic environment due to the existence of disturbances and changing product requirements. We have developed a hierarchical control structure which is based on the spatial decomposition of the plant into reactor and fractionation subsystems and temporal decomposition of the control tasks based on the characterization of disturbances, availability of measurements and frequency of control actions.

2.8.2 Hierarchical Plant Wide Control Structure

Complex systems are made up of large number of parts that interact in a non-simple way. In particular these interactions are often dynamic, nonlinear, stochastic, and delayed. In his pioneering article [36] in 1962 Nobel laureate economist Herbert Simon discussed the evolution of complex systems and concluded that complex systems are less affected by external disturbances if their structures are hierarchically organized and decomposable into stable parts. A hierarchy consists of a number of subsystems organized in a *functional* and *spatial* relationship to one another and, in their totality, possesses the character of an integral whole. A very important feature of hierarchical systems is that the hierarchical whole gives new properties to its individual parts, which, in turn, fulfills functions which did not exist previously. As an example chemical plants, such as the hydrocracking process, satisfy the definition of a hierarchically organized complex system. At the lowest level of the hierarchy we have the building blocks of a chemical plant which consist of basic unit operations such as tanks, heat exchangers, reactors and separators. At the next level of hierarchy these units are grouped together as subsystems to fulfill distinct operational objectives. Finally the subsystems come together through material and energy integration to meet the objectives of the whole chemical plant. The resulting system is a complex nonlinear dynamical system with many parts that interact in a nontrivial way. It is this hierarchical thinking and organization that guides both the way chemical plants are optimally designed and controlled by engineers today.

Complex systems, like the hydrocracker plant, have to fulfill certain operational objectives in an optimal way. The basic functions of feedback and optimization are implemented by hierarchical control architectures which are organized both in time and space. These hierarchical structures were originally articulated by Lefkowitz [37] and Mesarovic et al. [38]. Their first application to chemical processes in the context of synthesis of regulatory and optimizing control structures appeared in [35]. Around the same time, constraint control or in its most general form MPC emerged [39]. After a long period of theoretical advances, improvements in computer power and successful industrial applications using MPC, we are now witnessing a resurgence of hierarchical control concepts for real-time plant-wide optimization and operation. Attention is now focused on decentralized MPC, alternative coordination schemes and integration of RTO with MPC. For a review the reader is referred to [39, 40]. Next we present a hierarchical plant-wide control scheme which we have adopted for the hydrocracking process.

2.8.3 Cascaded MPC for Plant Wide Control

We propose a hierarchical control structure that consists of a cascade of MPC controllers operating in tandem with economic optimization and refinery planning as shown in Fig. 2.13. Starting from the top, each block in Fig. 2.13 is explained next.

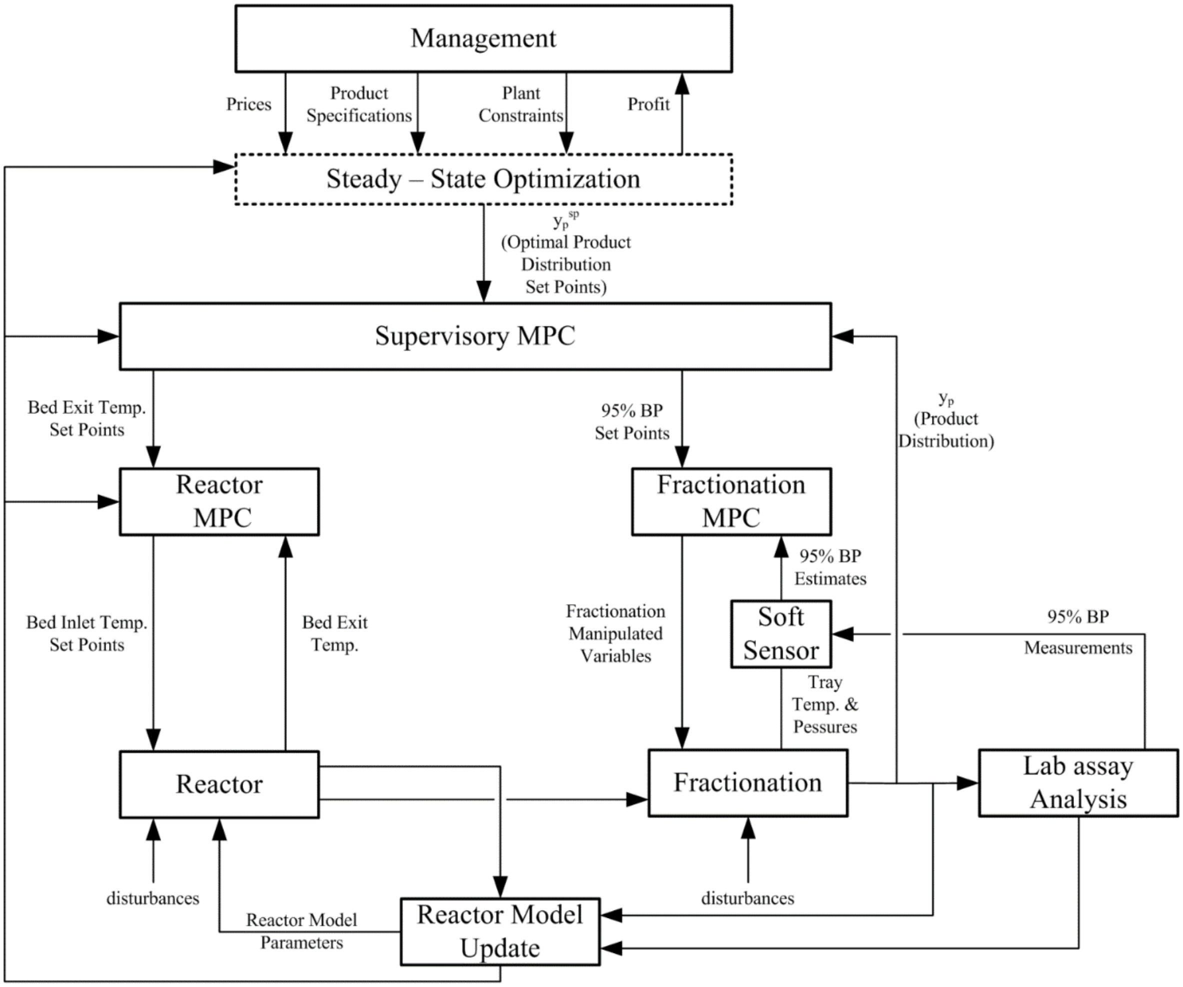

Figure 2.13: Plant-wide control structure for hydrocracking.

2.8.3.1 Management Layer

The highest level in the hierarchy is the management layer which considers the demand for the products by the market and by different units in the refinery. A refinery-wide linear programming is performed to compute the prices of feed, hydrogen and products. In addition product specifications and operating constraints for the hydrocracking plant are also defined.

2.8.3.2 Steady state optimization

The next layer below in the hierarchy is steady-state economic optimization. Steady-state optimization makes use of the steady-state predictions of the nonlinear hydrocracking model. Based on prices, product specifications and operating constraints set by the management, steady–state optimization maximizes profit by calculating the optimal product distribution (i.e. the relative amounts of light ends, light naphtha, heavy naphtha, diesel, kerosene, and bottoms), 95%BPs and the optimal reactor bed inlet and exit temperatures. Next the optimal economic operating conditions are converted to feedback implementation. This is accomplished through a cascade of coordinated MPCs.

2.8.3.3 Cascade of Coordinated MPCs

At the core of the proposed hierarchical control structure in Fig. 2.13 is a cascade of MPCs. Cascaded or nested MPCs appeared in the literature in different contexts to serve different purposes. For example in [41] cascaded MPCs are designed for different time scales to control a power system. In [42] a two-tiered approach is developed to coordinate distributed controllers for recycle processes that exhibit time scale separation. In [43] a two-stage QP-MPC cascade structure was proposed to update the RTO set-points to make them consistent (i.e. achievable) for the linear MPCs. This is done by an LP or QP that computes the feasible set-points closest to the steady-state optimal values given by RTO. MPC implements these feasible set points. In a similar context in [44] a price-driven coordination method is proposed to compute the targets for the decentralized MPCs. A cooperation based coordination of decentralized MPCs is developed in [45]. In cooperation based coordination, decentralized MPCs use the plant objective function as their local objectives and exchange local state and input information, thereby eliminating potential conflicts.

The main task of the proposed cascaded MPC structure is to coordinate a set of decentralized MPCs towards attaining the plant-wide economic steady-state optimum. We have applied a new coordination mechanism that is based on cascade control and this makes our problem formulation different than the available coordination mechanisms. The mechanism can be best understood if one focuses on its general hierarchical structure given in Fig. 2.14. Without any loss of generality a 2-subsystem plant is shown for simplicity. In Fig. 2.14 two sets of MPCs (locals and supervisory) operate in tandem under a cascade feedback configuration. In the classical cascade controller, the error in an (outer) primary control loop drives the set-point of an (inner) secondary control loop. Similarly here, the supervisory MPC functions like the (outer) controller of the primary control loop. Local decentralized model predictive controllers (MPC_1 and MPC_2) are the (inner) controllers of the secondary control loop. A set of plant-wide economic variables (denoted by y_p) are assigned as the controlled outputs to the supervisory MPC. The task of the supervisory MPC is to control these economic outputs at their set-points y_p^{sp} determined by steady-state economic optimization. It accomplishes this by specifying appropriate set-point trajectories y_1^{sp}, y_2^{sp} to the local MPCs. Thus, within the cascade loop, the supervisory MPC acts like a coordinator which guides the local MPCs towards the plant-wide economic steady-state optimum.

The control structure proposed for the hydrocracking plant in Fig. 2.13 is an application of the cascaded MPC structure shown in Fig. 2.14. The inner controllers are the decentralized reactor and fractionator MPC controllers. Reactor MPC controls the bed exit temperatures by manipulating the set-points of bed inlet temperatures. PID controllers regulate the bed inlet temperatures at the set-points sent by MPC by changing the hydrogen quench flow rates. These quench PID controllers are hidden inside the reactor block in Fig. 2.13. Fractionator MPC controls the 95%BPs by adjusting the set-points of the fractionation PID controllers shown in Fig. 2.11. Temperature measurements and 95%BP estimates through the soft sensor are available every sec.

The control cycles of decentralized MPC controllers are 3 minutes.

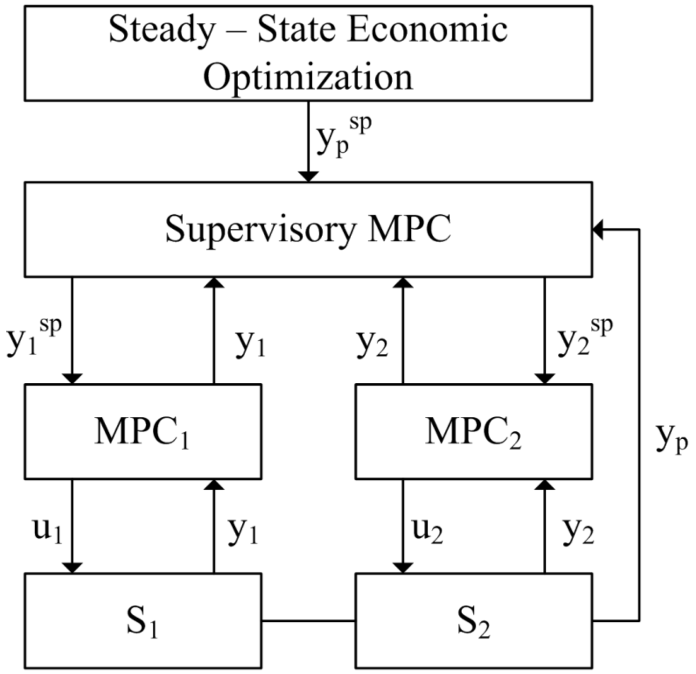

Figure 2.14: Cascaded MPC for plant-wide coordination.

The task of the Supervisory MPC is to control the plant-wide economic output variables. In our case the product distributions are chosen as the economic outputs. Supervisory MPC keeps these outputs at their optimal set-points by adjusting the set-points of the reactor exit temperatures and the 95% BPs as shown in Fig.2.13. In this fashion, it coordinates the local MPCs. The control cycle for the Supervisory MPC is 15 minutes which is much slower than the decentralized MPCs. There is a 2-hr delay between the reactor exit and the fractionator.

When there are slow, step-like disturbances, supervisory MPC tries to keep the plant-wide objective at its optimal steady-state value by making the necessary set-point changes in the local MPCs. Without this coordination, the plant-wide objective would drift from its economic optimum when persistent disturbances enter the subsystems. In addition, when steady-state optimization calls for a change in the product distribution, supervisory MPC provides new optimal set-point trajectories to the decentralized MPCs to perform the necessary transition between steady-states. Since the supervisory MPC responds to the effects of slower disturbances, it executes its coordinating control action much less frequently than the decentralized local MPCs.

2.9 Results

Proposed plant-wide control structure is tested against its ability to adapt to new economic conditions and to reject disturbances. In the hydrocracking process the optimal steady-state operating conditions change in response to different product specifications and fluctuations in raw material and product prices. Due to large throughputs, a slight modification in processing conditions yields significant profit increase on annual basis.

We consider a case where the plant is operating with the product distribution given in Table 2.5. Next the prices change and new optimal operating conditions are calculated by steady–state optimization. Corresponding new product distribution is given in Table 2.5 as well. For this case, it is seen that desired product distribution is lighter; therefore, higher cracking activity in the hydrocracker is needed.

Table 2.5: Product distribution before and after optimization.

	Initial	Final
Btm	0.079	0.059
Dsl	0.222	0.211
Krs	0.408	0.425
HN	0.170	0.180
LN	0.071	0.076
LE	0.042	0.049

2.9.1.1 MPC models

All the MPC designs were implemented using MATLAB's MPC Toolbox. Reactor MPC uses a step response model obtained from the dynamic reactor model. All the reactor constraints (2.41-2.43) are included in the MPC optimization. The fractionator MPC uses the step response model between four 95% BPs and eight manipulated variables (fractionator top pressure, fractionator top temperature, kerosene withdrawal rate, diesel withdrawal rate, middle reflux, splitter top pressure, splitter middle tray temperature and splitter reflux set-points). This model was constructed from step tests implemented on the actual plant. Corresponding transfer functions are given in Table 2.6

Table 2.6: Transfer functions that are used to design the Fractionation MPC

		95% BPs (CV)			
		$\text{Dsl}_{95\%}$	$\text{Krs}_{95\%}$	$\text{HN}_{95\%}$	$\text{LN}_{95\%}$
MVs	Fractionator Top Pressure	(-14.4,0.25,0)	(-1.8,0.3,0.13)		
	Fractionator Top Temperature		(1.2,0.36,0.0116)	(0.9,0.25,0.0116)	
	Kerosene Withdrawal	(1.5,0.1,0.13)	(2.3,0.45,0.016)		
	Diesel Withdrawal	(1.45,0.8,0)	(1.4,0.14,0)		
	Middle Reflux	(0.5,0.36,0.05)			
	Splitter Top Pressure				(-17.3,0.202,0)
	Splitter Tray Temperature				(2.2,0.65,0.09)
	Splitter Reflux				(-0.2,0.12,0.03)

The parameters of the individual transfer functions appear in parentheses as *"gain, time constant, time delay"*, respectively. Values are slightly modified from plant data for proprietary reasons. When there is negligible interaction between MV and CV, the corresponding cell is left blank in the table.

Supervisory MPC's manipulated inputs are (four) reactor exit temperature set-points and (four) 95%BP set-points. Its controlled outputs are (six) product distributions. As shown in Fig. 2.14, the dynamic relationships between these variables are governed by the closed-loop action of decentralized MPC controllers. Therefore we have constructed the transfer functions between these inputs and outputs (48 of them) by simulating the plant model under closed-loop conditions by including the local MPCs. Specifically, step changes were made in the reactor exit temperature set-points and 95%BP set-points of the local MPCs (see Fig. 2.14), and the response of the product distribution was recorded. Local MPCs have been designed so that the closed-loop responses of 95% BPs are smooth first order responses. In addition, since the product distributions are directly correlated with 95% BPs through temperature cut-points (see Fig. 2.5), they also exhibit smooth first order responses. Therefore, we were able to approximate the transfer functions between the product distributions and 95% BP set-points and reactor temperature set-points by simple first order systems. Corresponding transfer functions are given in Table 2.7.

Table 2.7: Transfer functions that are used to design the Supervisory MPC

		Product weight fractions **(CV)**					
		Btm	Dsl	HN	Krs	LE	LN
MVs	$B1_{exit}$	(-0.0016118,0.65,3)	(-0.001798,0.65,3)	(0.0012,0.65,3)	(0.0006,0.65,3)	(0.0006,0.65,3)	(0.0007,0.65,3)
	$B2_{exit}$	(-0.0023,0.65,2.75)	(-0.0027,0.65,2.75)	(0.0018,0.65,2.75)	(0.0009,0.65,2.75)	(0.0010,0.65,2.75)	(0.0011,0.65,2.75)
	$B3_{exit}$	(-0.0023,0.65,2.5)	(-0.0026,0.65,2.5)	(0.0018,0.65,2.5)	(0.0010,0.65,2.5)	(0.0010,0.65,2.5)	(0.0011,0.65,2.5)
	$B4_{exit}$	(-0.0025,0.65,2.25)	(-0.0028,0.65,2.25)	(0.0019,0.65,2.25)	(0.0010,0.65,2.25)	(0.0010,0.65,2.25)	(0.0012,0.65,2.25)
	$Dsl_{95\%}$	(-0.0019,0.35,0)	(0.0019,0.35,0)				
	$HN_{95\%}$			(0.0011,0.30,0)	(-0.0011,0.30,0)		
	$Krs_{95\%}$		(-0.0029,0.45,0)		(0.0029,0.45,0)		
	$LN_{95\%}$			(-0.0043,0.42,0)			(0.0043,0.42,0)

The parameters of the individual transfer functions appear in parentheses as *"gain, time constant, time delay"*, respectively. Values are slightly modified from plant data for proprietary reasons. When there is negligible interaction between MV and CV, the corresponding cell is left blank in the table.

Next these transfer functions were used by the supervisory MPC to control the product distributions at their economically optimum set-points. All the constraints including those for the reactor (2.41-2.43) and those for the fractionator (2.44) are addressed in the supervisory MPC computation. Therefore, the set-point changes demanded by the supervisory MPC controller are feasible for the decentralized MPCs.

2.9.1.2 Plant Model

The plant model used in the closed-loop simulations consists of the first principle nonlinear reactor model and the empirical fractionator model. Both models were validated against plant data. The empirical fractionation model includes both the static correlations that describe the relationships between 95%BPs, TCPs, weight fractions and the transfer functions given in Tables 2.6 and 2.7 which represent the dynamics. We have chosen to use this model in place of a more detailed rigorous model because our closed-loop simulations using the empirical model have matched the real closed-loop plant data closely. This is due to the fact that the operating window of the fractionator is narrow and the local fractionation MPC can be tuned so that the closed-loop model responses are close to those of the plant.

For the scenario listed in Table 2.5, the closed-loop response of product distribution is presented in Fig. 2.15. Optimal product distribution is reached in about 5 hours. The set points supplied by the supervisory MPC to the reactor MPC and the reactor's response are shown in Fig. 2.16. Note that increase of bed temperatures is in line with the demanded transition to a lighter product distribution.

Supervisory MPC also affects the fractionator MPC by changing the 95% BP set-points as shown in Fig. 2.17. The impact of fractionator MPC on the products is observed instantly since 95%BPs are directly correlated with the product weight fractions. However the influence of reactor temperature is felt after 2 – 3 hours of delay. Therefore the initial impact of fractionator MPC results in a pseudo-steady state in products around t=1-2 hours as seen in Fig. 2.15. This effect is followed by the delayed effect of changes made in the reactor temperature which is seen in the transient response from the initial pseudo-steady state to the final product. For a slight shift in product distribution, changes only in the fractionator (i.e. 95%BP set-points) are adequate; but significant changes in product distribution require manipulations in the reactor temperature set-points as well. As a result, settling to the new steady state takes much longer time than the time constant of fractionator alone. Supervisory MPC takes into account the interactions among the reactor and fractionator and the long time delay between them and coordinates the operation of the decentralized MPCs by making the right set-point changes.

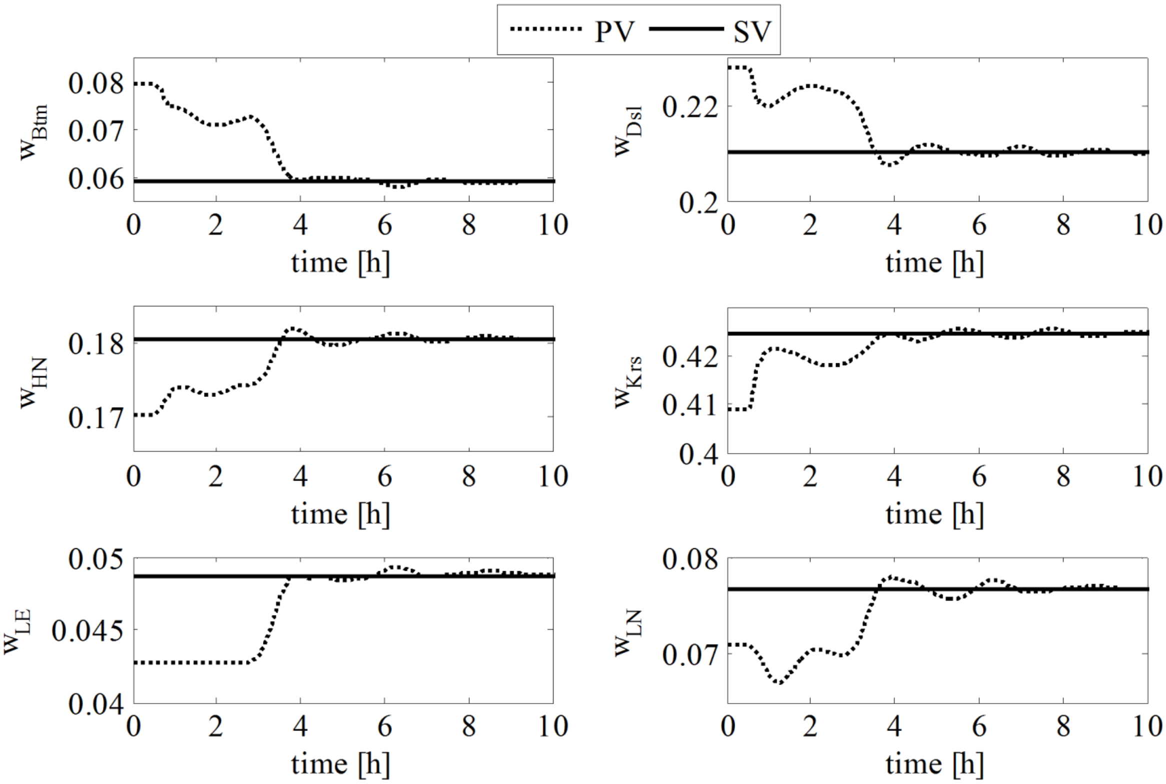

Figure 2.15: Response of product weight fractions.

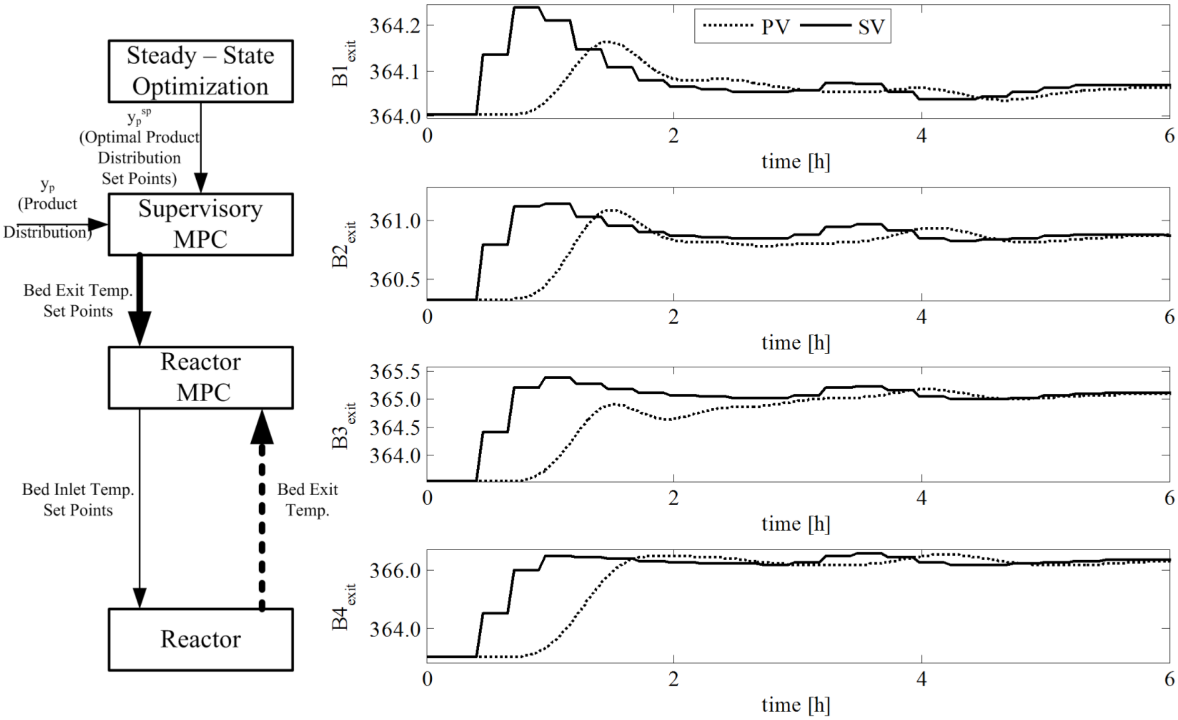

Figure 2.16: Dynamic behavior of bed exit temperatures.

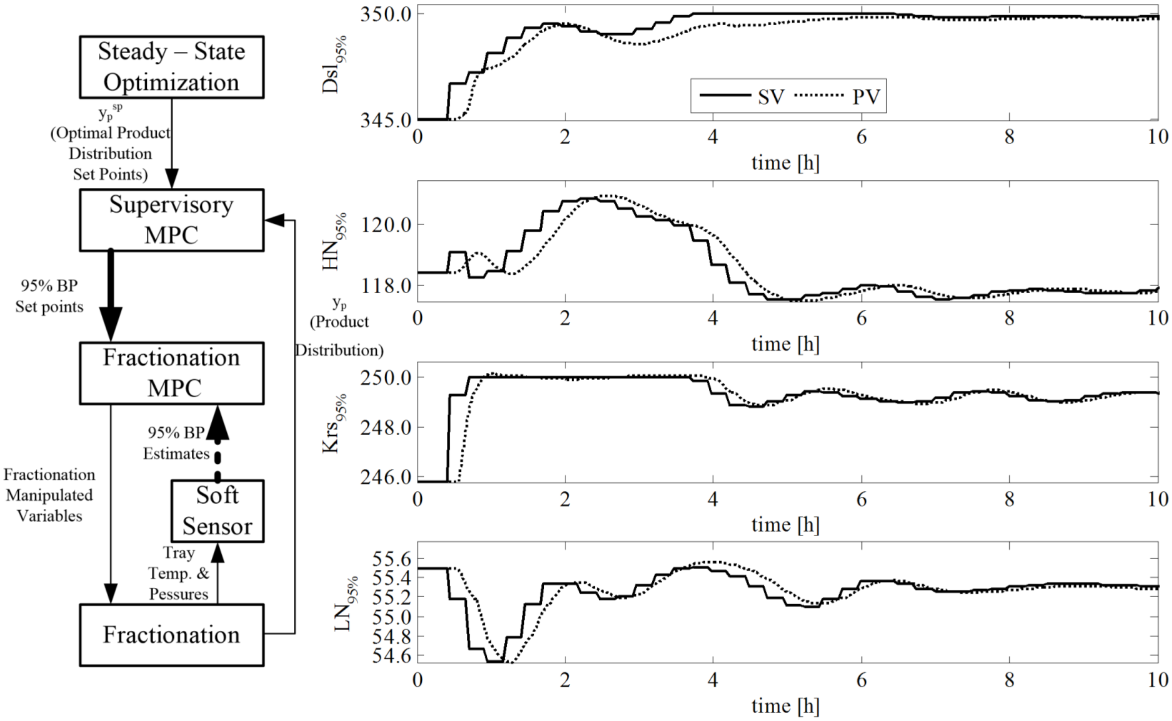

Figure 2.17: Dynamic behavior of 95% BPs.

The 95% BPs in Fig. 2.17 are realized by adjusting 8 manipulated variables in the fractionation subplant. The behaviors of fractionation manipulated variables are shown in Fig. 2.18. Those are in deviations from nominal values.

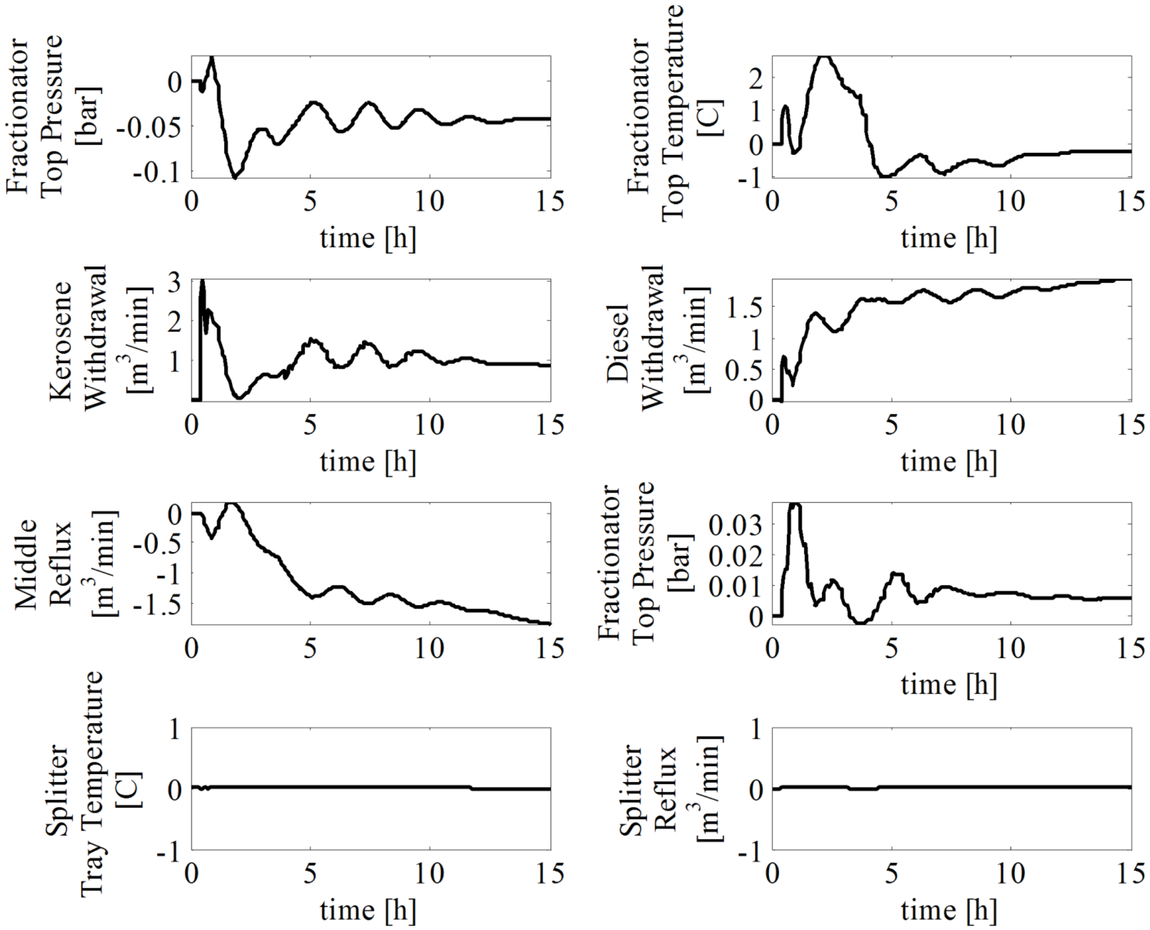

Figure 2.18: Dynamic behavior of manipulated variables of fractionation MPC for set point tracking.

Measurement of disturbances and modeling their effects is not easy in such a complex system. For that reason, disturbances are considered as output disturbances and they are modeled as integrated white noise processes. This modeling represents randomly varying step-like disturbances which are common in chemical processes. In addition output disturbance models are used in MPC to prevent steady-state offset. In this study, disturbances are added on product weight fractions and bed exit temperatures, which are shown in Fig.

2.19. The persistent effects of these disturbances on the products are successfully rejected with an acceptable variance as shown in Fig. 2.20.

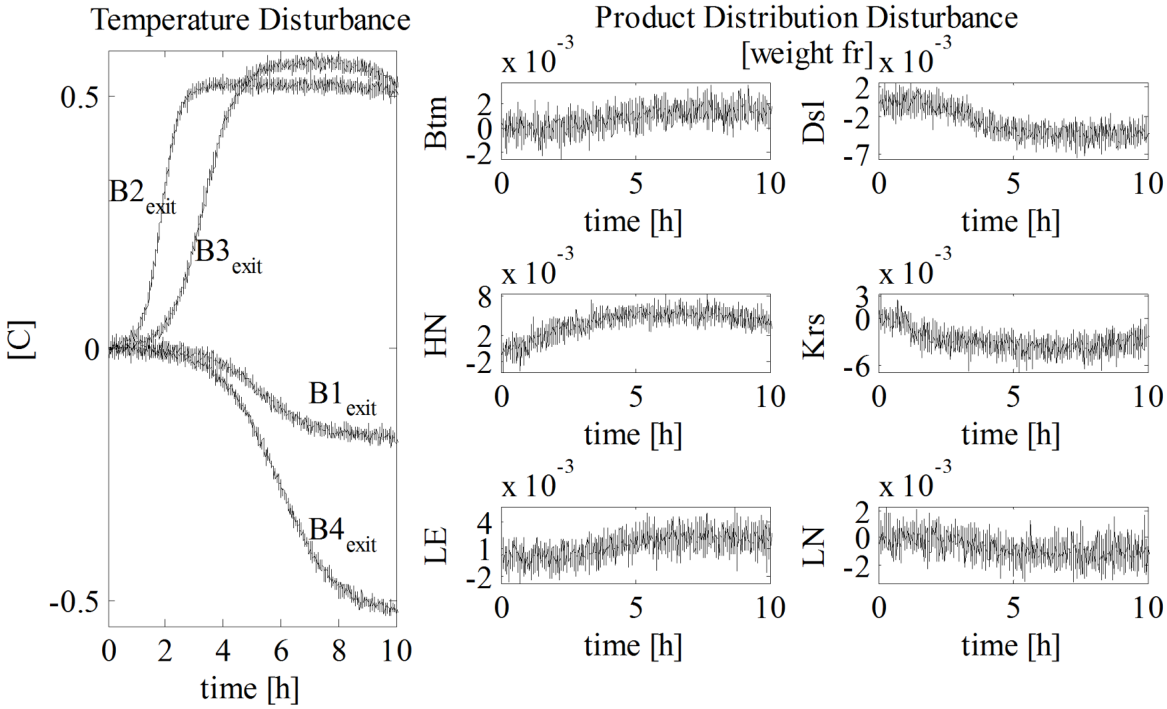

Figure 2.19: Output disturbances.

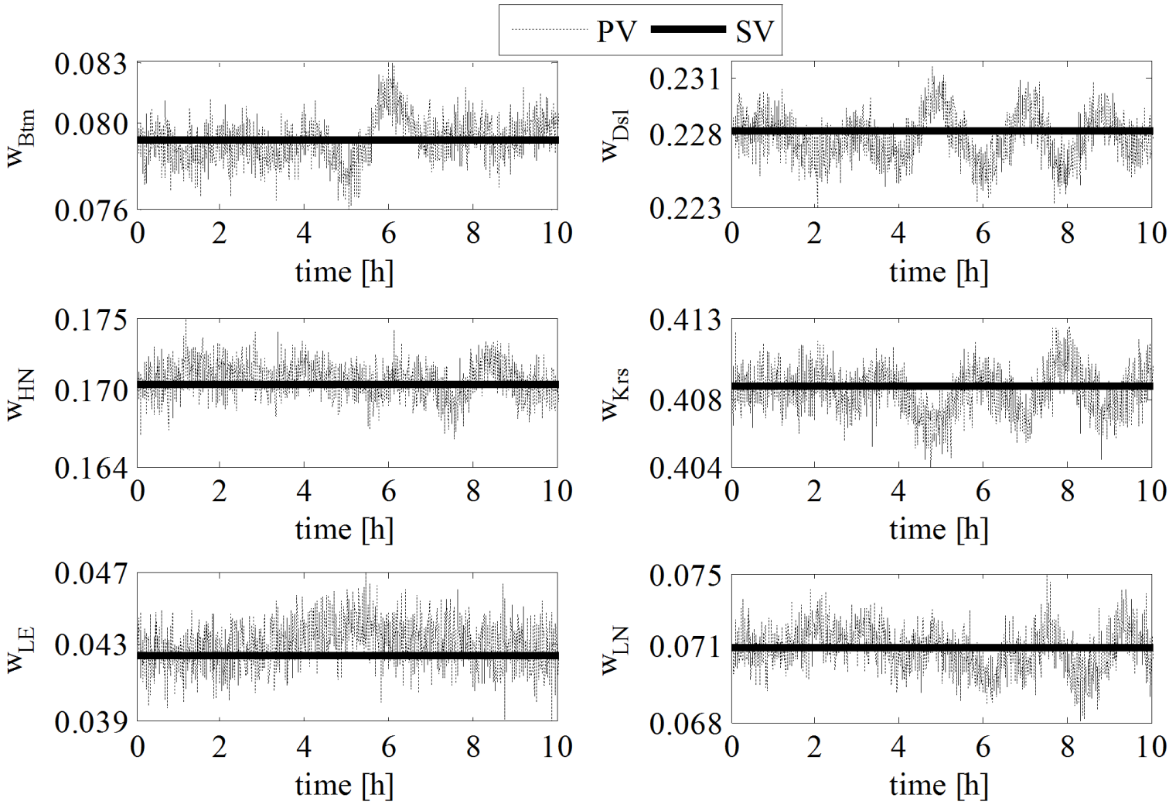

Figure 2.20: Controlled responses of product weight fractions to disturbances.

In order to reject the disturbances in Fig. 2.19, supervisory MPC changes the reactor and fractionator operating conditions as shown in Fig. 2.21 and Fig. 2.22 respectively.

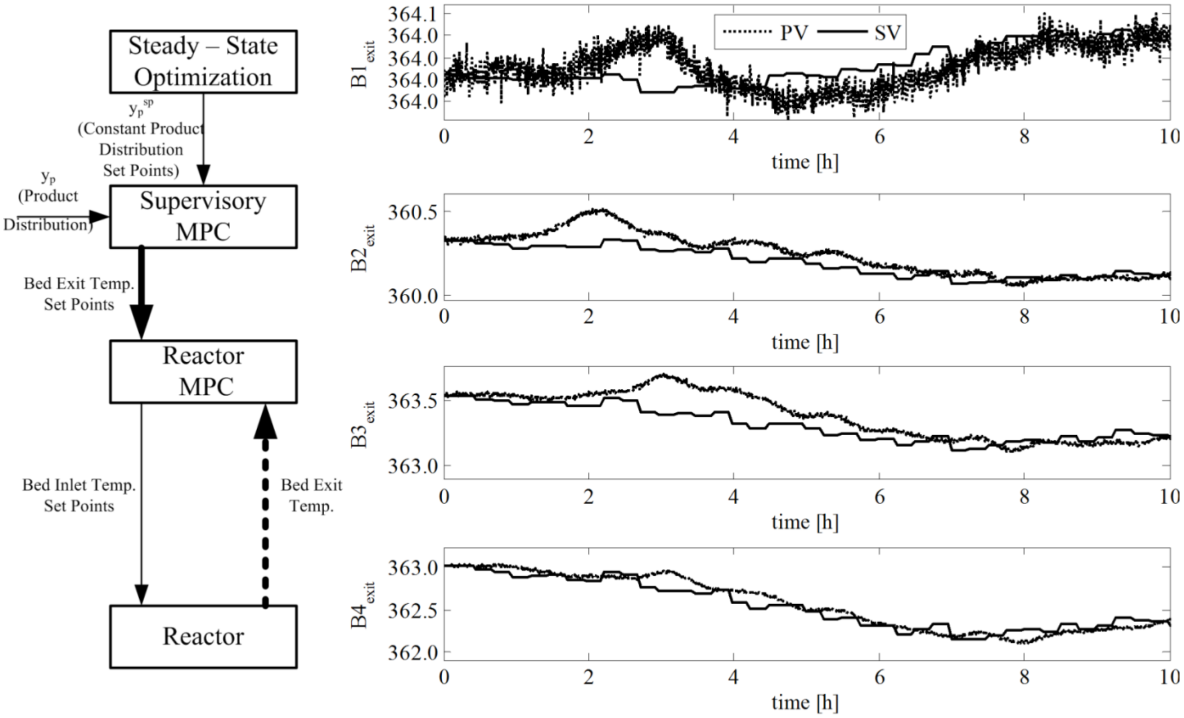

Figure 2.21: Dynamic behavior of bed exit temperatures for disturbance rejection.

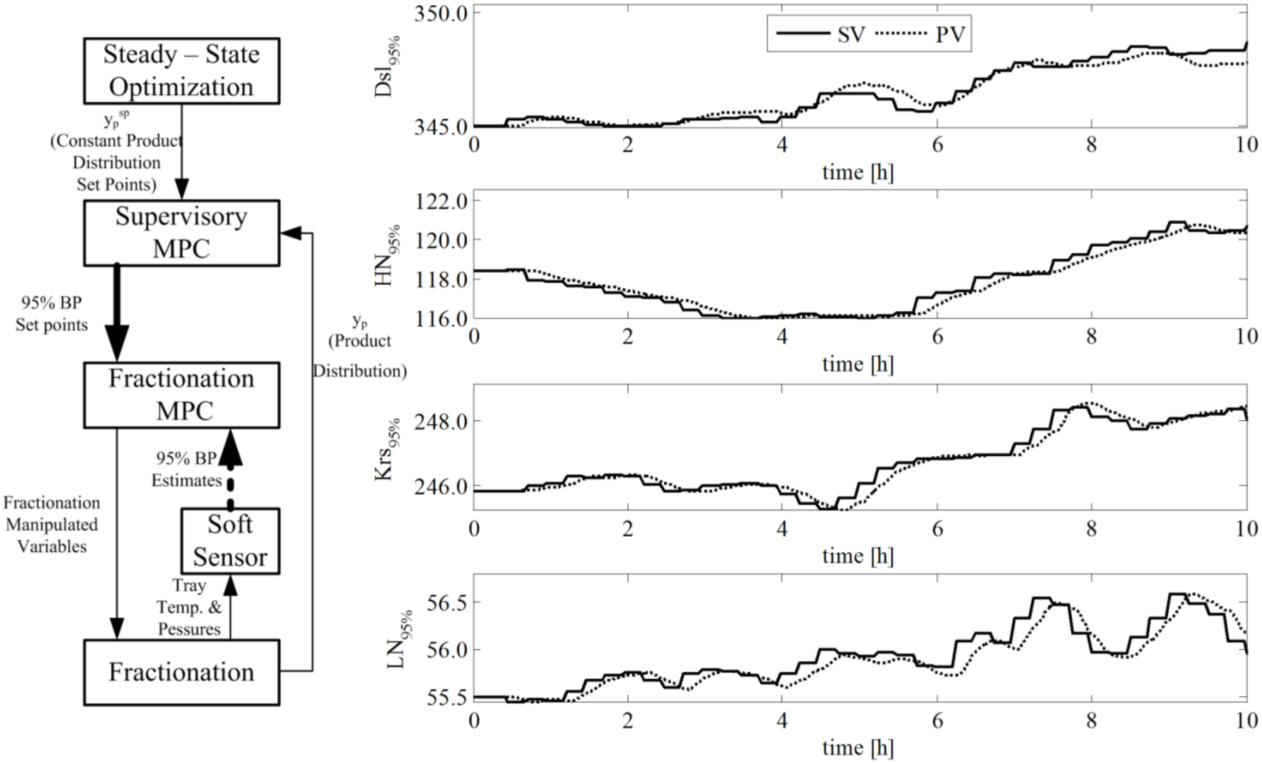

Figure 2.22: Dynamic behavior of 95% BPs for disturbance rejection.

Required manipulated variable changes to reject disturbances are shown in Fig. 2.23.

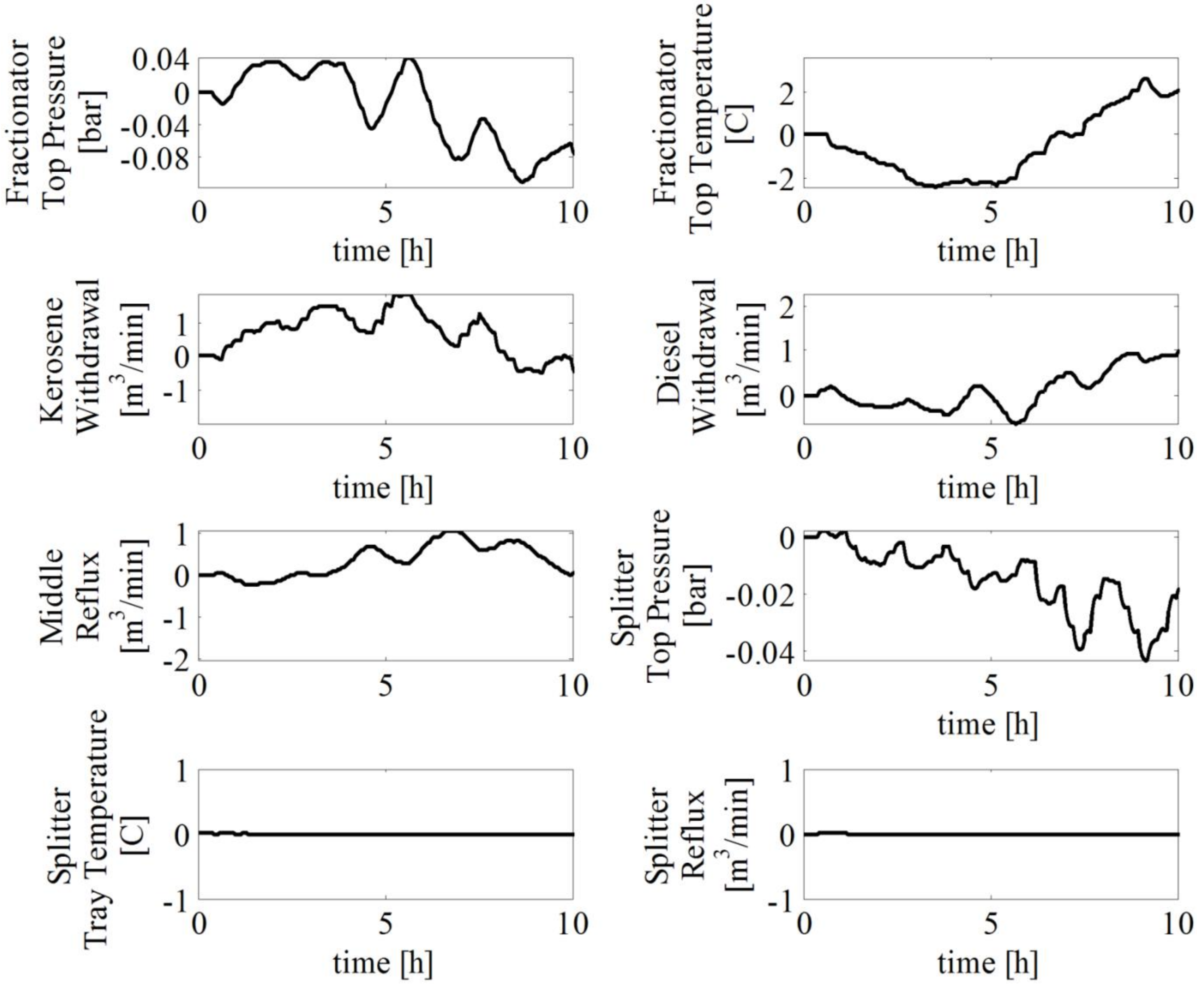

Figure 2.23: Dynamic behavior of manipulated variables of fractionation MPC for disturbance rejection.

2.10 Conclusions

Using the method of continuous lumping, we have developed a reactor model for an industrial hydrocracking unit. Unlike previous continuous lumping models in the literature, the model is non-isothermal and includes dynamic effects. Therefore it can predict the reactor bed temperatures and product yields under both steady-state and transient conditions. Using parameter estimation the model was validated against plant measurements. Model predictions of reactor bed temperatures, hydrogen consumption and product yields were found to be in excellent agreement with the plant data. The model is useful for real-time optimization purposes by which the model parameters can be retuned on-line as desired; and economically optimal operating conditions can be updated and implemented by advanced control systems.

For real-time optimization and control purposes, a hierarchical plant-wide control structure is systematically constructed for a complex refinery process such as hydrocracking. Economic optimization and regulation tasks of this hierarchical control structure require reliable steady-state and dynamic models. It is an empirical model developed from plant data and it correlates the 95% boiling points used in the fractionator with the weight fractions of the product in the reactor. As such it is used to predict the effect of reactor operating conditions on the distillation product distribution. In addition several important distillation product specifications are successfully correlated and validated with the 95% boiling points. These models are next used in the design of the local decentralized MPC controllers for the reactor and fractionator.

A novel feature of the plant-wide hierarchical control system is that cascade control is used for coordination of decentralized MPC controllers. In this cascade, a supervisory MPC coordinates the actions of the decentralized reactor and fractionator MPC controllers by adjusting their set-points and moving the whole plant towards the optimum operating conditions. While decentralized MPCs reject the local disturbances and keep their units (i.e. reactor and fractionator) within limits, the supervisory MPC coordinates the local MPCs to achieve a smooth and fast transition between different steady-states. The proposed methodology and cascaded MPC structure can find applications in many other complex plants.

Simulations show that the proposed control system is able to make the necessary transition in product distributions successfully by operating the reactor and fractionator at the optimal conditions determined by economic optimization. Through this study, the potential benefits of implementing real-time optimization for the hydrocracking plant have been found to be significant.

Chapter 3

DISCRETE LUMPING AND APPLICATION TO FCC

3.1 Introduction

Fluid catalytic cracking (FCC) is one of the most important refinery processes. It is used for cracking high molecular weight hydrocarbon feedstocks to smaller molecules which boil at relatively lower temperatures. In the refinery under study here, heavy vacuum gas oil (HVGO) feed is converted to off-gas, liquefied petroleum gas (LPG), whole crack naphtha (WCN), light cycle oil (LCO) and clarified oil (CLO). LPG and WCN are usually the primary products. Approximately, 45% of naphtha in the world is produced by FCC [46].

The existing FCC plant in the refinery consists of a reaction unit which is followed by the fractionation unit that separates the reactor effluent into final products. A simplified process flow sheet is shown in Fig. 3.1. Pressure and temperature transmitters are represented by PT and TT, respectively. The block that is marked with “GC” represents the gas analyzer. The reaction unit is composed of the riser and the regenerator. HVGO is fed to the bottom of the riser after it is dispersed through a nozzle system. After dispersion, the feed vaporizes upon contact with the hot catalyst coming from the regenerator. Dispersion of the feed provides more heat transfer which in turn increases the efficiency of feed vaporization. Some amount of lift steam is also added to provide drag force to catalyst particles. Steam and the vaporized feed lift the catalyst particles upward through the riser. In the riser, vaporized hydrocarbons crack to smaller molecules on the catalyst surface. In addition to the cracking reactions, some amount of coke is deposited on the catalyst surface which reduces the catalyst's activity. At the riser exit, deactivated catalyst particles are separated and transferred back to the regenerator whereas the vapor hydrocarbons are sent to the fractionation unit where they are separated into the end products. In the regenerator, the coke on the catalyst is burned with air and fresh hot catalyst is transferred back to the riser inlet. The gaseous products of combustion reactions are further processed in the CO burner.

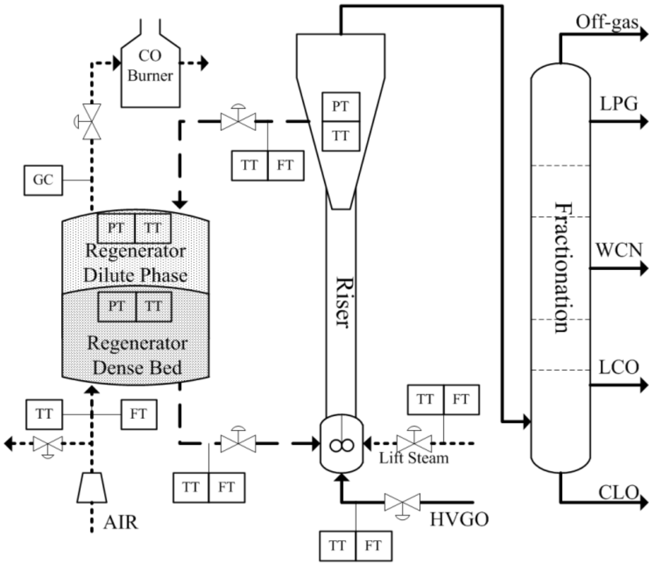

Figure 3.1: Simplified process flow diagram of FCC plant in the refinery.

Our modeling objective here is to derive a practical nonlinear model which captures the dominant steady-state and dynamic features of the plant. To this end, the riser and the regenerator units are modeled using first principles and their parameters are estimated from plant data. In order to predict the end products of the fractionation unit from the reactor effluent, an empirical model is developed by making use of temperature cut points (*TCP*s). This eliminates the need for any rigorous fractionation unit modeling to calculate the product distribution. Details of these models are presented next.

3.2 Modeling of the Riser

In the riser, hydrocarbon compounds are converted to smaller molecules which boil at lower temperatures. There is a high number of chemical species in the reaction medium. Complexity of detailed models has motivated the development of simpler lumped models. In discrete lumping approach [47], the mixture is assumed to be composed of pure pseudo-components (*PC*s) that are characterized by an intrinsic property. In our case, each *PC* is defined by its average normal boiling point (*NBP*). In the literature, most studies prefer to use small number of *PC*s to facilitate modeling and to reduce the number of unknown parameters. In early studies [9, 11, 48] the reaction medium is represented by 3 lumps (feed, gasoline and light gases, coke). Limited flexibility of these models has motivated the introduction of additional lumps. In some studies, coke and light gases are considered as separate lumps [49-51]. Later studies also include diesel as another lump [52-54]. Vargas et al. used a 6- lump model and estimated parameters from refinery data [55]. In some detailed studies 10- lump models are used [56-58].

It is customary to characterize the composition of petroleum fractions by a boiling point curve. Such curves are obtained from an industry- standard ASTM laboratory test in which distilled volume fractions of the sample are recorded as a function of temperature. Next mass fractions can be computed (e.g. using the oil manager of HYSYS) and plotted versus temperature. In our case, the boiling point curves of *HVGO*, *WCN*, *LCO* and *CLO* are measured in the refinery. *LPG* and off-gas composition is analyzed using gas chromatography and this data can be used to obtain the boiling point curve of these products as well. The boiling point curves of 5 individual products and the feed *HVGO* are shown in Fig. 3.2. It is not possible to sample and perform a similar distillation assay on the riser output before fractionation due to safety and other physical restrictions. Because of lack of this data, we blend the individual boiling point curves of the 5 products in HYSYS to obtain the boiling point curve of the riser effluent. The riser effluent boiling point curve reconstructed in this fashion is shown in Fig. 3.2 as well.

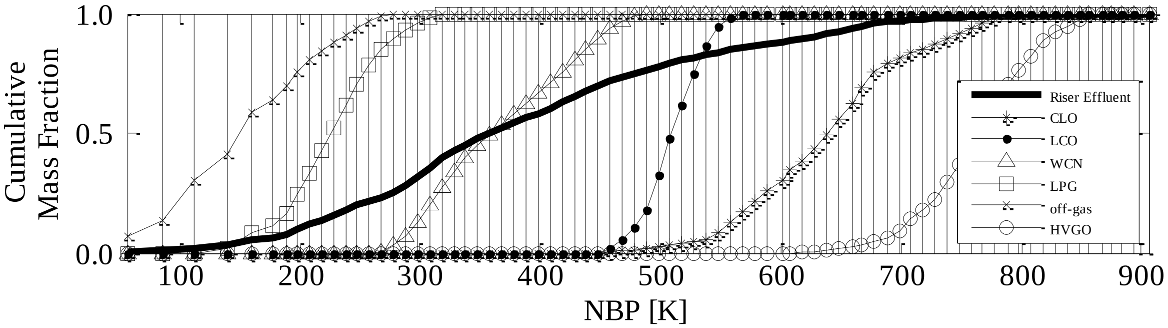

Figure 3.2: Boiling point curves of petroleum fractions. Vertical lines represent the *NBP* of the corresponding *PC*.

The boiling range in Fig. 3.2 is quite large; therefore, few *PC*s fail to characterize such mixtures. Modeling the reaction medium with narrow fractions enables better prediction of product properties in general. Therefore, for NBP between 200 and 900 K, the riser effluent is divided into *PC*s which have a small boiling range of 10K. Since there is very little material in very light products, the related *PC*s up to NBP=200K were assigned higher boiling point range in order to reduce their number for computational purposes.

The riser includes the mixing and the reaction zones which are modeled next.

3.2.1 The Mixing Zone

The volume in which the liquid feed is combined with the hot catalyst at the riser inlet is called the mixing zone. It is widely accepted in the literature that vaporization occurs in a small fraction of the riser [59, 60]. Therefore, the mixing zone is taken as a small volume and modeled separately from the reaction zone. Crucial inputs to the mixing zone are shown in Fig. 3.3. The amount of lift steam is negligible compared to the mass of catalyst and feed [61].

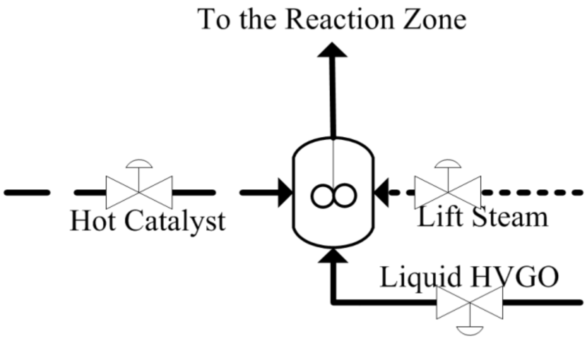

Figure 3.3: The mixing zone

The catalyst to oil mass ratio is usually high and the catalyst temperature is much greater than the feed vaporization temperature. In addition, the feed is dispersed in the mixing zone to provide turbulence for efficient vaporization. Due to high heat transfer rate between the catalyst and the hydrocarbons, the catalyst and the vaporized hydrocarbons can be assumed to have the same temperature when they leave the mixing zone. There is no reaction in the mixing zone since catalyst is active only when the hydrocarbons are in gaseous phase [62].

Under these conditions, steady-state energy balance for the mixing zone results in:

$$\begin{aligned} &\int_{T_{Regen}}^{T_{MixZone}} \dot{M}_{cat} \cdot c_{p,cat} dT = \\ &\sum_{i=1}^{N} \int_{T_{HVGO}}^{T_{B,i}} \dot{M}_i \, c_{p,liquid,i} dT + \sum_{i=1}^{N} \Delta H_{vap,i} + \sum_{i=1}^{N} \int_{T_{B,i}}^{T_{MixZone}} \dot{M}_i \, c_{p,gas,i} dT + \int_{T_{steam}}^{T_{MixZone}} \dot{M}_{steam} \, c_{p,steam} dT \end{aligned} \tag{3.1}$$

In Eq. 3.1, the left hand side is the heat released by catalyst particles. The first term in the right hand side is the energy that is needed to increase the temperature of the liquid hydrocarbons to their boiling points. The second term is vaporization of hydrocarbons, and the third term is superheating of those hydrocarbons to the mixing zone temperature. The last term is the energy added to the lift steam. An expression similar to Eq. 3.1 was already used in the literature [63, 64]. Heat capacities for the pseudo-components are estimated from [65]. Heats of vaporization are obtained from HYSYS and there are some correlations in the literature which provide similar predictions as well [66, 67].

After $T_{MixZone}$ is determined from Eq. 3.1, the velocity of the gas (v_g) leaving the mixing zone can be calculated from the ideal gas law as a result of high temperature and low pressure operating conditions at the reaction zone inlet:

$$v_g = \frac{\dot{M}_{HVGO}\, R \cdot T_{MixZone}}{MW \cdot P \cdot A_{riser}} \tag{3.2}$$

3.2.2 Reaction Zone

The reaction zone starts right after the mixing zone. Vaporized hydrocarbons and catalyst particles travel along the reaction zone where cracking reactions occur. At the riser exit, deactivated catalyst particles are sent to the regenerator and vapor hydrocarbons are sent to the fractionation unit where they are separated.

The riser is modeled as an adiabatic, one-dimensional, two-phase moving bed reactor. Hydrodynamics of the riser is not well understood [68] and including the radial direction would increase the modeling uncertainty. In addition, radial distribution has not been observed to be significant [55]. The cracking reactions are assumed to be first order and irreversible. Riser dynamics is very fast relative to the much slower regenerator which dominates the overall dynamic behavior [57, 61]. Therefore, the riser can be assumed to be at pseudo-steady state and its modeling equations are derived only for steady-state conditions. The results in [55] demonstrate that the catalyst and the gas obtain the same temperature very fast. Thus, there is no heat transfer resistance between the vapor and catalyst phases.

3.2.2.1 Hydrodynamics

The pressure drop is mainly governed by gravitational forces and acceleration of particles and is calculated using [69]:

$$\frac{\partial P}{\partial z} = -\left((1-\varepsilon)\rho_{cat} + \varepsilon\rho_g\right)g - \frac{\partial}{\partial z}\left((1-\varepsilon)\rho_{cat}v_{cat}^2 + \varepsilon\rho_g v_g^2\right) \tag{3.3}$$

where the void fraction ε is given by:

$$(1-\varepsilon) = \frac{\dot{M}_{cat}}{v_{cat}\rho_{cat}A_{riser}} \tag{3.4}$$

The catalyst velocity is calculated from [69, 70]:

$$\frac{\partial v_{cat}}{\partial z} = C_D \frac{3}{4}\frac{\rho_g \cdot (v_g - v_{cat})^2}{d_{cat}\rho_{cat}v_{cat}} + \frac{(\rho_g - \rho_{cat})g}{\rho_{cat}v_{cat}} \tag{3.5}$$

C_D is the drag coefficient; d_{cat} is the average diameter of the catalyst particles (m); ρ_{cat} and ρ_g are catalyst and gas phase densities, respectively. In our case, the catalyst particles are small and the catalyst velocity is close to the gas velocity as shown in Fig. 3.4. Assuming the same velocity for gas and catalyst reduces the computational load and does not result in significant changes in our results.

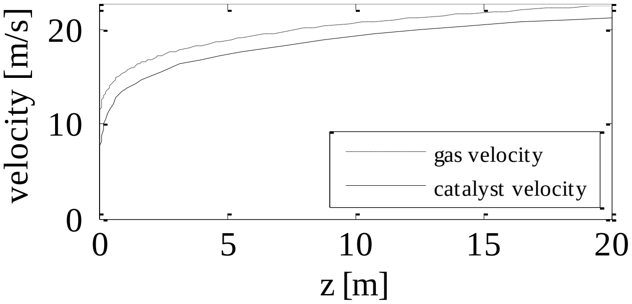

Figure 3.4: The catalyst and the gas velocity

3.2.2.2 The Kinetic Model

Cracking rate constant depends on many parameters including feed and catalyst properties. Bollas et al. [71] defined a feed index to relate paraffinic, olefinic, and aromatic content of the feed to rate constants based on empirical correlations. Ginzel [72] investigated the influence of feed quality on cracking performance. In summary, limited knowledge of chemical composition for complex feeds provides only some qualitative understanding of kinetics. In our case, we have defined the pre-exponential factor A_i and the activation energy E_i as a function of boiling point only. In this fashion unnecessary details and feed analysis are avoided while using readily available boiling point data which is most representative of oil fractions [73]. Therefore, the pre-exponential factor and activation energy of i^{th} pseudo component are parameterized by its boiling point, NBP_i:

$$A_i = \beta \cdot NBP_i^{\mu} \tag{3.6}$$

$$E_{A,i} = E_1 - E_2 \cdot NBP_i \tag{3.7}$$

The rate constant for each PC is calculated from:

$$k_i = A_i e^{-E_{A,i}/RT} \tag{3.8}$$

Parameters E_1, E_2, β and μ are estimated from plant data. Eq. 3.6 is in the form of a power law [74] since higher boiling materials have higher cracking rate constants [75]. Eq. 3.7 is proposed based on experimental evidence that activation energy is higher for low boiling materials in general [76-78]. The nature of the activation energy also explains why the light materials react more slowly and the average activation energy increases when lighter molecules are formed in the cracking reactions [77].

When j^{th} *PC* cracks, it forms the lighter *PC*s. The yield function *p(i,j)* determines the amount of i^{th} *PC* formed from cracking of j^{th} *PC*. Construction of the yield function is challenging since the reactions are highly dependent on catalyst properties, feed content, operating conditions and many other unknown factors [79]. In addition, available refinery data is limited since measurements can be taken at the riser exit only, which limits the analysis of the intermediate products. In [47], the kinetic model suggests maximum probability for any *PC* to produce two other *PC*s that have similar molecular weight. Hernandez et al. used beta distribution function [80] for similar purposes. In our case, we make use of literature results on the riser behavior to construct the yield function. For example, Gilbert et al. [81] observed that the amount of light materials is positively correlated with the contact time. In addition, catalyst type influences the results significantly, which means the yield function might be catalyst dependent. The results in [70, 80, 82, 83] demonstrate that there is a temperature and composition profile along the riser. Thus, starting from the riser inlet, the yields of cracking reactions to intermediate products should be in significant amounts, and those intermediate products should be next consumed by secondary reactions. In order to determine the distribution of primary products, we focused on the experiments that provide minimum contact time and conversion. The product distributions of paraffinic and olefinic petroleum feedstocks are presented in [75] with a low contact time.

The product distribution of a specific petroleum cut is also presented in [84]. Based on those studies, the following yield function is constructed to calculate the products distribution of a specific *PC*:

$$p(i,j) = \frac{1}{P_j^T}\sqrt{\frac{\lambda_p \cdot NBP_j}{2\pi \cdot NBP_i^3}}\, e^{\frac{-\lambda_p \cdot NBP_j}{2\left(\mu_p \cdot NBP_j\right)^2 NBP_i}\left(NBP_i - \mu_p \cdot NBP_j\right)^2} \tag{3.9}$$

where λ_p and μ_p are adjustable parameters. P_j^T is the normalization factor so that $\sum_{i=1}^{j} p(i,j) = 1$:

$$P_j^T = \sum_{i=1}^{j-1}\sqrt{\frac{\lambda_p \cdot NBP_j}{2\pi \cdot NBP_i^3}}\, e^{\frac{-\lambda_p \cdot NBP_j}{2\left(\mu_p \cdot NBP_j\right)^2 NBP_i}\left(NBP_i - \mu_p \cdot NBP_j\right)^2} \tag{3.10}$$

p(i,j) for three *PC*s that have different *NBP*s are presented in Fig. 3.5a.

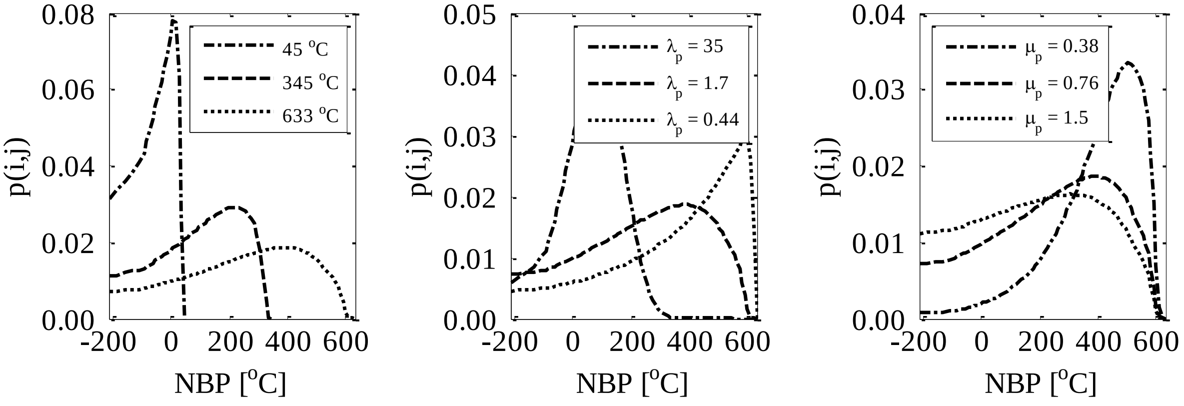

(a) (b) (c)

Figure 3.5: Product distributions of specific pseudo-components

Fig. 3.5a. shows that higher boiling *PC*s have wider product distributions whereas light products can produce less type of species. The yield function expressed by Eq. 3.9 is flexible as it generates a large class of different product distributions by tuning its parameters. For example, different possible product distributions of the heaviest *PC* are presented in Fig. 3.5b and Fig. 3.5c when those parameters are changed. The yield function parameters are updated from plant data and thus it is assumed that resulting yield function will be a good approximation of the true distribution.

In the riser, along with cracking reactions, some portion of hydrocarbons is deposited on the solid catalyst due to coking. Coke deposition causes significant deactivation of catalyst even though the mass of the coke is significantly less than that of the catalyst and feed. The amount of coke should be predicted accurately to calculate deactivation and the reaction rates in the regenerator. When few lumps are used to characterize the reaction medium, usually coke is considered a separate lump (i.e. [49-51]). The coking tendency is affected by feedstock, operating conditions, catalyst type, and reactor design [85]. It is known that most of the coke formation occurs early in the riser [86, 87]. It is found in [87] that catalyst to oil ratio is positively correlated with coke formation. In addition, heavy and aromatic hydrocarbons increase coking [71, 88]. In [71], the Conradson carbon of the feed is found to be an indicator of coking tendency. Heavy hydrocarbons form most of the coke since they are richer in carbon [61]. It is clear that coke is a product of cracking reactions and it should be included in the kinetic model. We have introduced a coking tendency parameter (φ) in our model. For each cracking reaction, φ fraction of the reacting material is converted to coke.

3.2.2.3 Mass Balance

The following steady-state mass balance holds for a specific pseudo-component (*PC)* at any axial position, *z*:

$$\begin{aligned}\frac{\partial\left(\dot{M}_i\right)}{\partial z} &= -k_i \cdot \frac{\dot{M}_i}{v_g} \cdot (1-\varepsilon) \cdot \rho_{cat} \cdot \Phi \\ &+ \sum_{n>i}^{N} p(i,n) \cdot (1-\varphi) \cdot k_n \cdot \frac{\dot{M}_n}{v_g} \cdot (1-\varepsilon) \cdot \rho_{cat} \cdot \Phi\end{aligned} \tag{3.11}$$

where $\dot{M}_i$ is the mass flow rate of i^{th} *PC;* k_i is the cracking rate constant ($m^3/kgcat \cdot h$) of i^{th} *PC*, and Φ is the catalyst activity coefficient. The first term in the right hand side denotes cracking of i^{th} *PC* to smaller molecules; the second term is the formation of that component from cracking of larger molecules. The yield function *p(i,n)* determines the amount of i^{th} *PC* formed from cracking of n^{th} *PC*. For each reaction, φ fraction of the reacting material is converted to coke. The value of φ is estimated from plant data. The catalyst activity coefficient Φ is calculated as explained below.

The overall mass balance between the inlet and outlet of the riser gives:

$$\sum_{i=1}^{N} \dot{M}_i + \dot{C} = \dot{M}_{HVGO} + \dot{C}_0 \tag{3.12}$$

where $\dot{C}_0$ is the coke flow rate (kg/h) on the catalyst entering the riser. The coke mass flow rate $\dot{C}$ leaving the riser is computed from Eq. 3.12:

$$\dot{C} = \dot{M}_{HVGO} - \sum_{i=1}^{N} \dot{M}_i + \dot{C}_0 \tag{3.13}$$

Catalyst activity depends on the coke fraction on the catalyst since coke is the physical reason for deactivation. An exponential type deactivation is used[70]. There are other type of expressions in the literature as well (i.e. [68]). Catalyst activity coefficient is then defined by:

$$\Phi = e^{-\alpha \frac{\dot{C}}{\dot{M}_{cat}}} \tag{3.14}$$

where $\frac{\dot{C}}{\dot{M}_{cat}}$ is the coke fraction on the catalyst and α is a tuning parameter.

3.2.2.4 Energy Balance

The following steady-state energy balance holds at any axial position, *z*:

$$\frac{\partial\left(\dot{M} \cdot c_{p,avg} \cdot T + \dot{M}_{cat} \cdot c_{p,cat} \cdot T\right)}{\partial z} = \sum_{i=1}^{N} \Delta H_i \cdot k_i \cdot \frac{\dot{M}_i}{v_g} \cdot (1-\varepsilon) \cdot \rho_{cat} \cdot \Phi \tag{3.15}$$

where $c_{p,avg}$ is the average heat capacity and ΔH_i is the heat of cracking of i^{th} *PC*.

The heat of cracking of i^{th} pseudo component is calculated from [47]:

$$\Delta H_i = H_{c,coke} \cdot \varphi + \sum_{j=1}^{i} p(j,i) \cdot (1-\varphi) \cdot H_{c,j} - H_{c,i} \tag{3.16}$$

where $H_{c,coke}$ is the heat of combustion of coke; $H_{c,i}$ is the heat of combustion of i^{th} pseudo component.

Since heat of combustion is sensitive to feed content which cannot be directly measured in the refinery, we use a power-law type equation to relate heat of combustion to *NBP*:

$$H_{c,i} = a_c NBP_i^{b_c} \tag{3.17}$$

where a_c and b_c are adjustable parameters.

$H_{c,coke}$ is considered to be a function of *API* gravity of the feed:

$$H_{c,coke} = a_{coke} API_{HVGO} + b_{coke} \tag{3.18}$$

3.2.2.5 Prediction of Final Product Distribution

Component mass balance, Eq. 3.11, gives the distribution of *PC*s in the riser effluent. When the temperature cut-points [29] (TCPs) used in the fractionation unit are known, the amounts of the final products (off-gas, LPG, WCN, LCO and CLO) can be predicted from the distribution of PCs in the riser effluent. This is shown in Fig. 3.6 for a particular day of plant operation. The solid curve represents the boiling point curve of the riser effluent predicted by the model and it is obtained through Eq. 3.11. Since the actual riser effluent boiling point curve cannot be measured in the plant, we blend the available final products' boiling point curves to construct the actual riser effluent boiling point curve. This is shown by the dashed curve in Fig. 3.6.

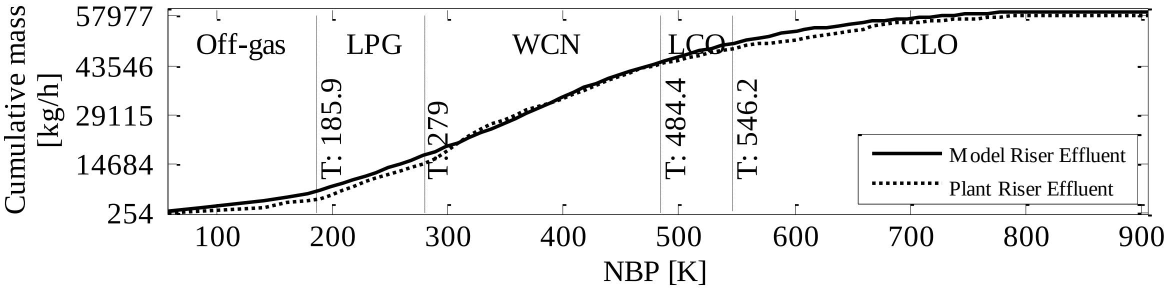

Figure 3.6: Riser effluent curves and TCPs

Each vertical dashed line in Fig. 3.6 represents a *TCP*, whose numerical value is also shown. The yield of each cut (off-gas, LPG, WCN, LCO and CLO) is computed from the intersection of TCPs with the boiling point curve. The TCPs are calculated with the methodology described in chapter 2.8.1.

3.3 Regenerator

In the regenerator coke is burnt to increase the catalyst activity. The compressed air is fed to the bottom of the regenerator after passing through the distributors. Oxygen in the air reacts with the coke and gaseous combustion products are further processed in the *CO* boiler. Since combustion reactions are highly exothermic, regenerated catalyst is transferred back to the riser mixing zone at a high temperature and provides energy for the endothermic reactions occurring in the riser.

We assume that the regenerator has two physical regimes described by the dense bed and the dilute phase (see Fig. 3.1) which are modeled next.

3.3.1 Modeling of the Dense Bed

The dense bed is the lower part of the regenerator where there is a high concentration of catalyst particles. As air travels through the dense bed, oxygen reacts with coke. The air flow rate is not so high to carry the catalyst particles away but it is enough to generate mixing in the dense bed. In practice, there might be catalyst concentration and temperature gradients in the dense bed despite the mixing. This may be important in some cases [89, 90] in which case the dense bed is further divided into two phases: emulsion and bubble phases. In our case, we do not have measurement points in the regenerator to know whether this is significant or not. Therefore, in order to keep it simple, we have modeled the dense bed as a well-mixed CSTR. Similar assumptions have found applications in many other modeling studies [52, 57]. Primary reactions, rate expressions and heat of reactions are presented in Table 3.1.

Table 3.1: Reactions and rate expressions in the regenerator.

Reaction Number	Reaction	Reaction Rate Expression	Heat of Reaction
(I)	$C + {}^1\!/_2 O_2 \xrightarrow{k_{C,CO}} CO$	$r_{C,CO} = k_{C,CO} \cdot \left(\frac{M_{cat}}{V_{DenseBed}} \cdot \frac{Y_{coke}^{Regen}}{MW_{coke}} \right)^{a_1} \cdot \left(P_{O_2}\right)^{a_2}$	$\Delta H_{C,CO}$
(II)	$C + O_2 \xrightarrow{k_{C,CO_2}} CO_2$	$r_{C,CO_2} = k_{C,CO_2} \cdot \left(\frac{M_{cat}}{V_{DenseBed}} \cdot \frac{Y_{coke}^{Regen}}{MW_{coke}} \right)^{a_3} \cdot \left(P_{O_2}\right)^{a_4}$	$\Delta H_{C,CO_2}$
(III)	$CO + {}^1\!/_2 O_2 \xrightarrow{k_{CO,CO_2,c}} CO_2$	$r_{CO,CO_2,c} = k_{CO,CO_2,c} \cdot \frac{M_{cat}}{V_{DenseBed}} \cdot \left(P_{CO}\right)^{a_5} \cdot \left(P_{O_2}\right)^{a_6}$	$\Delta H_{CO,CO_2}$
(IV)	$CO + {}^1\!/_2 O_2 \xrightarrow{k_{CO,CO_2,h}} CO_2$	$r_{CO,CO_2,h} = k_{CO,CO_2,h} \cdot \left(P_{CO}\right)^{a_7} \cdot \left(P_{O_2}\right)^{a_8}$	$\Delta H_{CO,CO_2}$
(V)	$H_2 + {}^1\!/_2 O_2 \xrightarrow{k_{H_2,H_2O}} H_2O$	Instantaneous	$\Delta H_{H_2,H_2O}$

M_{cat} (kg) is the total catalyst mass holdup in the dense bed; $V_{DenseBed}$ (m^3) is the volume of the dense bed; Y_{coke}^{Regen} is the coke mass fraction of the catalyst in the dense phase; MW_{coke} is the molecular weight of coke. $k_{C,CO}$, k_{C,CO_2}, $k_{CO,CO_2,c}$, $k_{CO,CO_2,h}$ and k_{H_2,H_2O} are the reaction rate constants in reactions I, II, III, IV and V, respectively. Combustion rate expressions ($r_{C,CO}$, r_{C,CO_2}, $r_{CO,CO_2,c}$ and $r_{CO,CO_2,h}$) are also shown in Table 3.1. P_{CO} (bar) and P_{O_2} (bar) are the partial pressures of *CO* and *O2*. *CO* combustion can occur through both catalytic and homogenous paths (reactions III-IV). Arthur studied the combustion of carbon without catalyst and determined the ratio of $k_{C,CO}$ and k_{C,CO_2} at various temperatures [91]. Arbel et al. [57] used this to infer combustion rate constants of reactions I and II. Even though the reaction medium is composed of several types of elements, the reaction mechanism is not fully defined due to catalyst influence and hydrodynamic issues. In the literature different reaction mechanisms and numerical values for the reaction orders have been proposed [57, 89, 92]. We have considered the orders of reactions as unknown parameters $[a_1, a_2 \cdots a_8]$ which are estimated from plant data. Unlike *C* and *CO* combustion reactions, burning of *H2* is so fast that it is assumed to occur instantaneously [93]. Even though *H2* does not influence the kinetics of the regenerator by its concentration, the thermal effects are significant because of its high combustion energy [94]. Expressions for the rate constants are given in Eq. 3.24-3.27 [57].

$$k_{C,CO} = \frac{\beta_c e^{-\frac{E_\beta}{RT}} k_{c0} e^{-\frac{E_{c0}}{RT}}}{\beta_c e^{-\frac{E_\beta}{RT}} + 1} \tag{3.24}$$

$$k_{C,CO_2} = \frac{\beta_c e^{-\frac{E_\beta}{RT}}}{\beta_c e^{-\frac{E_\beta}{RT}} + 1} \tag{3.25}$$

$$k_{CO,CO_2,c} = k_{3c0} e^{-\frac{E_{3c}}{RT}} \tag{3.26}$$

$$k_{CO,CO_2,h} = k_{3h0} e^{-\frac{E_{3h}}{RT}} \tag{3.27}$$

where β_c , k_{c0} , K_{3c0} , K_{3h0} , E_β , E_{c0} , E_{3c} and E_{3h} are adjustable parameters for which approximate values are available [57].

Unlike the riser, the dynamics of the dense bed is significant due to its large catalyst holdup. The approximate residence time of the catalyst in the dense bed is about 5-7 minutes. Mass balance for the coke is given by:

$$\dot{M}_{cat} \frac{Y_{coke}^{Riser}}{MW_{coke}} - \dot{M}_{cat} \frac{Y_{coke}^{Regen}}{MW_{coke}} - \left(r_{C,CO} + r_{C,CO_2}\right) V_{DenseBed} = \frac{M_{cat}}{MW_{coke}} \frac{d}{dt}\left(Y_{coke}^{Regen}\right) \tag{3.28}$$

where $(r_{C,CO} + r_{C,CO_2})$ is the combustion rate of coke. Note that the time constant of the plant is primarily affected by M_{cat}, which is kept constant by controlling the catalyst level in the regenerator.

The gaseous species have a residence time of 3-4 sec in the dense bed. Thus, we have assumed pseudo steady-state for the gaseous phase. The mass balance for *CO* in the dense phase is as follows:

$$-\dot{M}_{CO,DenseToDilute} + r_{CO} V_{DenseBed} = 0 \tag{3.29}$$

$\dot{M}_{CO,DenseToDilute}$ is the molar flow rate of *CO* that leaves the dense phase. r_{CO} is calculated from:

$$
\begin{aligned}
r_{CO} = {} & k_{C,CO}\left(\frac{M_{cat}}{V_{DenseBed}}\cdot\frac{Y_{coke}^{Regen}}{MW_{coke}}\right)^{a_1}\cdot\left(P_{O_2}\right)^{a_2} - k_{CO,CO_2,c}\cdot\frac{M_{cat}}{V_{DenseBed}}\cdot\left(P_{CO}\right)^{a_5}\cdot\left(P_{O_2}\right)^{a_6} \\
& - k_{CO,CO_2,h}\cdot\left(P_{CO}\right)^{a_7}\cdot\left(P_{O_2}\right)^{a_8}
\end{aligned}
\tag{3.30}
$$

Similarly, the material balance for CO_2 gives:

$$
-\dot{M}_{CO_2,DenseToDilute} + r_{CO_2}V_{DenseBed} = 0
\tag{3.31}
$$

and

$$
\begin{aligned}
r_{CO_2} = {} & k_{C,CO_2}\left(\frac{M_{cat}}{V_{DenseBed}}\cdot\frac{Y_{coke}^{Regen}}{MW_{coke}}\right)^{a_3}\cdot\left(P_{O_2}\right)^{a_4} + k_{CO,CO_2,c}\frac{M_{cat}}{V_{DenseBed}}\cdot\left(P_{CO}\right)^{a_5}\cdot\left(P_{O_2}\right)^{a_6} \\
& + k_{CO,CO_2,h}\left(P_{CO}\right)^{a_7}\cdot\left(P_{O_2}\right)^{a_8}
\end{aligned}
\tag{3.32}
$$

H_2 is converted to water instantly, and water flow rate that leaves the dense bed is calculated from:

$$
\dot{M}_{H_2O,DenseToDilute} = \dot{M}_{cat}\,Y_{coke}^{Riser}\,\frac{Y_{H_2}^{coke}}{MW_{H_2}}
\tag{3.33}
$$

where $Y_{H_2}^{coke}$ is the H_2 weight fraction in coke. Material balance for O_2 is given by

$$
\dot{M}_{O_2,in} - \dot{M}_{O_2,DenseToDilute} - \dot{M}_{cat}\,Y_{coke}^{Riser}\,\frac{Y_{H_2}^{coke}}{MW_{H_2}}\,\frac{1}{2} + r_{O_2}V_{DenseBed} = 0
\tag{3.34}
$$

where $M_{O_2,in}$ is the molar flow rate of *O2* into the dense bed from the supply air; $\dot{M}_{O_2,DenseToDilute}$ is the molar flow rate of *O2* that leaves the dense bed.

r_{O_2} is calculated from:

$$\begin{aligned} r_{O_2} = & -k_{C,CO} \cdot \left(\frac{M_{cat}}{V_{DenseBed}} \cdot \frac{Y_{coke}^{Regen}}{MW_{coke}} \right)^{a_1} \cdot \left(P_{O_2}\right)^{a_2} \frac{1}{2} - k_{C,CO_2} \cdot \left(\frac{M_{cat}}{V_{DenseBed}} \cdot \frac{Y_{coke}^{Regen}}{MW_{coke}} \right)^{a_3} \cdot \left(P_{O_2}\right)^{a_4} \\ & - k_{CO,CO_2,c} \cdot \frac{M_{cat}}{V_{DenseBed}} \cdot \left(P_{CO}\right)^{a_5} \cdot \left(P_{O_2}\right)^{a_6} \cdot \frac{1}{2} - k_{CO,CO_2,h} \cdot \left(P_{CO}\right)^{a_7} \cdot \left(P_{O_2}\right)^{a_8} \cdot \frac{1}{2} \end{aligned} \tag{3.35}$$

Energy balance for the dense bed is as follows:

$$\begin{aligned} & \left(\dot{M}_{O_2,in} \cdot c_{p,O_2} \cdot T_{air} + \dot{M}_{N_2,in} \cdot c_{p,N_2} \cdot T_{air} + \dot{M}_{cat} \cdot c_{p,cat} \cdot T_{Riser} \right) \\ & - \left(\begin{aligned} & \dot{M}_{O_2,DenseToDilute} \cdot c_{p,O_2} \cdot T_{Regen} + \dot{M}_{N_2,DenseToDilute} \cdot c_{p,N_2} \cdot T_{Regen} + \dot{M}_{cat} \cdot c_{p,cat} \cdot T_{Regen} \\ & + \dot{M}_{CO,DenseToDilute} \cdot c_{p,CO} \cdot T_{Regen} + \dot{M}_{CO_2,DenseToDilute} \cdot c_{p,CO_2} \cdot T_{Regen} \\ & + \dot{M}_{H_2O,DenseToDilute} \cdot c_{p,H_2O} \cdot T_{Regen} \end{aligned} \right) \\ & + Q_{R,DenseBed} V_{DenseBed} + \dot{M}_{cat} Y_{coke}^{Riser} \frac{Y_{H_2}^{coke}}{MW_{H_2}} \Delta H_{H_2,H_2O} \\ & = \frac{d}{dt} \left(\left(M_{cat} + M_{O_2} + M_{N_2} + M_{CO} + M_{CO_2} + M_{H_2O} \right) c_{p,avg} T_{Regen} \right) \end{aligned} \tag{3.36}$$

where T_{Regen} is the dense phase temperature (K); T_{air} is the air temperature (K), and $Q_{R,DenseBed}$ is the heat released per volume due to combustion reactions:

$$
\begin{aligned}
Q_{R,DenseBed} &= k_{C,CO}\left(\frac{M_{cat}}{V_{DenseBed}}\frac{Y_{coke}^{Regen}}{MW_{coke}}\right)^{a_1}\left(P_{O_2}\right)^{a_2}\Delta H_{C,CO} \\
&+ k_{C,CO_2}\left(\frac{M_{cat}}{V_{DenseBed}}\frac{Y_{coke}^{Regen}}{MW_{coke}}\right)^{a_3}\left(P_{O_2}\right)^{a_4}\Delta H_{C,CO_2} \\
&+ k_{CO,CO_2,c}\cdot\frac{M_{cat}}{V_{DenseBed}}\cdot\left(P_{CO}\right)^{a_5}\cdot\left(P_{O_2}\right)^{a_6}\Delta H_{CO,CO_2} \\
&+ k_{CO,CO_2,h}\cdot\left(P_{CO}\right)^{a_7}\cdot\left(P_{O_2}\right)^{a_8}\Delta H_{CO,CO_2}
\end{aligned}
\tag{3.37}
$$

3.3.2 Modeling of the Dilute Phase

In contrast to the dense bed, there is negligible amount of catalyst particles in the dilute phase. Thus, solid coke does not exist in the dilute phase. Dilute phase can be approximated by pseudo-steady-state operation due to high superficial velocity of the gaseous phase. Dilute phase is modeled as adiabatic plug flow reactor in which CO is burnt homogenously only.

The material balance of *CO* at an axial position, *z*, is given by:

$$\frac{d}{dz}\left(\dot{M}_{CO}\right) = -k_{CO,CO_2,h}\cdot\left(P_{CO}\right)^{a_7}\cdot\left(P_{O_2}\right)^{a_8}A_{regen} \tag{3.38}$$

The balance for CO_2:

$$\frac{d}{dz}\left(\dot{M}_{CO_2}\right) = k_{CO,CO_2,h}\cdot\left(P_{CO}\right)^{a_7}\cdot\left(P_{O_2}\right)^{a_8}A_{regen} \tag{3.39}$$

The balance for O_2:

$$\frac{d}{dz}\left(\dot{M}_{O_2}\right) = -k_{CO,CO_2,h} \cdot \left(P_{CO}\right)^{a_7} \cdot \left(P_{O_2}\right)^{a_8} A_{regen} \cdot \frac{1}{2} \tag{3.40}$$

The differential energy balance is given by:

$$\begin{aligned}&-\frac{d}{dz}\left(\begin{aligned}&\dot{M}_{O_2} \cdot c_{p,O_2} \cdot T + \dot{M}_{N_2} \cdot c_{p,N_2} \cdot T \\ &+ \dot{M}_{CO} \cdot c_{p,CO} \cdot T + \dot{M}_{CO_2} \cdot c_{p,CO_2} \cdot T + \dot{M}_{H_2O} \cdot c_{p,H_2O} \cdot T\end{aligned}\right) \\ &+ k_{CO,CO_2,h} \cdot \left(P_{CO}\right)^{a_7} \cdot \left(P_{O_2}\right)^{a_8} \Delta H_{CO,CO_2} A_{regen} = 0\end{aligned} \tag{3.41}$$

3.4 Parameter Estimation

Parameter estimation is necessary to determine reasonable values for the model parameters. The data used in the parameter estimation include a wide range of operating conditions and different types of feed stocks.

Nonlinear weighted steady-state parameter estimation problem is defined by:

$$\min_{\phi} \left(X_p - X_m(\phi)\right)^T W \left(X_p - X_m(\phi)\right) \tag{3.42}$$

Where X_p is the vector of plant measurements; $X_m(\phi)$ is the vector of the model predictions obtained with parameter set ϕ, and W is the weighting matrix. For the riser, plant measurements include the product amounts and the exit temperature. For the regenerator, plant measurements are the exit gas composition and dense phase temperature, dilute phase temperature and coke fraction of the catalyst.

The following parameters are estimated for the riser:

$$\phi_{riser} = \lfloor \beta \quad \mu \quad E_1 \quad E_2 \quad \lambda_p \quad \mu_p \quad \alpha \quad a_c \quad b_c \quad a_{coke} \quad b_{coke} \ \varphi \rfloor \tag{3.43}$$

The following parameters are estimated for the regenerator:

$$\phi_{regen} = \lfloor \beta_c \quad k_{c0} \quad K_{3c0} \quad K_{3h0} \quad E_\beta \quad E_{c0} \quad E_{3c} \quad E_{3h} \quad a_1 \quad a_2 \quad a_3 \quad a_4 \quad a_5 \quad a_6 \quad a_7 \quad a_8 \rfloor \tag{3.44}$$

In parallel with chapter 3.5, the identifiable parameters are determined with corresponding confidence regions. The values are shown in Table 3.2.

Table 3.2: Estimated parameters

	Parameter	Nominal value	95% confidence interval
ϕ_{riser}	λ_p	0.76	0.04
	μ_p	1.64	0.86
	φ	0.069	0.00001
	β	0.024	0.001
	μ	3.32	0.06
	b_c	-0.054	0.00009
ϕ_{regen}	a_2	0.65	0.004
	a_6	0.90	0.006
	a_8	0.95	0.044

3.5 Model Performance

The main outputs of the riser are the exit temperature (T_{Riser}) and the product distribution. Note that the model uses the same *TCP*s as the plant and this makes the predicted final products comparable to the actual data. The available data under consideration include 10 sets of measurements with different feeds and steady-state operating conditions. 4 days were used for training (Δ) and the remaining was used for prediction (•) as shown in Fig. 3.7. The model predicts the overall steady-state performance of the riser quite well, considering that 45 degree line corresponds to perfect estimation.

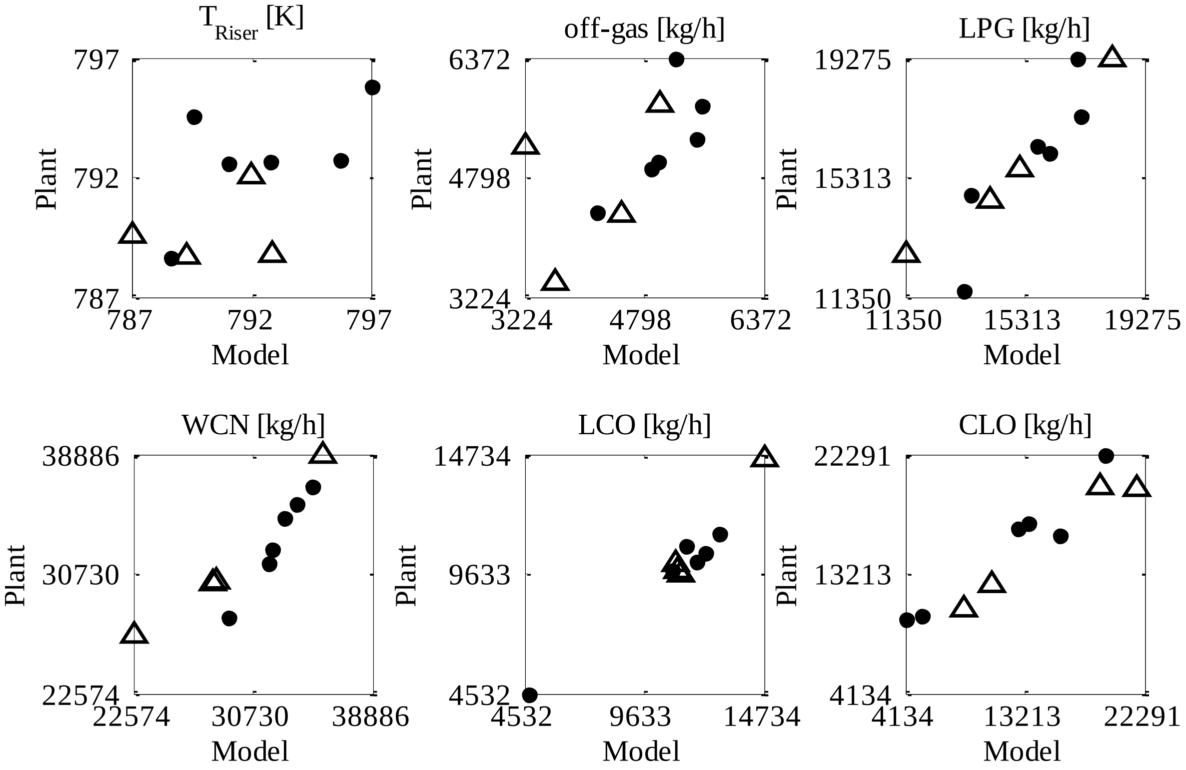

Figure 3.7: Comparison of model and plant for the crucial riser variables.

In Table 3.3, the errors in Fig. 3.7 are quantified by using the absolute deviation (AD):

$$AD_i = \left| x_{p,i} - x_{m,i} \right| \tag{3.45}$$

where $x_{p,i}$ and $x_{m,i}$ are plant measurements and model predictions, respectively. Note that the average absolute deviations for product amounts are less than 10% of their nominal values. Average temperature prediction error in the riser is around 2K.

Table 3.3: *AD*s for crucial riser variables

		T_{Riser} [K]	*Off-gas* [kg/h]	*LPG* [kg/h]	*WCN* [kg/h]	*LCO* [kg/h]	*CLO* [kg/h]
TRAINING	$AD_{AVERAGE}$	1.8	785	849	2923	973	1674
	AD_{MAX}	3.9	1993	1425	4039	1583	1995
	AD_{MIN}	0.2	187	409	2127	160	993
VALIDATION	$AD_{AVERAGE}$	1.8	286	1001	1225	1156	3497
	AD_{MAX}	4.9	1993	2201	4039	1778	5605
	AD_{MIN}	0.1	12	12	292	160	242

A similar comparison is made for the regenerator as shown in Fig. 3.8. Note that the model captures the overall plant behavior of the regenerator as well. In parallel with findings in [57], prediction of after burn gas phase compositions is more challenging both as a result of hydrodynamic effects and difficulty in measuring the average gas phase composition accurately.

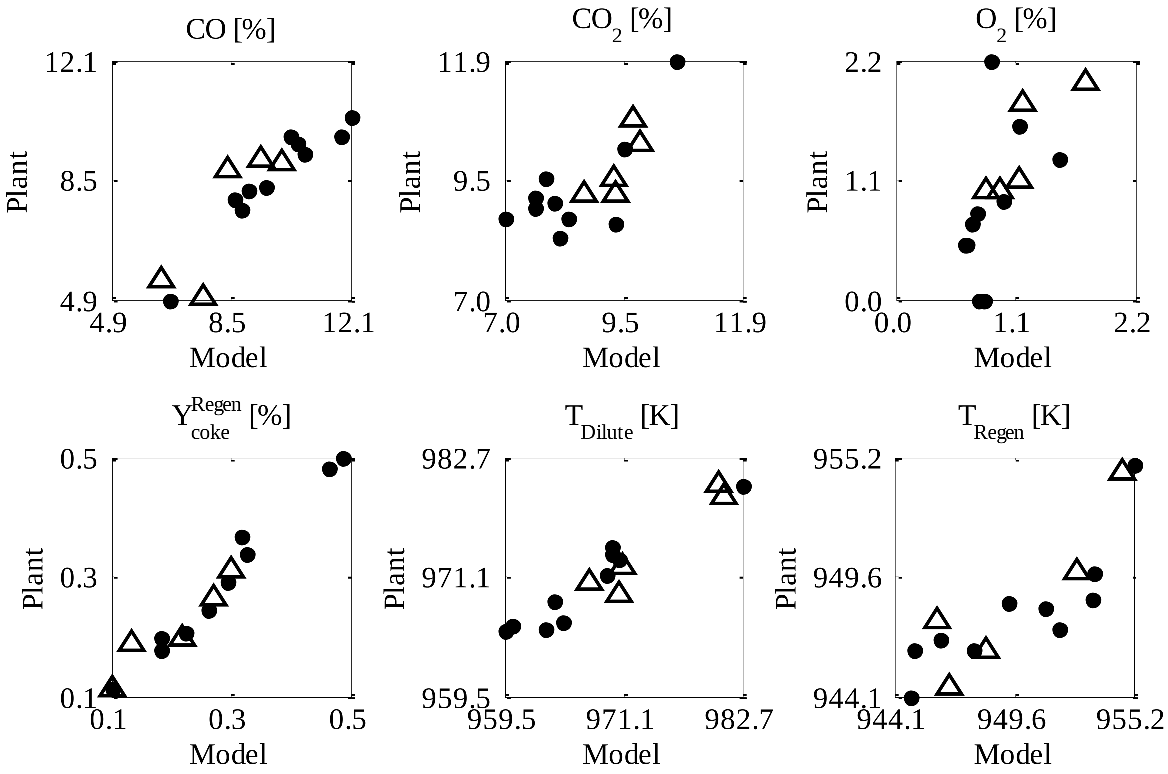

Figure 3.8: Comparison of regenerator model and plant measurements

In Table 3.4, the absolute deviation (AD) errors are given. Average temperature prediction error in the regenerator is around 2K and prediction error in the gaseous products amounts is less than 10%.

Table 3.4: Regenerator predictions

		CO [%]	CO_2 [%]	O_2 [%]	N_2 [%]	Y_{coke}^{Regen} [%]	T_{Dilute} [K]	T_{Regen} [K]
TRAINING	$AD_{AVERAGE}$	1.3	0.5	0.3	0.4	0.03	1.2	1.6
	AD_{MAX}	2.7	1.0	0.6	1.0	0.06	2.1	2.5
	AD_{MIN}	0.3	0.2	0.0	0.0	0.01	0.4	0.1
VALIDATION	$AD_{AVERAGE}$	1.1	0.9	0.3	0.4	0.02	3.2	2.0
	AD_{MAX}	2.0	1.7	1.3	0.7	0.05	6.3	4.6
	AD_{MIN}	0.4	0.1	0.0	0.1	0.00	1.2	0.4

3.6 Potential Application Areas of the Model

The developed model can be used for various purposes including operator training, monitoring, optimization and control. Detailed treatment of these applications is beyond the scope of this study. We present below the important features of the model that are relevant to optimization and control studies.

3.6.1 Plant Operating Window and Economic Optimization

The complex interactions of the riser and the regenerator must be well understood in order to realize the full economic potential of the FCC plant. Using the model, we have evaluated the steady-state solutions corresponding to feasible values of manipulated variables. The resulting operating window is shown in Fig. 3.9 for a particular feed. In this operating window, contours of important process variables and the plant's profit are plotted as a function of catalyst circulation rate ($\dot{M}_{cat}$) and air flow rate ($\dot{M}_{air}$). Once the degrees of freedom is fixed (i.e. $\dot{M}_{cat}$ and $\dot{M}_{air}$ values are assigned), the steady-state solution and the profit can be read from the displayed contours.

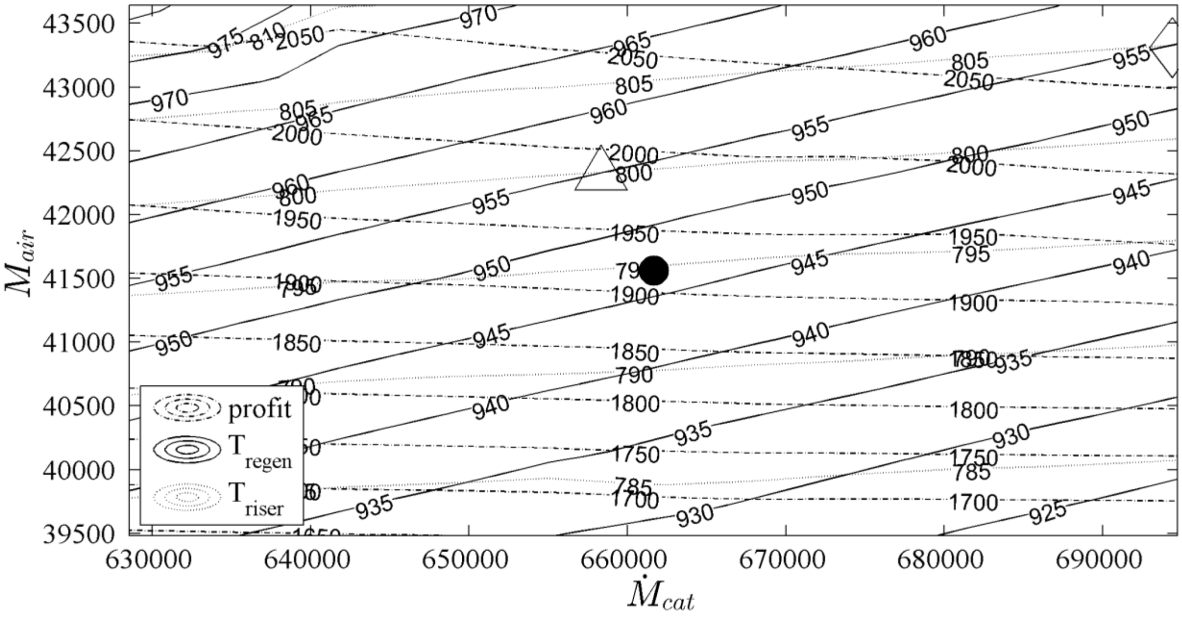

Figure 3.9: Reaction unit temperatures and plant profit in the operating window

For example the point labeled by (●) corresponds to the nominal steady-state operation in the plant. In Fig. 3.9, in addition to the riser and regenerator temperature contours, we have also shown the economic profit which is given by:

$$J = \sum_{i=1}^{5} P_i \cdot \dot{M}_{p,i} - P_{HVGO} \cdot \dot{M}_{HVGO} - U \qquad (3.46)$$

where P_i is the price of the i^{th} product; $\dot{M}_{p,i}$ is the mass flow rate of the i^{th} product; P_{HVGO} is the price of the feed; $\dot{M}_{HVGO}$ is the mass flow rate of the feed; J is the net profit; U is the utility cost. In our case, the utility cost is negligible compared to the economic value of the product and the feed. The prices of products are determined by interactions among different plants in the refinery and the market demand for different products. In order to compute these prices, the planning department uses a refinery-wide linear programming algorithm. Once the prices are set, the optimum steady-state operating point can be calculated from:

$$\begin{aligned}
&\underset{\dot{M}_{cat},\dot{M}_{air}}{Max} \sum_{i=1}^{5} P_i \cdot \dot{M}_{p,i} - P_{HVGO} \cdot \dot{M}_{HVGO} - U \\
&s.t. \\
&\dot{M}_{air,min} \le \dot{M}_{air} \le \dot{M}_{air,max} \\
&\dot{M}_{cat,min} \le \dot{M}_{cat} \le \dot{M}_{cat,max} \\
&T_{regen} \le T_{regen,max} \\
&T_{riser} \le T_{riser,max}
\end{aligned} \tag{3.47}$$

The constraints on the catalyst circulation rate and the air flow rate are capacity constraints, and temperatures are constrained due to safety. In the absence of any temperature constraints, the optimum steady-state corresponds to maximum values of $\dot{M}_{cat}$ and $\dot{M}_{air}$ which is the upper right corner in Fig. 3.9. When the temperatures are constrained, the optimum shifts to different operating points where different constraints become binding. For example, when $T_{Regen,max} = 955K$, the optimum operating point shifts to the diamond (◊) where catalyst circulation and regenerator temperature (instead of air flow rate) are at their maximum limits. If $\dot{M}_{cat,max}$ is 658353 kg/h and $T_{Regen,max} = 955K$, the optimum operating regime further shifts to triangle (Δ) where both regenerator temperature and catalyst circulation constraints become active.

In addition to computation of the optimum steady-state, Fig. 3.9 provides significant insight into understanding of the influence of manipulated variables on the plant profitability. As seen from the contours, the profit is more sensitive to the air flow rate compared to the catalyst circulation. Physically, the air flow increases the extent of the reaction in the regenerator and a hotter temperature catalyst with less coke content is transferred to the riser. This favors cracking at constant catalyst circulation. On the other hand, increasing the catalyst flow rate at constant air flow rate also increases the cracking reactions as a result of increased catalyst concentration in the riser; but the extent is not so significant because of decrease in the temperature.

3.6.2 Dynamic Simulations

Dynamic analysis of the model helps to better understand the interactions between the operation of the riser and the regenerator. Fig. 3.10 shows the model's dynamic response to an increase in the air flow rate by 1000 m^3/h. The amount of air supply determines the extent of combustion reactions. When the air input increases, more combustion reactions occur and more heat is released. Given the constant catalyst circulation rate, the temperature in both the dense and dilute phase increases. Consequently, the coke content of the catalyst decreases. A relatively hotter catalyst is transferred to the riser and the riser temperature increases as well. This high temperature operation results in more cracking as seen in product flow rates. The amount of heavy products (CLO and LCO) decreases whereas the amount of the light products (WCN, LPG) increases.

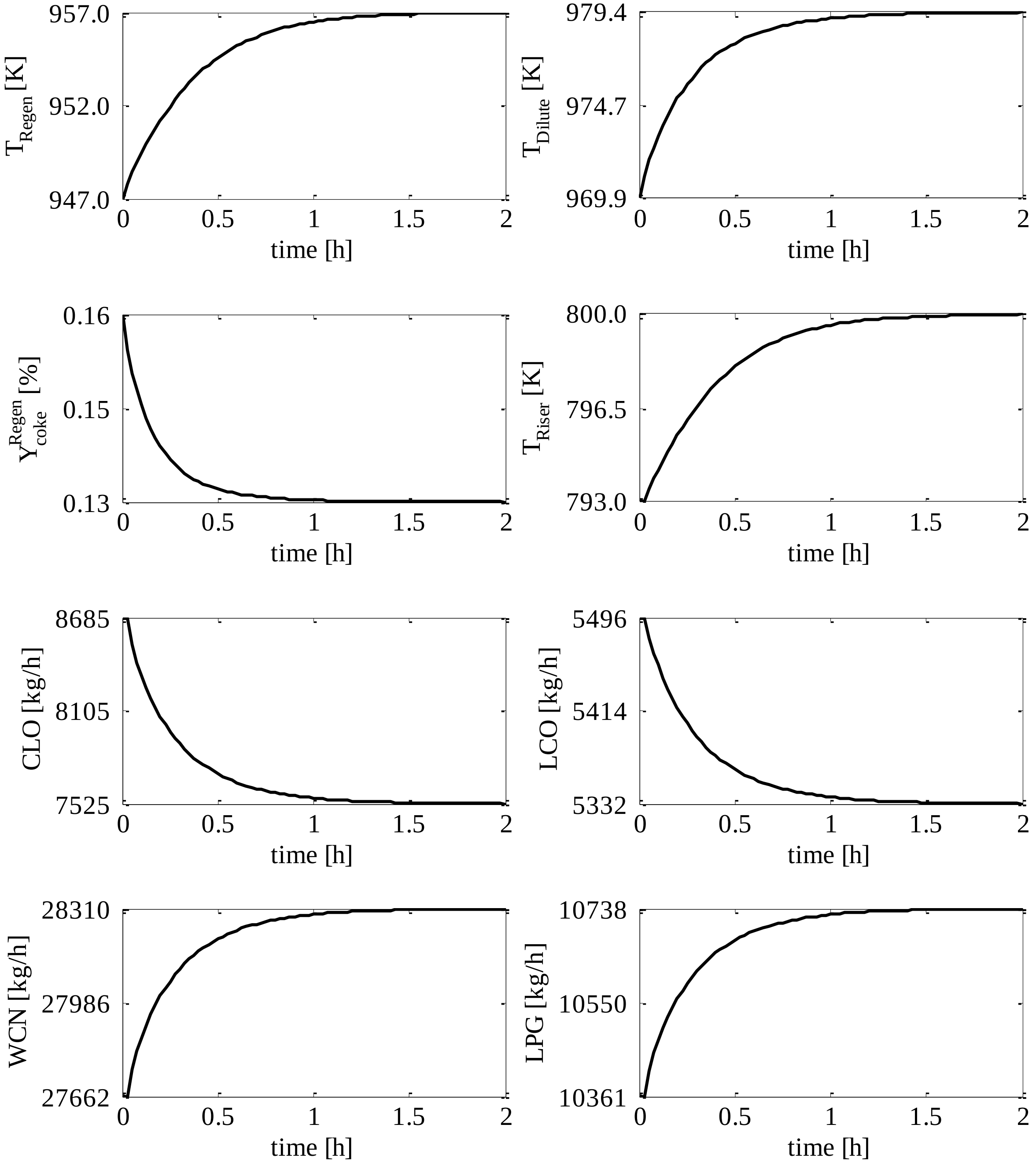

Figure 3.10: Dynamic response of the plant to a step increase in air flow rate by 1000 m^3/h.

Next we study the response to catalyst circulation change. Fig. 3.11 shows the model's dynamic response to an increase of the catalyst circulation rate by 5% keeping the air flow constant. When the catalyst circulation rate increases suddenly, more energy is transferred from the regenerator to the riser and the riser temperature increases suddenly due to its small time constant. The sudden initial increase in riser temperature favors more cracking. As a result of temperature drop in the regenerator, the combustion reactions slow down and the coke fraction on the catalyst increase. Due to both decrease in regenerator temperature and increase in coke amount on the regenerated catalyst, the riser temperature eventually drops. Note that at steady-state the amounts of the light products slightly increase as a result of increased catalyst concentration in the riser.

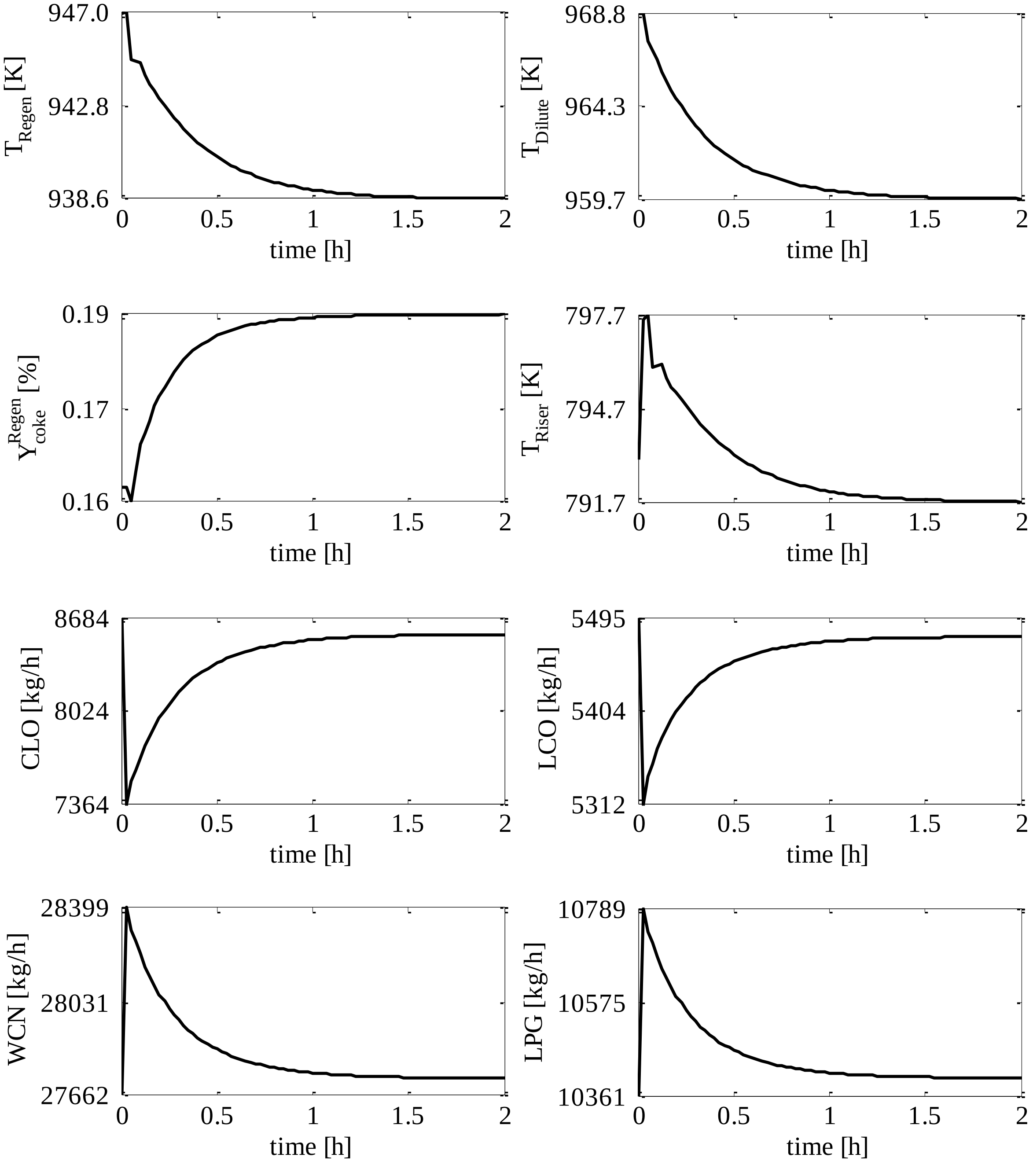

Figure 3.11: Dynamic response of the plant to step catalyst circulation rate increase by 5%

3.7 Design of Control Structure

FCC units have to run under economically optimum operating conditions while maintaining stability and adhering to operational constraints. Therefore, closed-loop control strategies have to address two types of objectives: *regulatory control objectives* and *economic control objectives*. Furthermore these objectives have to be continuously met in the face of external disturbances.

Plant disturbances can be classified according to their frequencies and impact [37]. Slow disturbances with high economic impact require re-optimization and may initiate a change in the operating conditions. For example, changes in the feed quality and product types and prices belong to this class of disturbances which may persist for a relatively long period. For such cases the model parameters can be updated on-line and economic optimization is repeated to determine the new operating conditions. Since these economic disturbances do not change frequently, the closed-loop plant dynamics is favorable to undergo the necessary transition between the different optimum operating conditions. For faster disturbances or for those without significant economic impact, on-line optimization is not warranted. The adverse effects caused by these disturbances are handled by the regulatory controllers.

Economic and regulatory objectives are addressed in real-time through a two-layer approach as shown in Fig.3.12a. [35].

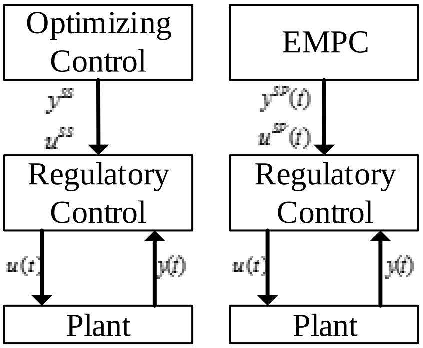

(a) (b)

Figure 3.12: Decomposition of control tasks (a) Traditional two-layer approach (b) Two-layer EMPC.

In practice, most of the time, optimizing control layer performs steady-state optimization to compute the optimal steady-state operating point (y_{ss}, u_{ss}) from the solution of:

$$\begin{aligned}
&\underset{u}{Max}\ \ L_{SS}(y,u,d) \\
&s.t. \\
&y = f_{SS}(u,d) \\
&h(x,u,d) \leq 0
\end{aligned} \tag{3.48}$$

where y is the vector of outputs; u is the vector of inputs or decision variables; d is the vector of economic disturbances; f_{SS} is the steady-state plant model; $L_{ss}(y,u,d)$ is the economic performance index i.e. plant profit in this case. Optimal solution (y_{ss}, u_{ss}) is supplied to the lower regulatory layer as constant set-point (y^{sp}, u^{sp}). Usually, in complex multivariable and constrained industrial applications, regulatory layer consists of a model predictive controller

(RMPC) [95] which tracks the set-points. The classical tracking optimization problem solved by RMPC is given by:

$$
\begin{aligned}
&\underset{u_1,u_2,..,u_N}{Min} \quad J_{RMPC} = \sum_{k=1}^{N} \left(y_k - y^{sp}\right)^T W_y \left(y_k - y^{sp}\right) + \left(u_k - u^{sp}\right)^T W_u \left(u_k - u^{sp}\right) \\
&s.t. \\
&x_{k+1} = f\left(x_k, u_k, d_k\right) \\
&y_k = g(x_k, u_k, d_k) \\
&h(y_k, u_k, d_k) \le 0 \quad k = \{1, \dots, N\}
\end{aligned}
\tag{3.49}
$$

where *k* is the sample time; *N* is the horizon; y_k is the output vector at time *k*; d_k is the vector of disturbances at time *k*; u_k is the vector of inputs; W_y and W_u are weighting matrices of the outputs and inputs, respectively.

Determining steady-state set-points first, followed by tracking is clearly suboptimal when compared with a dynamic optimization formulation which directly optimizes the economic objective function. Economic dynamic optimization performed over a specified time horizon is bound to provide better economic performance since it minimizes the transient cost incurred during transition between different steady-state operations [96-98]. Therefore, a single layer architecture that integrates optimizing and regulatory control tasks has been proposed recently. In particular, Economic Model Predictive Control (EMPC) [96] is such a strategy. EMPC converts the open-loop dynamic optimization into a feedback control strategy by performing it at each sampling time after updating the initial state. Specifically, EMPC implements in real-time the solution of the following dynamic optimization problem:

$$
\begin{aligned}
&\underset{(u_1,u_2,..,u_N)}{Min}\; J_{EMPC} = \sum_{k=1}^{N} L(x_k,u_k) + C(x_N) \\
&s.t. \\
&x_{k+1} = f\,(x_k,u_k,d_k) \\
&h(x_k,u_k,d_k) \le 0 \quad k = \{1,\ldots,N\} \\
&x_N \in \mathrm{X}_f
\end{aligned}
\tag{3.50}
$$

Like in RMPC, the first optimal control move u_k is applied to the plant, and optimization is repeated at the next sampling time after estimating the new state from output measurements. In Eqn. 50, $L(x_k,u_k)$ is the economic stage cost e.g. negative profit; $C(x_N)$ is the terminal cost; and X_f is a compact terminal region containing the steady-state operating point in its interior. Unlike RMPC, stability of EMPCs is more challenging due to primarily the non-convex form of the economic objective function. In [96, 99] stability is ensured by using a terminal state constraint $x_N = x_{ss}$ (final steady-state) instead of the terminal region constraint $x_N \in X_f$ and eliminating the terminal cost term $C(x_N)$. Later Amrit et al. [100] relaxed the terminal constraint to a terminal region constraint $x_N \in X_f$ in order to provide more flexibility. Other techniques to handle stability exist as well [101, 102].

Real-time implementation of the dynamic optimization as a feedback control law requires solving Eq.50 at each sampling time to account for disturbances, modeling and initial state errors. For large scale complex industrial processes, this can be computationally demanding especially when large prediction horizons have to be used to enhance stability and performance. In order to cope with these disadvantages of real-time optimization, a two-layer implementation of EMPC [103-106] has been proposed as shown in Fig. 3.12b.

Here EMPC acts as a supervisory controller driving RMPC by supplying economically optimal time-varying set-point trajectories for the plant outputs. RMPC tracks these trajectories by implementing the necessary changes in the control inputs. Note that this two-layer implementation is proposed on the premise that plant disturbances can be separated into slow (economic) and fast (non-economic) disturbances as discussed earlier. In this case the sampling time for EMPC can be chosen much larger than the sampling time of RMPC so that slow (economic) disturbances are handled by EMPC and fast (non-economic) disturbances are rejected by RMPC. Integrating EMPC with RMPC in a two-layer hierarchy offers significant computational advantages by reducing the frequency of optimization cycle.

Two-layer EMPC implementation benefits both from the economic features of EMPC and the well-established advantages of RMPC such as stability, fast convergence, robustness and constraint handling. In addition in most industrial plants RMPC is already in place and widely used with success. This is indeed the case with the FCC plant under study here as well.

Next we present how we apply EMPC on the FCC plant.

3.7.1 Hierarchical Plant Wide Control Structure

The hierarchical control structure designed for the FCC plant under consideration is shown in Fig. 3.13. Next we describe the function of each block and its interaction with and contribution to the overall hierarchy.

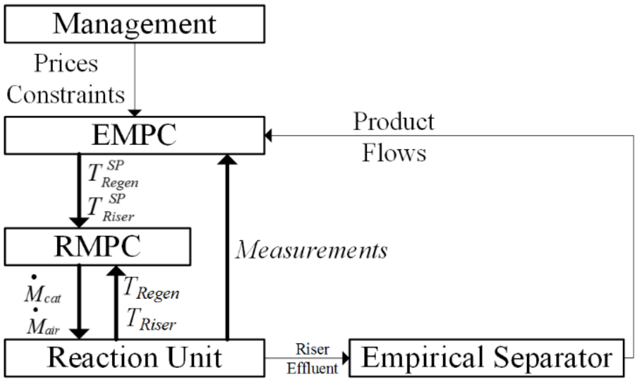

Figure 3.13: Hierarchical FCC control structure.

3.7.1.1 Management

The highest level in the hierarchy is the management layer which provides prices of all individual products considering product demand in the refinery and the market. In addition product specifications and operating constraints are also defined here.

3.7.1.2 EMPC

The plant profit is given by Eq. 3.46. There are two-degrees of freedom and the decision variables are the two inputs: the catalyst circulation rate ($\dot{M}_{cat}$) and the air flow rate ($\dot{M}_{air}$). For different values of these two inputs, the riser and regenerator temperatures, and the profit values are calculated using the steady-state model [107]. Next the steady-state operating window is constructed as shown in Fig. 3.14. From the temperature and profit contours, one can infer the profitability of different steady-state operating conditions. As optimization scenarios, we consider two different sets of product prices. The first set of prices is valid for the first three hours of operation. In this case, the profit increases with catalyst circulation and the air flow rate. Increased $\dot{M}_{cat}$ and $\dot{M}_{air}$ results in higher temperatures and lighter product distribution, and the profit increases when the light products are relatively more valuable. The second set of prices corresponds to a 5% reduction in WCN price, and 5% and 15% increase in LCO and CLO prices, respectively. Once the heavy products LCO and CLO become relatively more valuable, the profit increases with less cracking which occurs when low catalyst circulation and air flow rate are used. This is confirmed by the relative positions of the plant contours for the two scenarios as shown in Fig. 3.14.

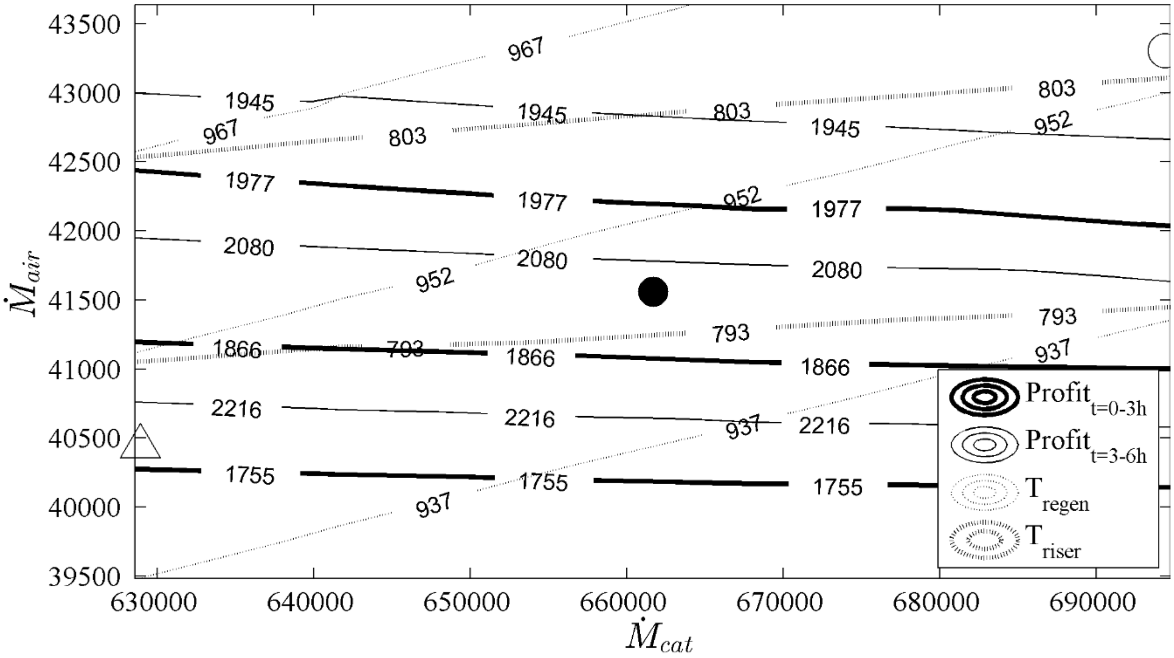

Figure 3.14: FCC operating window.

(●) Plant initial operating point

(○) Optimal operating regime between t=0-3h

(Δ) Optimal operating regime between t=3-6h

In addition to economic considerations, there are some hard constraints which are determined by equipment capacities and the catalyst. These are:

$$\begin{aligned}
&\dot{M}_{air,min} \le \dot{M}_{air} \le \dot{M}_{air,max} \\
&\dot{M}_{cat,min} \le \dot{M}_{cat} \le \dot{M}_{cat,max} \\
&T_{Regen,min} \le T_{Regen} \le T_{Regen,max} \\
&T_{Riser,min} \le T_{Riser} \le T_{Riser,max}
\end{aligned} \tag{3.51}$$

Typical constraint values are listed in Table 3.5:

Table 3.5: Plant constraints

Variable	*Min*	*Max*
$\dot{M}_{air}$ [m^3/h]	39484	43640
$\dot{M}_{cat}$ [kg/h]	628578	694796
T_{Regen} [K]	945.95	955.00
T_{Riser} [K]	787.55	803.25

EMPC uses the profit function as the stage cost and solves the following dynamic optimization:

$$
\begin{aligned}
&\underset{\substack{T^{sp}_{Regen,1},\ T^{sp}_{Regen,2},\dots,T^{sp}_{Regen,N}\\ T^{sp}_{Riser,1},\ T^{sp}_{Riser,2},\dots,\ T^{sp}_{Riser,N}}}{Min} \qquad J^{FCC}_{EMPC} = -\sum_{k=1}^{N}\left(\sum_{i=1}^{5} P_{i,k}\cdot \dot{M}_{p,i,k} - P_{HVGO,k}\cdot \dot{M}_{HVGO,k}\right)\\
&s.t.\\
&x_{k+1} = f_{RMPC}\left(x_k, T^{sp}_{Regen,k}, T^{sp}_{Riser,k}\right)\\
&\dot{M}_{p,k} = g\left(x_k, T^{sp}_{Regen,k}, T^{sp}_{Riser,k}\right)\\
&\left(T^{sp}_{Regen,k}, T^{sp}_{Riser,k}\right)\in\Gamma\\
&T_{Regen,min} \le T^{sp}_{Regen,k} \le T_{Regen,max} \qquad k\in\left(1,\dots,N\right)\\
&T_{Riser,min} \le T^{ref}_{Riser,k} \le T_{riser,max} \qquad k\in\left(1,\dots,N\right)
\end{aligned}
\tag{3.52}
$$

Eq. 3.52 is solved at each sample time to deliver the optimal trajectories $T^{sp}_{Regen,k}, T^{sp}_{Riser,k}$ for $k\in(1,..,N)$ to the RMPC layer. The sampling time for EMPC is 1 hr and the prediction horizon *N*=2. With these choices, plant dynamics allows enough time to track the temperature trajectories and computational load is kept reasonable. The constraint $\left(T^{sp}_{Regen,k}, T^{sp}_{Riser,k}\right)\in\Gamma$ where Γ is closed and bounded is included in the optimization to guarantee that the closed-loop system is stable and the optimal set-point trajectories can be tracked by RMPC [105]. In fact this additional requirement is imposed by the two-layer implementation of EMPC. The set Γ is constructed in such a way that for each set-point value belonging to Γ, there exists feasible values for the lower layer RMPC control inputs, $\dot{M}_{air}$ and $\dot{M}_{cat}$. The set Γ is easily calculated from the steady-state FCC model [107] that relates the riser and regenerator temperatures to the catalyst circulation and air flow rate and their constraint values. In addition to feasibility, closed-loop stability is guaranteed for trajectories belonging to the set Γ by the tuning parameters of RMPC. In our simulations with a single set of tuning parameters, RMPC was able to track the optimal set-point trajectories (see Results). In case of poor tracking, on-line tuning of RMPC or deviation from the optimal trajectory may be required. Finally, EMPC starts the optimization from the estimated state x_k. In the above formulation, it is assumed that the estimated state x_k remains in Γ. Otherwise it has to be projected to this set as done in [105].

Finally, the regenerator and the riser temperature trajectories are constrained by the plant limits as expressed by the last inequalities.

The closed-loop dynamics of RMPC layer is represented by f_{RMPC} in Eq. 3.52. The vector of product flow-rates $\dot{M}_p$ in the objective function is calculated from the empirical fractionator model as explained below [107].

3.7.1.3 RMPC and the Reaction Unit

RMPC controls T_{Regen} and T_{Riser}. Tracking optimization problem is given by:

$$
\begin{gathered}
\underset{\substack{\dot{M}_{air,1},\dot{M}_{air,2},\ldots,\dot{M}_{air,N} \\ \dot{M}_{cat,1},\dot{M}_{cat,2},\ldots,\dot{M}_{cat,N}}}{Min} \quad J_{RMPC}^{FCC} = \sum_{k=1}^{N} \begin{pmatrix} \left(T_{Regen,k} - T_{Regen,k}^{sp}\right)^{T} W_{Regen} \left(T_{Regen,k} - T_{Regen,k}^{sp}\right) \\ + \left(T_{Riser,k} - T_{Riser,k}^{sp}\right)^{T} W_{Riser} \left(T_{Riser,k} - T_{Riser,k}^{sp}\right) \end{pmatrix}
\end{gathered}
$$

$$
\begin{aligned}
& s.t. \\
& x_{k+1} = f_{ReactionUnit}\left(x_k, \dot{M}_{cat,k}, \dot{M}_{air,k}\right) \\
& \\
& \dot{M}_{air,min} \le \dot{M}_{air,k} \le \dot{M}_{air,max} \quad k = \{1,\ldots,N\} \\
& \dot{M}_{cat,min} \le \dot{M}_{cat,k} \le \dot{M}_{cat,max} \quad k = \{1,\ldots,N\} \\
& \Delta\dot{M}_{air,min} \le \Delta\dot{M}_{air,k} \le \Delta\dot{M}_{air,max} \quad k = \{1,\ldots,N\} \\
& \Delta\dot{M}_{cat,min} \le \Delta\dot{M}_{cat,k} \le \Delta\dot{M}_{cat,max} \quad k = \{1,\ldots,N\} \\
& T_{Regen,min} \le T_{Regen,k} \le T_{Regen,max} \quad k = \{1,\ldots,N\} \\
& T_{Riser,min} \le T_{Riser,k} \le T_{Riser,max} \quad k = \{1,\ldots,N\} \\
& \Delta\dot{T}_{Regen,min} \le \Delta\dot{T}_{Regen,k} \le \Delta\dot{T}_{Regen,max} \quad k = \{1,\ldots,N\} \\
& \Delta\dot{T}_{Riser,min} \le \Delta\dot{T}_{Riser,k} \le \Delta\dot{T}_{Riser,max} \quad k = \{1,\ldots,N\}
\end{aligned}
\tag{3.53}
$$

While we have used the nonlinear model explicitly in EMPC to exploit its full economic potential, we have used its linearized version for RMPC since empirical linear step response models are already used in the plant satisfactorily. $f_{ReactionUnit}$ represents the linearized reaction unit model which includes both the riser and regenerator. $\Delta\dot{M}_{air,k}$ and $\Delta\dot{M}_{cat,k}$ are the rate of change of the air flow and the catalyst circulation at time *k*. Constraints include total and rate constraints on the inputs and the temperatures.

3.7.1.4 The Empirical Separator

In order to compute the profit function used in EMPC, individual product amounts are needed. However these amounts are available only after fractionation. Detailed modeling of the fractionation plant is out of the scope of this study. Instead we have developed an empirical model based on temperature cut points which are explained in chapter 3.2.2.5 in detail.

3.7.2 Results

The hierarchical control structure in Fig. 3.13 is based on the temporal decomposition of the control tasks depending on the function and frequency of control actions. The aim of this section is to demonstrate the applicability of current implementation on the model when it is exposed to economic and physical disturbances. More specifically, we are focusing on the effects of changing product prices and the feed content, which change the optimal operation regime.

The performance of the current control approach is tested in a simulation of 9 hours. A significant disturbance which changes the maximum profit region is generated at 3 hour frequency. Next we focus on the corresponding time intervals.

The primary operational objective in the plant had been ensuring the safety until the nonlinear model was developed. In a particular day, the steady state operating point of the plant is market with “●” in Fig. 3.14. That point is considered as an initial point to test our control approach. In such case, the control approach in Fig. 3.13 makes use of product prices provided by the management layer. The same price set is assumed to be valid at first three hours of operation and no other disturbance enters to the plant. Using the prices, in addition to a steady state optimization formulation, the current implementation provides optimal transition to the maximum profit regime, which is denoted by circle (○) at the upper right for this price set. Therefore higher temperature reference trajectories on the regenerator and the riser are calculated by the EMPC considering the dynamic profit profile and the constraints along the path. The set point trajectories provided by EMPC (SV) and the temperature values of the plant (PV) are shown in Fig. 3.15. The objective function in EMPC (see Eq. 3.52) maximizes the plant profit directly; in turn the steepest probable increase in the profit is obtained with current tuning settings.

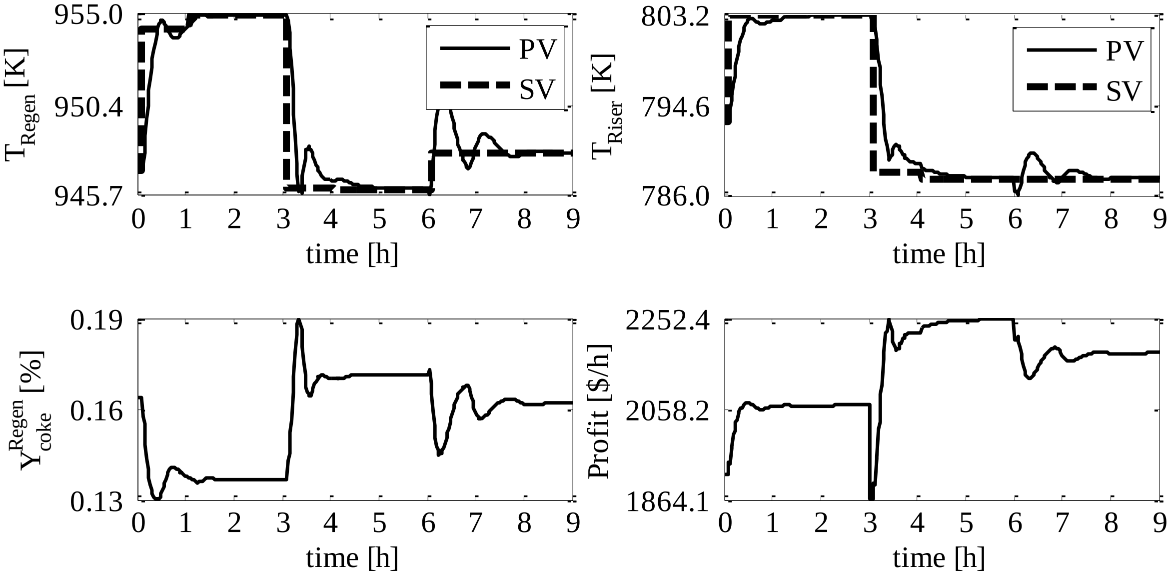

Figure 3.15: Crucial process variables in the simulation.

The steady state values of optimal processing conditions are already known from Fig. 3.14. However, whole economic potential of the profit can only be exploited when their interactions have been considered in the determination of dynamic behavior. Note that, from the steady state behavior, the sensitivities of profit to these temperatures are different because of plant nature. With given set of prices, at constant riser temperature, the increase of the regenerator temperature reduces the profit since the plant produces heavier products more when they are relatively less valuable. On the other hand, higher riser temperatures deliver more profit at constant regenerator temperature since this shift favors production of lighter products and thus more profit. However, both temperatures should be increased as due to physical connection of the units (see definition of Γ in Eq. 3.52). Making use of nonlinear plant model, EMPC provides optimal set point combination of the two. In the lower level, RMPC increases the air flow rate and the catalyst circulation rate. Physically, when the air flow rate to the regenerator increases, the burning reactions in the regenerator are favored reducing the coke content on the catalyst (see Fig. 3.15). In turn, the regenerator temperature increases significantly. To adjust the regenerator temperature and to carry more energy to the riser, the catalyst circulation rate is also increased. Eventually, the riser temperature also adjusted. The dynamic profiles of the manipulated variables are shown in Fig. 3.16.

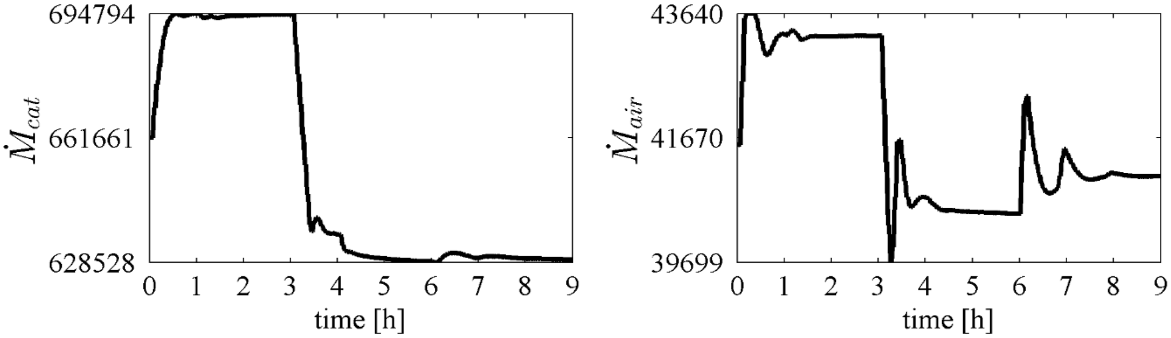

Figure 3.16: Manipulated variables of RMPC

The rise in temperatures favor reducing the amount of heavy products (CLO and LCO) as shown in Fig. 3.17. Overall, the plant profit sharply increases due to the economic weight of light products (off-gas, LPG, and WCN). Since the amount of LPG and WCN is much larger than off-gas, we have plotted them only for demonstration purposes. The new steady state is obtained after approximately 2 hours.

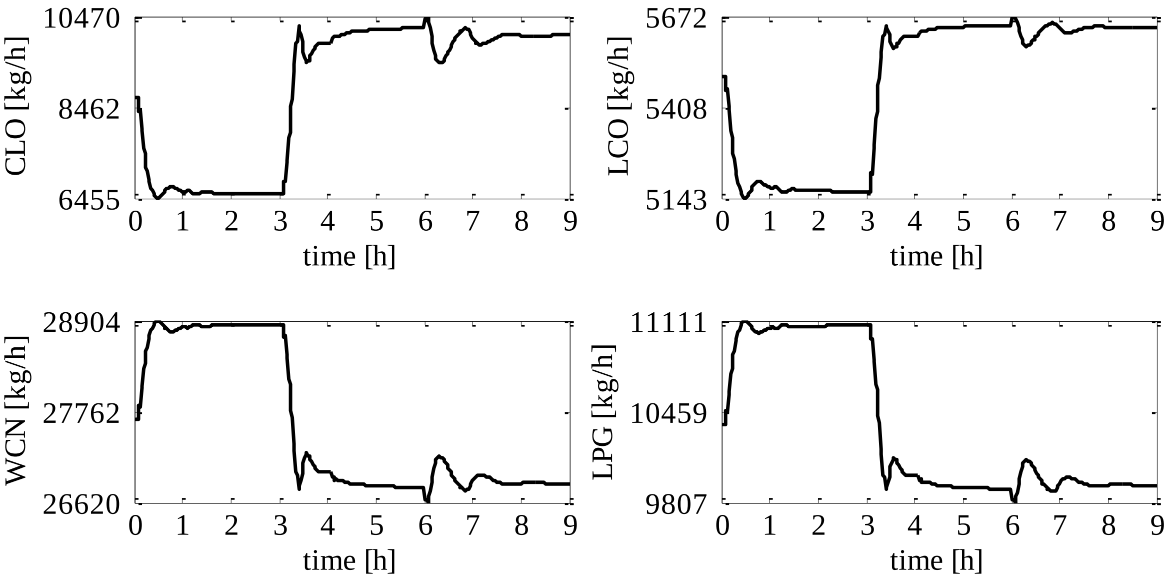

Figure 3.17: Product flow rates

At t=3, a hypothetical price change (see chapter 3.7.1.2) which shifts the profit contours drastically in Fig. 3.14 is imposed on the plant. The price change at this magnitude is probable in the refinery and they do not happen in hourly basis. For this hypothetical case, the plant profit decreases sharply at the time of change. Once the heavy products become relatively more valuable, EMPC provides lower riser and regenerator temperature set points as shown in Fig. 3.15. Note that same Γ is still valid because it is only a function of the feed, the catalyst and other physical disturbances. EMPC calculates lower set point trajectories which necessitate the RMPC to reduce the manipulated variables. The lower catalyst circulation and air input eventually reduces the cracking activity after temperatures drop. Eventually, the amount of heavy products increases and this is reflected on the profit instantly.

In addition to changing economic considerations, the physical disturbances in the plant shift the optimal operating regime and available profit margin. There are various physical disturbances in the plant; terminal deactivation of catalyst, hydrodynamic effects in the reaction units, inefficiencies in the cyclones, measurement errors and fluctuations in the feed content are common examples. Some of these disturbances have small characteristic times and do not affect the plant performance significantly. On the other hand, some disturbances persist for a long time and might require adjustments in all control layers. Usually, it is difficult to determine the exact source of the disturbance due to analysis and measurement challenges; but the feed content is known to fluctuate in daily operation since it is a mixture of various refinery effluents. For that reason, we have chosen the feed content change as a descriptive disturbance which might reflect a daily experience. The new feed has relatively higher average boiling point temperature compared to the feed at the beginning of the process. However, the amount is fixed at its same value by the management layer. The steady state model is used again to calculate the new operating window and Γ. The new temperatures and the profits are shown in Fig. 3.18.

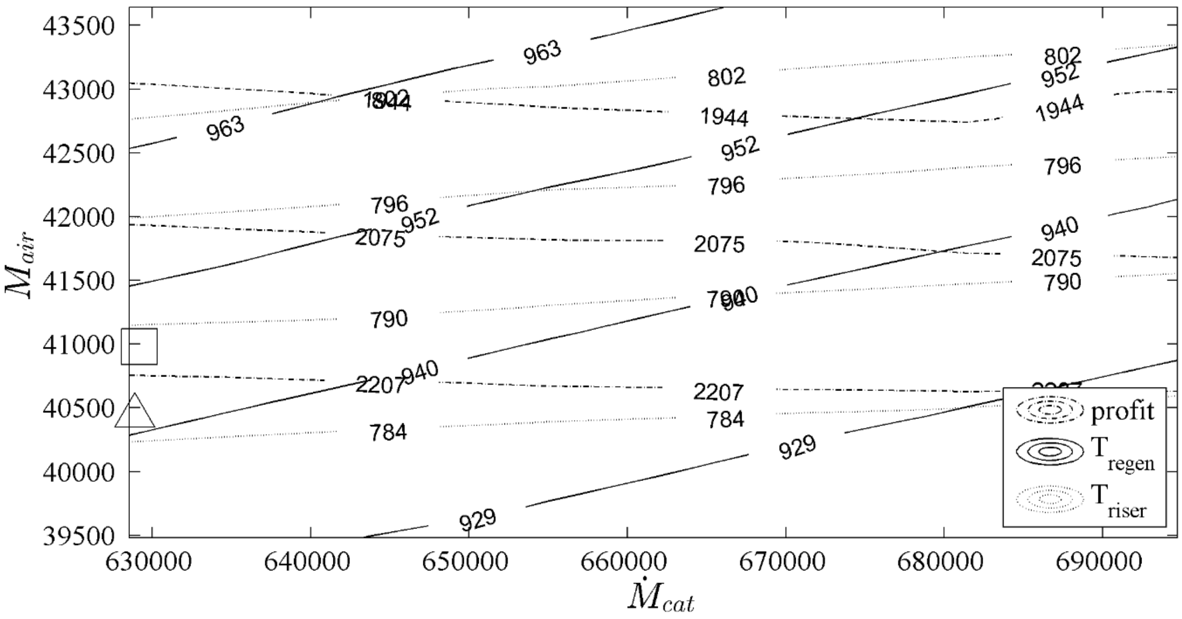

Figure 3.18: The operating window for heavier feedstock

(□) Optimal operating regime between t=6-9h

The temperature contours in Fig. 3.18 are different from Fig. 3.14 since the feed content affects the cracking reactions in the riser. The ultimate effect is reflected on the product distribution and thus profit contours. Usually, the economic issues (changes of prices) have higher impact on the optimal operating regime. The disturbance from the feed content also changes optimal operating regime but smaller adjustments are required to satisfy plant constraints.

The heavier feedstock enters the plant at t=6 while product prices are kept constant. The constraints in Table 3.5 are violated because of decrease in the resulting riser temperature (see Fig. 3.15). EMPC determines the new feasible set points to RMPC to move the plant from previous optimal condition, Δ, to new optimal operating regime in Fig. 3.18 (□). To satisfy the temperature limits, the control actions of RMPC is relatively more aggressive. For that purpose, the air flow rate is increased and the catalyst circulation rate is adjusted slightly. The change of the feed content and the operating conditions result in some loss of heavy products eventually, which results in decrease in overall plant profit.

3.7.3 Conclusions

Using the method of discrete lumping, we have developed a model for an industrial fluid catalytic cracker. The model predicts the riser and regenerator temperatures and product yield under dynamic and steady-state conditions. Empirical correlations that describe the reaction mechanism with few parameters are constructed from literature data. Model parameters are determined from plant data using parameter estimation. Steady-state model predictions predict plant data closely. Simulations show that the model also explains the dynamic interactions between the riser and regenerator. Among many potential applications, the model is especially suited for real-time optimization and control. In this paper we have shown how the feasible operating window and optimum steady-state operating conditions can be ascertained from the model.

FCC process are very complex with very complex chemistry and unknown driving forces. Real-time optimization of the process is very important since the plant produces crucial outputs at significant amounts. In this study, we have designed a hierarchical control structure which decomposes control tasks based on plant needs and the characteristics of the process. At the upper level, EMPC provides set point trajectory for the lower level conventional RMPC. In this structure, EMPC determines the optimal set points considering the plant profile using the dynamic model. In the lower level, RMPC adjusts plant manipulated variables to control the temperatures which is determined by the EMPC. This structure enables smooth and fast transition despite disturbances.

Chapter 4

CONCLUSIONS

Even though significant improvements are obtained in theory, process equipment, monitoring tools and computational advances, the real time optimization of refinery processes is still a challenge due to recent tightening specifications from market. Those specifications push engineers further to integrate processes while searching for efficiencies, which in turn results in more complex processes. In addition to efficiency considerations, the structure of the materials in the reaction media require continuous upgrades due to high amount of impurities inside the crude oil.

The chemical complexity of cracking processes has not been revealed clearly for development of very detailed models. In addition, the analysis of petroleum fractions in molecular details is not practical. For that reasons, the cracking processes are exposed to many unknown driving forces and disturbances. In this study, we have focused on two different industrial cracking processes. Both models make use of easily measurable process variables and construct expressions from the qualitative and quantitative literature data.

The hydrocracker reactor is modeled using the method of continuous lumping while developing existing knowledge in the literature for applications in nonisothermal and dynamic modelling problems. In addition to first principle reactor models, a new generation of empirical dynamic fractionation model which incorporates the online measurements with temperature cut points is developed. The real time optimization is implemented on the models with a hierarchical control structure at which local control blocks of individual units are coordinated. The supervisory controller actions adjust the product distribution which directly determines the plant profit and local control blocks ensure the plant safety and operation desired by coordinator. The coordinating actions in the high level drive the overall plant to optimum operating regime despite large time delay between individual units and plant disturbances.

The method of discrete lumping is utilized to calculate narrow fractions in the reaction media. Semi empirical correlations which use the intrinsic properties to model the cracking behavior of small fractions were developed with few tuning parameters. The model is very flexible for industrial implantation purposes to carry optimization and control objectives. In addition to traditional model predictive control approaches, in this study, we also design economic model predictive controller which includes the plant profit in the objective function directly. The stability of the plant is guaranteed with a cascaded interaction of the controllers. The case studies reveal that the current implementation provides fast transition despite changing economic conditions and physical disturbances.

Among refinery processes, the cracking processes remain important both due to increasing demand for light products and requirements for heavier feedstock processing. A crucial problem in the derivation of practical models is the analysis challenges which enable the considerations of chemical details. Almost all models in the literature, including ones developed in this study, are based on basic measurements. Today’s complex and interacting plants require a better description of chemical composition for feed forward control actions and optimize the overall plant with blending operations. Thus, in the near future research areas that provide practical solutions to feed and product characterization which can be used in the reaction expressions might push the model performances.

BIBLIOGRAPHY

[1] H. Kumar, G.F. Froment, Mechanistic kinetic modeling of the hydrocracking of complex feedstocks, such as vacuum gas oils, Ind Eng Chem Res, 46 (2007) 5881-5897.
[2] M.T. Klein, G. Hou, Mechanistic kinetic modeling of heavy paraffin hydrocracking, Practical Advances in Petroleum Processing, 2 (2006).
[3] R.J. Quann, Modeling the chemistry of complex petroleum mixtures, Environ Health Persp, 106 (1998) 1441-1448.
[4] R.J. Quann, S.B. Jaffe, Structure-Oriented Lumping - Describing the Chemistry of Complex Hydrocarbon Mixtures, Ind Eng Chem Res, 31 (1992) 2483-2497.
[5] R.J. Quann, S.B. Jaffe, Building useful models of complex reaction systems in petroleum refining, Chem Eng Sci, 51 (1996) 1615-&.
[6] G.G. Martens, G.B. Marin, Kinetics for hydrocracking based on structural classes: Model development and application, Aiche J, 47 (2001) 1607-1622.
[7] T.C. Ho, Modeling of reaction kinetics for petroleum fractions, in: C.S.H.a.P.R. Robinson (Ed.) Practical Advances in Petroleum Processing, Springer, 2006.
[8] S.A.Q.G.R. Hill, Hydrocracking of gas oils, Ind. Eng. Chem. Pro. Des. Dev., 8 (1969) 98-105.
[9] V.W. Weekman, D.M. Nace, Kinetics of catalytic cracking selectivity in fixed, moving, and fluid bed reactors, Aiche J, 16 (1970) 397-404.
[10] B.E. Stangeland, Kinetic model for prediction of hydrocracker yields, Ind. Eng. Chem. Proc. Des. Dev., 13 (1974).
[11] V.W. Weekman, Lumps, models and kinetics in practice, Chem. Eng. Prog. Monogr. Ser., 75 (1979).
[12] S. Mohanty, D.N. Saraf, D. Kunzru, Modeling of a Hydrocracking Reactor, Fuel Process Technol, 29 (1991) 1-17.
[13] N. Bhutani, A.K. Ray, G. Rangaiah, Modeling, simulation, and multi-objective optimization of an industrial hydrocracking unit, Ind Eng Chem Res, 45 (2006) 1354-1372.
[14] T. DeDonder, in: L'Affinite, Paris, 1931.
[15] R. Aris, G.R. Gavalas, On the theory of reactions in continuous mixtures, Phil. Trans. Roy. Soc. Lond. Ser. A, 260 (1966) 351-393.
[16] M.Y. Chou, T.C. Ho, Continuum Theory for Lumping Nonlinear Reactions, Aiche J, 34 (1988) 1519-1527.
[17] P. Cicarelli, G. Astarita, A. Gallifuoco, Continuous kinetic lumping of catalytic cracking processes, Aiche J, 38 (1992) 1038-1044.
[18] C.S. Laxminarasimhan, R.P. Verma, P.A. Ramachandran, Continuous lumping model for simulation of hydrocracking, Aiche J, 42 (1996) 2645-2653.
[19] K. Basak, M. Sau, U. Manna, R.P. Verma, Industrial hydrocracker model based on novel continuum lumping approach for optimization in petroleum refinery, Catal Today, 98 (2004) 253-264.

[20] I. Elizalde, M.A. Rodriguez, J. Ancheyta, Application of continuous kinetic lumping modeling to moderate hydrocracking of heavy oil, Appl Catal a-Gen, 365 (2009) 237-242.

[21] H.M.S. Lababidi, F.S. AlHumaidan, Modeling the Hydrocracking Kinetics of Atmospheric Residue in Hydrotreating Processes by the Continuous Lumping Approach, Energ Fuel, 25 (2011) 1939-1949.

[22] J. Govindhakannan, J.B. Riggs, On the construction of a continuous concentration-reactivity function for the continuum lumping approach, Ind Eng Chem Res, 46 (2007) 1653-1656.

[23] D. Bessieres, H. Saint-Guirons, J.L. Daridon, Measurement and calculation of heat capacity of heavy distillation cuts under pressure up to 40 MPa, J Therm Anal Calorim, 58 (1999) 39-49.

[24] L.P. Gilyazetdinov, Heat capacity of petroleum fractions, Chem Tech Fuels Oil+, 31 (1995) 135-137.

[25] V.M. Kurganov, A.B. Gorshtein, G.Y. Starodubskaya, Calculation of Heats of Reaction in Hydrocracking, Chem Tech Fuels Oil+, 16 (1980) 612-616.

[26] S.B. Jaffe, Kinetics of heat release in petroleum hydrogenation, Ind. Eng. Chem. Process Des. Develop., 13 (1974) 34-39.

[27] W.L. Nelson, Petroleum Refinery Engineering, McGraw Hill, 1988.

[28] T.V. Choudhary, P.F. Meier, Characterization of heavy petroleum feedstocks, Fuel Process Technol, 89 (2008) 697-703.

[29] W. Li, C.-W. Hui, A. Li, Integrating CDU, FCC and product blending models into refinery planning, Comput Chem Eng, 29 (2005) 2010-2028.

[30] I. Ioslovich, P.-O. Gutman, I. Seginer, Dominant parameter selection in the marginally identifiable case, Math Comput Simulat, 65 (2004) 127-136.

[31] K. Schittkowski, Experimental Design Tools for Ordinary and Algebraic Differential Equations, Ind Eng Chem Res, 46 (2007) 9137-9147.

[32] G.C. Goodwin, R.L. Payne, Dynamic System Identification. Experiment Design and Data Analysis, New York, 1977.

[33] S. Kemaloglu, E.Ö. Kuzu, D. Gökçe, Ö. Cetin, Model predictive control of a crude distillation unit an industrial application, in: 7th IFAC International Symposium on Advanced Control of Chemical Processes, Istanbul, 2009, pp. 880-885.

[34] M.R. Riazi, Characterization and properties of petroleum fractions, ASTM International, West Conshohocken, PA, 2005.

[35] M. Morari, Y. Arkun, G. Stephanopoulos, Studies in the Synthesis of Control-Structures for Chemical Processes .1. Formulation of the Problem - Process Decomposition and the Classification of the Control Tasks - Analysis of the Optimizing Control-Structures, Aiche J, 26 (1980) 220-232.

[36] H.A. Simon, The Architecture of Complexity, Proceedings of the American Philosophical Society, 106 (1962) 467-482.

[37] I. Lefkowitz, Multilevel Approach Applied to Control System Design, Journal of Basic Engineering, 88 (1966) 392-398.

[38] M.D. Mesarovic, D. Macko, Y. Takahara, Theory of hierarchical, multilevel, systems, Academic Press, New York [u.a., 1979.

[39] M.L. Darby, M. Nikolaou, J. Jones, D. Nicholson, RTO: An overview and assessment of current practice, Journal of Process Control, 21 (2011) 874-884.

[40] R. Scattolini, Architectures for distributed and hierarchical Model Predictive Control - A review, Journal of Process Control, 19 (2009) 723-731.

[41] A. Ulbig, M. Arnold, S. Chatzivasileiadis, G. Andersson, I.W.C. th, Framework for multiple time-scale cascaded MPC application in power systems, IFAC Proc. Vol. (IFAC-PapersOnline) IFAC Proceedings Volumes (IFAC-PapersOnline), 18 (2011) 10472-10480.

[42] A. Kumar, P. Daoutidis, Nonlinear dynamics and control of process systems with recycle, Journal of Process Control, 12 (2002) 475-484.

[43] C.M. Ying, B. Joseph, Performance and stability analysis of LP-MPC and QP-MPC cascade control systems, Aiche J, 45 (1999) 1521-1534.

[44] R. Cheng, J.F. Forbes, W.S. Yip, Price-driven coordination method for solving plant-wide MPC problems, Journal of Process Control, 17 (2007) 429-438.

[45] J.B. Rawlings, B.T. Stewart, Coordinating multiple optimization-based controllers: New opportunities and challenges, Journal of Process Control, 18 (2008) 839-845.

[46] R. Sadeghbeigi, Fluid Catalytic Cracking Handbook: Design, Operation, and Troubleshooting of FCC Facilities, Gulf, 2000.

[47] R.K. Gupta, V. Kumar, V.K. Srivastava, New generic approach for the modeling of fluid catalytic cracking (FCC) riser reactor, Chem Eng Sci, 62 (2007) 4510-4528.

[48] V. W. Weekman, D.M. Nace, Kinetics of catalytic cracking selectivity in fixed, moving and fluid bed reactors, AIChE J., 16 (1970).

[49] L.-S. Lee, Y.-W. Chen, T.-N. Huang, W.-Y. Pan, Four-lump kinetic model for fluid catalytic cracking process, The Canadian Journal of Chemical Engineering, 67 (1989) 615-619.

[50] I.-S. Han, C.-B. Chung, Dynamic modeling and simulation of a fluidized catalytic cracking process. Part I: Process modeling, Chem Eng Sci, 56 (2001) 1951-1971.

[51] C. Jia, S. Rohani, A. Jutan, FCC unit modeling, identification and model predictive control, a simulation study, Chemical Engineering and Processing: Process Intensification, 42 (2003) 311-325.

[52] R. Roman, Z.K. Nagy, M.V. Cristea, S.P. Agachi, Dynamic modelling and nonlinear model predictive control of a Fluid Catalytic Cracking Unit, Comput Chem Eng, 33 (2009) 605-617.

[53] G.M. Bollas, A.A. Lappas, D.K. Iatridis, I.A. Vasalos, Five-lump kinetic model with selective catalyst deactivation for the prediction of the product selectivity in the fluid catalytic cracking process, Catal Today, 127 (2007) 31-43.

[54] J. Corella, E. Frances, On the Kinetic Equation of Deactivation of Commercial Cracking (Fcc) Catalysts with Commercial Feedstocks, in: H.B. Calvin, B.B. John (Eds.) Studies in Surface Science and Catalysis, Elsevier, 1991, pp. 375-381.
[55] J.A. Souza, J.V.C. Vargas, O.F. Von Meien, W. Martignoni, S.C. Amico, A two-dimensional model for simulation, control, and optimization of FCC risers, Aiche J, 52 (2006) 1895-1905.
[56] S.M. Jacob, B. Gross, S.E. Voltz, V.W. Weekman, A lumping and reaction scheme for catalytic cracking, Aiche J, 22 (1976) 701-713.
[57] A. Arbel, Z.P. Huang, I.H. Rinard, R. Shinnar, A.V. Sapre, Dynamic and Control of Fluidized Catalytic Crackers .1. Modeling of the Current Generation of Fccs, Ind Eng Chem Res, 34 (1995) 1228-1243.
[58] S. Kumar, A. Chadha, R. Gupta, R. Sharma, CATCRAK: A Process Simulator for an Integrated FCC-Regenerator System, Ind Eng Chem Res, 34 (1995) 3737-3748.
[59] H. Ali, S. Rohani, Dynamic modeling and simulation of a riser-type fluid catalytic cracking unit, Chem Eng Technol, 20 (1997) 118-130.
[60] M.P. Martin, C. Derouin, P. Turlier, M. Forissier, G. Wild, J.R. Bernard, Catalytic Cracking in Riser Reactors - Core-Annulus and Elbow Effects, Chem Eng Sci, 47 (1992) 2319-2324.
[61] I.S. Han, C.B. Chung, Dynamic modeling and simulation of a fluidized catalytic cracking process. Part I: Process modeling, Chem Eng Sci, 56 (2001) 1951-1971.
[62] R. Sadeghbeigi, Fluid catalytic cracking handbook, Gulf Pub. Co., 1995.
[63] A. Pekediz, D. Kraemer, A. Blasetti, H. deLasa, Heats of catalytic cracking. Determination in a riser simulator reactor, Ind Eng Chem Res, 36 (1997) 4516-4522.
[64] J.M. Arandes, M.J. Azkoiti, J. Bilbao, H.I. de Lasa, Modelling FCC units under steady and unsteady state conditions, The Canadian Journal of Chemical Engineering, 78 (2000) 111-123.
[65] A.P.I.R. Dept, Technical Data Book - Petroleum Refining, American Petroleum Institute, 1983.
[66] J.S. Buchanan, Analysis of Heating and Vaporization of Feed Droplets in Fluidized Catalytic Cracking Risers, Ind Eng Chem Res, 33 (1994) 3104-3111.
[67] J.L. Mauleon, J.C. Courcelle, FCC Heat-Balance Critical for Heavy Fuels, Oil Gas J, 83 (1985) 64-70.
[68] F. Van Landeghem, D. Nevicato, I. Pitault, M. Forissier, P. Turlier, C. Derouin, J.R. Bernard, Fluid catalytic cracking: modelling of an industrial riser, Applied Catalysis A: General, 138 (1996) 381-405.
[69] T.S. Pugsley, F. Berruti, A predictive hydrodynamic model for circulating fluidized bed risers, Powder Technol, 89 (1996) 57-69.
[70] J.L. Fernandes, J.J. Verstraete, C.I.C. Pinheiro, N.M.C. Oliveira, F. Ramôa Ribeiro, Dynamic modelling of an industrial R2R FCC unit, Chem Eng Sci, 62 (2007) 1184-1198.

[71] G.M. Bollas, I.A. Vasalos, A.A. Lappas, D.K. Iatridis, G.K. Tsioni, Bulk Molecular Characterization Approach for the Simulation of FCC Feedstocks, Ind Eng Chem Res, 43 (2004) 3270-3281.
[72] W. Ginzel, How Feed Quality Effects Fcc Performance, Erdol Kohle Erdgas P, 39 (1986) 447-451.
[73] R.T. Powell, C.-y. Yu, Refinery Reaction Modeling Trends, Hydrocarbon Engineering, (2004) 21-26.
[74] R.V. Shendye, R.A. Rajadhyaksha, Analysis of product selectivity in cracking of long chain hydrocarbons by simulation of the molecular processes, Chem Eng Sci, 47 (1992) 661-672.
[75] D.M. Nace, Catalytic Cracking over Crystalline Aluminosilicates. II. Application of Microreactor Technique to Investigation of Structural Effects of Hydrocarbon Reactants, Product R&D, 8 (1969) 31-38.
[76] D.K. Liguras, D.T. Allen, Structural models for catalytic cracking. 1. Model compound reactions, Ind Eng Chem Res, 28 (1989) 665-673.
[77] Y.H. Lin, M.H. Yang, Chemical catalysed recycling of polypropylene over a spent FCC catalyst and various commercial cracking catalysts using TGA, Thermochimica Acta, 470 (2008) 52-59.
[78] J. Corella, On the Modeling of the Kinetics of the Selective Deactivation of Catalysts. Application to the Fluidized Catalytic Cracking Process, Ind Eng Chem Res, 43 (2004) 4080-4086.
[79] J. Gmeinbauer, C. Ramakrishnan, A. Reichhold, Prediction of FCC product distributions by means of feed parameters, Oil Gas-Eur Mag, 30 (2004) 29-33.
[80] J.R. Hernández-Barajas, R. Vázquez-Román, M.G. Félix-Flores, A comprehensive estimation of kinetic parameters in lumped catalytic cracking reaction models, Fuel, 88 (2009) 169-178.
[81] W.R. Gilbert, E. Morgado Jr, M.A.S. de Abreu, G. de la Puente, F. Passamonti, U. Sedran, A novel fluid catalytic cracking approach for producing low aromatic LCO, Fuel Process Technol, 92 (2011) 2235-2240.
[82] I.-S. Han, C.-B. Chung, Dynamic modeling and simulation of a fluidized catalytic cracking process. Part II: Property estimation and simulation, Chem Eng Sci, 56 (2001) 1973-1990.
[83] F.-L. Martínez-Cruz, G. Navas-Guzmán, J.-P. Osorio-Suárez, PREDICTION OF THE FCC FEEDSTOCKS CRACKABILITY, CT&F - Ciencia, Tecnología y Futuro, 3 (2009) 125-142.
[84] D.M. Nace, Catalytic Cracking over Crystalline Aluminosilicates. Microreactor Study of Gas Oil Cracking, Product R&D, 9 (1970) 203-209.
[85] L.J. McPherson, Causes of FCC reactor coke deposits identified, Journal Name: Oil Gas J.; (United States); Journal Volume: 82:37, (1984) Medium: X; Size: Pages: 139-143.

[86] D.M. Nace, Catalytic Cracking over Crystalline Aluminosilicates. I. Instantaneous Rate Measurements for Hexadecane Cracking, Product R&D, 8 (1969) 24-31.

[87] M.A. den Hollander, M. Makkee, J.A. Moulijn, Coke formation in fluid catalytic cracking studied with the microriser, Catal Today, 46 (1998) 27-35.

[88] V. Van Speybroeck, K. Hemelsoet, B. Minner, G.B. Marin, M. Waroquier, Modeling elementary reactions in coke formation from first principles, Molecular Simulation, 33 (2007) 879-887.

[89] G.M. Bollas, I.A. Vasalos, A.A. Lappas, D.K. Iatridis, S.S. Voutetakis, S.A. Papadopoulou, Integrated FCC riser—regenerator dynamics studied in a fluid catalytic cracking pilot plant, Chem Eng Sci, 62 (2007) 1887-1904.

[90] Y. Zhang, C. Lu, T. Li, A practical countercurrent fluid catalytic cracking regenerator model for in situ operation optimization, Aiche J, 58 (2012) 2770-2784.

[91] J.R. Arthur, Reactions between carbon and oxygen, Transactions of the Faraday Society, 47 (1951) 164-178.

[92] J.L. Fernandes, C.I.C. Pinheiro, N.M.C. Oliveira, A.I. Neto, F. Ramôa Ribeiro, Steady state multiplicity in an UOP FCC unit with high-efficiency regenerator, Chem Eng Sci, 62 (2007) 6308-6322.

[93] C.I.C. Pinheiro, J.L. Fernandes, L. Domingues, A.J.S. Chambel, I. Graça, N.M.C. Oliveira, H.S. Cerqueira, F.R. Ribeiro, Fluid Catalytic Cracking (FCC) Process Modeling, Simulation, and Control, Ind Eng Chem Res, 51 (2011) 1-29.

[94] O. Faltsi-Saravelou, I.A. Vasalos, G. Dimogiorgas, FBSim: A model for fluidized bed simulation—II. Simulation of an industrial fluidized catalytic cracking regenerator, Comput Chem Eng, 15 (1991) 647-656.

[95] D.Q. Mayne, J.B. Rawlings, C.V. Rao, P.O.M. Scokaert, Constrained model predictive control: Stability and optimality, Automatica, 36 (2000) 789-814.

[96] D. Angeli, R. Amrit, J.B. Rawlings, On Average Performance and Stability of Economic Model Predictive Control, Automatic Control, IEEE Transactions on, 57 (2012) 1615-1626.

[97] R. Amrit, J.B. Rawlings, L.T. Biegler, Optimizing process economics online using model predictive control, Comput Chem Eng, 58 (2013) 334-343.

[98] L. Würth, J.B. Rawlings, W. Marquardt, Economic dynamic real-time optimization and nonlinear model-predictive control on infinite horizons, in: Proceedings of the international symposium on advanced control of chemical process, Istanbul, Turkey, 2009.

[99] M. Diehl, R. Amrit, J.B. Rawlings, A Lyapunov function for economic optimizing model predictive control, Automatic Control, IEEE Transactions on, 56 (2011) 703-707.

[100] R. Amrit, J.B. Rawlings, D. Angeli, Economic optimization using model predictive control with a terminal cost, Annual Reviews in Control, 35 (2011) 178-186.

[101] M.A. Muller, D. Angeli, F. Allgower, On convergence of averagely constrained economic MPC and necessity of dissipativity for optimal steady-state operation, in: American Control Conference (ACC), 2013, 2013, pp. 3141-3146.

[102] M. Heidarinejad, J. Liu, P.D. Christofides, Economic model predictive control of nonlinear process systems using Lyapunov techniques, Aiche J, 58 (2012) 855-870.
[103] A. Helbig, O. Abel, W. Marquardt, Structural concepts for optimization based control of transient processes, in: Nonlinear Model Predictive Control, Springer, 2000, pp. 295-311.
[104] J. Kadam, M. Schlegel, W. Marquardt, R. Tousain, D. Van Hessem, J. van den Berg, O. Bosgra, A two-level strategy of integrated dynamic optimization and control of industrial processes—a case study, Computer Aided Chemical Engineering, 10 (2002) 511-516.
[105] M. Ellis, P.D. Christofides, Integrating dynamic economic optimization and model predictive control for optimal operation of nonlinear process systems, Control Eng Pract, 22 (2014) 242-251.
[106] L. Würth, R. Hannemann, W. Marquardt, A two-layer architecture for economically optimal process control and operation, Journal of Process Control, 21 (2011) 311-321.
[107] H. Sildir, Y. Arkun, U. Canan, S. Celebi, U. Karani, İ. Er, Dynamic Modeling and Optimization of an Industrial Fluid Catalytic Cracker, Ind Eng Chem Res, (submitted) (2014).

VITA

Hasan Şıldır graduated from Şehit Osman Altunkuyu Anatolian High school at 2005. He joined Chemical and Biological Engineering Department for PhD at Koç University after he obtained a BS degree of chemical engineering at Boğaziçi University in 2010. In his PhD thesis, he focused on the real time optimization of industrial cracking processes. He published and submitted a few studies in journals and presented some of his work in conferences. His current research areas include, process modeling, control of large scale systems, process monitoring, process synthesis and optimization, computer aided systems engineering and numerical methods.